MAGISTERARBEIT

Titel der Magisterarbeit

„Fluorine in AGB-stars“

Verfasser

Andreas Hren, Bakk.

angestrebter akademischer Grad

Magister der Naturwissenschaften (Mag. rer. nat.)

Wien, 2012

Studienkennzahl lt. Studienblatt:	**A 066 861**
Studienrichtung lt. Studienblatt:	**Astronomie**
Betreuerin / Betreuer:	**Doz. Mag. Dr. Thomas Lebzelter**

Eidesstattliche Erklärung

Ich erkläre hiermit des Eides Statt, dass ich die vorliegende Arbeit selbstständig und ohne Benutzung anderer als der angegebenen Hilfsmittel angefertigt habe. Die aus fremden Quellen direkt oder indirekt übernommenen Gedanken sind als solche kenntlich gemacht.

Diese Arbeit wurde bisher in gleicher oder ähnlicher Form keiner anderen Prüfungsbehörde vorgelegt und auch noch nicht veröffentlicht.

Contents

Chapter 1

Introduction

Some people, especially astronomers, like to call astronomy the oldest science of mankind. As such, one of the main questions was the nature of the objects on the sky, what they are composed of, why do they shine and if they are eternal. Another, maybe even more important question was the nature of things on earth, like the composition of 'things' and the differences between solid, liquid and gaseous substances. These two topics seemed for the longest time of human history more or less independent, since how the bodies in the stellar sphere could even possibly be composed of the same elements as the human body or the desk I am writing this text at[1]? However, during the previous century it became clear, that the processes going on in stars are absolutely fundamental for the existence of the world as we know it.

1.1 Stellar nucleosynthesis

Almost all elements we know today are produced in stars of different types and initial masses, the only exceptions being hydrogen, helium and traces of lithium formed in the big-bang nucleosynthesis, first described by Alpher, Bethe, & Gamow (1948). So, without the contribution of stars, chemistry would be a rather simple subject, however there would also be nobody to study it.

The main product of stellar evolution is helium, since the fusion of hydrogen to ^{4}He is the primary energy source of most stars. The majority of the heavier elements, in astronomy usually called 'metals', can be produced by helium burning through the triple-α process and various other fusion and particle-capture processes described below at the later stages of stellar evolution (Burbidge et al., 1957). While this accounts for most of the elements we observe, some of them ask due to their abundances or their very existence for a closer look, for example lithium and beryllium, which can be produced as by-products of hydrogen-burning through the Cameron-Fowler mechanism (Cameron & Fowler, 1971) as well as technetium, which is despite the instability of all its isotopes observed in the spectra of certain AGB-stars (Merrill, 1952) and therefore and indicator for the 3^{rd} dredge-up (Lebzelter & Hron, 2003). But instead of going into too much detail here, let's take a look to the contribution of different types of stars first, in order to get a good overview.

[1]Created with LaTeX.

If not stated otherwise, data and information for this chapter are taken from Burbidge et al. (1957), Pagel (1997) and Salaris & Cassissi (2005).

1.1.1 Hydrogen-burning

The fusion of four protons to ^{4}He is the primary energy source of all stars on the main sequence of the colour-magnitude-diagram (CMD), as well as for the stars on the red giant branch (RGB). Compared to the later fusion processes it is very energy-efficient, a single reaction chain has an energy yield of roughly 6.54 MeV per nucleon (Salaris & Cassissi, 2005). Together with the high initial abundance of hydrogen these are the reasons why stars spend the majority of their lifetime on the main sequence, burning hydrogen in their cores. Just once the depletion of hydrogen in the core becomes significant, the star is forced to adapt to it by hydrogen shell burning and moving on the RGB.

There are two processes which are important for hydrogen burning, the pp-chain and the CNO-cycle. The first one starts with the fusion of two protons to deuterium (^{2}H), which can successively capture another proton to build up ^{3}He. Two ^{3}He-cores then can react to ^{4}He, releasing two protons in the process. This first pp-branch is being supplemented by the ppII and ppIII branches, which lead via lithium and beryllium to the same result ^{4}He. Although these two branches typically contribute just a small percentage of the energy 'production' in a star, they are very important for the understanding of the previously mentioned Cameron-Fowler mechanism.

In stars which are already enriched with heavier elements, there is a second hydrogen-converting process to be taken into consideration. The elements carbon, nitrogen and oxygen can act as catalysts at the fusion of hydrogen, the process is therefore often called CNO- or also Bethe-Weizsäcker-cycle[2] (Bethe, 1939). The cycle starts at ^{12}C and leads through a series of proton capture and beta-decay processes via ^{13}N, ^{13}C, ^{14}N, ^{15}O and ^{15}N back to ^{12}C. At the last stage a proton is captured and a free ^{4}He is produced, witch leads to the same net yield as the pp-chain. However, not all of these reactions have the same probability. In this cycle the reaction ^{14}N(p,γ)^{15}O is the least probable one, therefore creating a bottleneck at nitrogen. Therefore, in regions where the CNO-cycle occurs, nitrogen is enriched at the cost of mostly carbon and, to a lesser extent, oxygen. The CNO(I)-cycle can also branch out, leading to the CNO-II, III and IV cycles, where slightly heavier nuclei (for example ^{16}O, ^{17}O and ^{18}F) are taking part and, thus, higher temperatures are required for it to take place. Additionally, there is also a small probability that instead of the last reaction of the CNO-IV cycle, ^{19}F(p,α)^{16}O, the process ^{19}F(p,γ)^{20}Ne occurs, which allows a minor loss of catalyst-nuclei (Burbidge et al., 1957).

The efficiency of these nuclear burning processes depends strongly on the temperature. While the temperature dependency for the pp-chain is approximately $\epsilon_{pp} \approx T^4$, the one for the CNO-cycle lies around $\epsilon_{CNO} \approx T^{18}$ (Salaris & Cassissi, 2005). The consequence of the different temperature sensitivities is, that for a given metallicity the pp-chain dominates the energy production at lower core temperatures ($T_c<15*10^6$K), while at

[2]Named after Hans Bethe and Carl von Weizsäcker, who proposed this process independently.

higher temperatures the CNO-cycle is the main source of energy. For the sun the contribution by the CNO-cycle is at roughly 10 percent of the total energy production.

1.1.2 Helium-burning

As a result of hydrogen shell-burning and core contraction during the red giant branch phase, most stars ($M_{cHe} > \approx 0.5 M_{\odot}$ (Salaris & Cassissi, 2005)) reach the necessary physical conditions for the onset of helium-burning through the triple-α process in their hydrogen-depleted cores. The fundamental reaction of the He-burning process is the production of ^{8}Be out of two ^{4}He-nuclei. However, ^{8}Be is unstable and decays in a short timescale back into Helium-cores, leaving virtually no time for a third α-particle to react with the beryllium to form ^{12}C. The probabilities for both reactions to occur would be usually very small. It is, however, facilitated by the fact, that the combined energy of a Be- and a He-core match almost exactly an excited state of the carbon nucleus. This resonance is fundamental for the production of carbon in stars and was predicted by Fred Hoyle before it was observed by William Fowler (Burbidge, Burbidge, Fowler, & Hoyle, 1957).
Since it is still necessary for three particles more massive than hydrogen to interact almost at the same time, the pressure and temperature in a main-sequence star are too low for the reactions to occur, because a minimum temperature of roughly $1.2 * 10^{8}$ K must be reached for the onset of helium-burning. Depending on the star's total mass, this onset can take place either violently during a helium-core-flash in low mass stars ($M_{*} < 2.25 M_{\odot}$) due to their degenerated cores after the main sequence, or quietly in intermediate and high mass stars, who reach the necessary temperatures before the core degenerates (Salaris & Cassissi, 2005).

While the requirements for helium-burning are significantly higher than the ones for hydrogen-burning, the amount of energy released per single reaction is more than a magnitude less. Per ^{12}C-core produced 7.27 MeV are released, which corresponds to ≈ 0.6 MeV per nucleon, compared to the value of ≈ 6.54 MeV per nucleon at the production of ^{4}He. That is the main reason, why helium burning is, compared to hydrogen burning, just a relatively short episode of the stellar evolution.
There are a number of other reactions which contribute during helium burning, using the produced ^{12}C as compound for further α-capture. The first of these processes, $^{12}C(\alpha,\gamma)^{16}O$, is particularly important, since it releases a similar amount of energy per reaction as the triple-α process while using just one α-particle. The cross-section of this reaction therefore has a significant impact on the core helium-burning lifetime. Further α-capture processes are possible, although the production of α-elements heavier than ^{20}Ne are very unlikely. Therefore, the result of core helium burning is a CO-core with traces of neon.

After helium is depleted in the core, helium burning continues in a shell and the (low and intermediate mass) stars enter their AGB-phase (Section 1.2). This marks the end of their evolution, the CO-core finally becomes a white dwarf, while strong stellar winds remove almost the whole envelope, releasing a considerable proportion of the produced elements, mainly carbon and nitrogen, into the interstellar medium (ISM).

1.1.3 Later burning stages

For high mass stars (M_*>$8M_\odot$ (Salaris & Cassissi, 2005)), the previously created CO-core reaches the necessary temperature and densities for the fusion of carbon to neon, sodium or magnesium, $^{12}C(^{12}C,\alpha)^{20}Ne$,$^{12}C(^{12}C,p)^{23}Na$ and $^{12}C(^{12}C,n)^{23}Mg$ respectively. Once the carbon in the core is exhausted and the carbon burning moves to a shell, the core can heat further. This leads to the burning of neon due to the fact that the alpha-separation energy of neon is significantly lower than the one of oxygen, the fundamental (and endothermic!) process here being $^{20}Ne(\gamma,\alpha)^{16}O$. Following the destruction of neon in the core the star enters the oxygen-burning stage. Two ^{16}O-nuclei produce an unstable ^{32}S-nucleus which can decay in four different ways, forming either ^{31}S, ^{31}P, ^{30}P or ^{28}Si. The produced silicon plays an important role in the following and last burning stage of massive stars, the fusion of silicon for iron-peak elements, mainly ^{56}Fe and ^{52}Cr. After the development of the iron core and the achieving of nuclear statistical equilibrium (all nuclear reactions are balanced by their inverse reaction) the star ends its life in a core collapse supernova, releasing a big proportion of its processed materials, mainly the α-elements O, Ne, Mg, Si and S as well as some iron into the ISM.

However, since iron-peak elements are formed at the very end of the process, the majority of these nuclei is trapped in the neutron star resulting from the supernova. So there must be an additional source of iron to explain the high solar abundance of this element. The common scenario are white dwarfs in close binary systems. Once the companion star evolves to a giant, the white dwarf can gain additional mass by accretion of material from its companion. Once it reaches the Chandrasekhar-limit ($M_* \approx 1.4M_\odot$ (Salaris & Cassissi, 2005)), a thermonuclear runaway is ignited which leads to the disruption of the white dwarf. The main products of such events are iron-peak elements, while the yield of elements like Si and S is similar to and the yield of oxygen is significantly lower than the one at "normal" SNe. This can be observed by measuring O/Fe and Fe/H-ratios in various stellar populations. At low metallicity they show a linear relation, since both elements are produced by massive stars in a more or less constant ratio. But at a certain point the O/Fe ratio starts to evolve differently with increasing metallicity, since additional iron comes into play. This observation can be explained by the longer evolution time of thermonuclear-runaway SNe.

1.1.4 Neutron-capture processes

The iron isotope ^{56}Fe has the lowest mass per nucleon of all known isotopes. Its production in a massive star marks the end of its lifetime, since all nuclear processes leading away from it are endothermic. So how can elements beyond the iron-peak be produced?

The most important processes are the rapid- and slow-neutron capture, where free neutrons are captured by iron-peak nuclei. If the resulting nucleus is unstable, a β-decay can follow, leading to an isotope of the next element in the periodic table. The ratio between the neutron-capture and the β-decay timescales determines, whether the nucleus follows the r- or the s-path. If the neutron-capture rate is high, the nucleus can capture a high number before a β-decay of the core will take place; if the rate is low, the unstable nucleus has enough time to decay and it closely follows the line of stable isotopes.

Since free neutrons are unstable, the presence of abundant neutron sources is crucial for both neutron capture processes. For the s-process, the reaction $^{13}C(\alpha,n)^{16}O$ is believed to be the main neutron source. It, however, requires a significant number of ^{13}C and ^{4}He-nuclei to be effective. These requirements can be met in the intershell-region of AGB-stars, where this reaction is a slow but steady neutron source; typical neutron densities are around $10^8/cm^{-3}$. In contrast to this, the r-process requires significantly higher neutron densities, which can be reached by the photodisintegration of iron and other abundant elements. This limits the process to supernovae.

An interesting feature is the low neutron-capture cross section for nuclei with closed neutron shells, which occur at some specific neutron-numbers (n=28, 50, 82, 126...). This leads to abundance-peaks in s-process elements, mostly at ^{88}Sr, ^{138}Ba and ^{208}Pb. Besides these peaks, the relative abundance of the isotopes produced through the s-process depends also on the initial metallicity; if the number of free neutrons available per seed-nucleus is higher due to low initial metallicity, heavier elements can be produced. Additionally, if the neutron capture timescale is close to the β-decay timescale of an unstable isotope, branching can occur. The line of stable nuclei ends at $^{208}Pb/^{209}Bi$, more massive nuclei can not be produced through the s-process.

R-processed material shows peaks due to closed neutron shells as well. The peaks however, are shifted to slightly lower masses (about 10 atomic mass units), because the required neutron numbers are reached at lower A (proton + neutron number) and the following β-decays follow a constant A line. The maxima lie therefore around ^{74}Ge, ^{132}Xe and ^{195}Pt and are less sharp then the equivalent s-process peaks. Branching is not a factor in the r-process and the initial metallicity plays just a minor role, since the region where the process takes place was already the site of various nuclear burning processes, heavily modifying the chemical composition.

1.2 AGB-Stars

As already mentioned in the previous section, the AGB-phase is one of the final evolutionary stages for low and intermediate mass stars ($\approx$ 0.8-8$M_\odot$). The main components are: a Carbon-Oxygen-Core, a thin helium and a hydrogen burning shell, a hydrogen-depleted intershell region, and an extremely extended, convective envelope. But to see how the star evolves to this stage, let us take a step back first.

1.2.1 From the horizontal branch to the early AGB

Stars on the horizontal branch (or red clump, depending on the metallicity), are characterized by core Helium burning and a thin hydrogen burning shell around that core. Once the helium in the core is depleted, He-burning moves to a shell, analogous to the H-burning shell during the evolution away from the main sequence. Similarly, the star now moves to cooler effective temperatures and higher luminosities in the color-magnitude diagram again, entering a 2^{nd} giant phase. This time, however, it has two main energy sources; an AGB star with a structure very similar to the one outlined

above is formed. The coexistence of two burning shells causes a major problem, though. As mentioned earlier (sect. 1.1.2) the energy/mass-ratio of H- and He-burning differs by about a magnitude (≈6.5 compared to ≈0.6 MeV per nucleon). Therefore, in order to release the same amount of energy, the He-burning shell needs to burn through a significantly bigger mass layer; it consumes its 'fuel' faster. So, while the He-burning shell moves outwards rather rapidly inside the He-core, the H-burning shell does not increase the mass of this core fast enough to keep up. This problem is further intensified by the fact, that, due to the energy released by the He-burning shell, the overlying H-shell expands and cools, which further reduces the efficiency of H-burning. This can also lead to a temporary extinguishing of this shell at stars with higher mass (M_*>3-5$M_\odot$ (Salaris & Cassissi, 2005)), allowing the outer convective zone to reach into the intershell region and leading to a second dredge-up. The dredged up material consists mostly of H-burning ashes, primarily ^{4}He and ^{14}N. For stars of lower mass, the H-burning shell remains efficient and prevents such a mixing.
This phase in the stellar evolution lasts as long as the He-burning shell can be fed by of the He generated by previous hydrogen burning. Once it approaches the He/H discontinuity, however, He-burning switches off and H-burning takes its place as the main energy source again. With this temporary stop of He-burning, the early AGB-phase comes to its end.

1.2.2 The thermally pulsing AGB phase

At this stage, H-burning is the main energy source for most of the time. When enough helium accumulates on top of the CO-core ($10^{-3}M_\odot$ at a core mass of 0.8$M_\odot$ (Salaris & Cassissi, 2005)), however, it ignites again, resulting in a helium shell flash (or thermal pulse). During the thermonuclear runaway, the helium-burning shell is expanding again and lifting the layers above it, temporarily also extinguishing the H-burning shell. Due to the huge energy release, a convective zone on top of the He-burning shell is formed, mixing He-burning ashes (mostly ^{12}C) in the intershell region. Once an equilibrium between energy produced and released is established, the star continues to steadily burn He until the reservoir of helium produced before the flash is used up again. Once this happens, He-burning dies down again and the H-burning shell is reignited, leading to another long episode of stable H-burning and possibly generating enough 'fuel' for another thermal pulse. This cycle can repeat many times and is only limited by two factors: the mass of the stellar envelope, which at one point is not sufficient to build up enough helium for another pulse, and the mass of the degenerated CO-core, which could theoretically become massive enough to ignite carbon and, thus, end the AGB-phase. In order for this to happen during the thermally pulsing phase, however, a high number of pulses would have to take place and observations suggest that in fact the limited envelope mass is the deciding factor, due to mass loss (Salaris & Cassissi, 2005).
Mass loss plays a major role in late AGB evolution. There is a number of direct and indirect observations that suggest that AGB-stars must loose the bulk of their mass during this phase. Taking the supernova rate as an example, if all stars with initial masses higher than the Chandrasekhar-limit would end in a supernova, the often stated '≈ 1 supernova per 100 years in our galaxy' would be way to small to account for the high number of stars starting their evolution above this mass limit. The initial mass for a star evolving towards a supernova is significantly higher (M_*>8$M_\odot$ (Salaris &

Cassissi, 2005)) as stated earlier in section 1.1.3, so all stars between these two mass boundaries must loose the bulk of their mass in some way.
How this mass loss is taking place exactly on such a scale is still open to discussion, though, since not all mechanisms of driving this 'super wind' (10^{-8}-10^{-4}M$_\odot$/year (Salaris & Cassissi, 2005)) are fully understood yet. Pulsation for example, could play the main role here, since it enhances the formation of molecules and dust in the cool envelopes due to pressure and density changes, and this, in turn, helps at driving a strong stellar wind. Therefore, a strong correlation between pulsation and mass loss rate can be expected. Dust formation is commonly believed to be an important factor for mass loss, dust driven, radiation pressure based models work well with carbon rich dust (Habing & Olofsson, 2004). In the oxygen rich case on the other hand, radiation pressure on (primarily) silicate grains alone might be not sufficient to account for the observed mass loss rates and different scenarios might be necessary, for example a combination of carbon and silicate dust as discussed by Höfner & Andersen (2007) or a bigger influence of scattering by large silicate dust grains (Höfner, 2011).
Once the star lost most of its mass to the ISM and just an envelope of a few 10^{-3}M$_\odot$ (Salaris & Cassissi, 2005) remains, the hydrogen burning shell can not burn further, helium stops being stocked up and further thermal pulses can not take place. The star starts moving towards the left side of the color-magnitude diagram and becomes a white dwarf. Eventually, its surface becomes hot enough to ionize the envelope layers it released during the mass loss periods of the TP-AGB phase and they become visible at a planetary nebula.

1.2.3 The third dredge-up

For most stars, oxygen is the most abundant element on the stellar surface after hydrogen and helium. The surface composition usually remains unaltered through most of the stellar evolution, if external 'polluters' like binary companions for example are excluded. Dredge-up episodes, however, change that. The first and second dredge-ups enrich the stellar surface primarily with ashes of hydrogen burning, mostly ^{4}He, ^{14}N and ^{13}C.
For thermally pulsing AGB stars, however, dredge ups become more interesting from the chemical point of view. While the H-burning shell is switched off during the thermal pulse, the outer convective zone can penetrate into the intershell region, leading to the third dredge-up, or actually dredge-ups, since they do follow most thermal pulses and, therefore, repeat multiple times. The material dredged up this time differs significantly from the one involved in the first two dredge up episodes, since it can also contain the ashes of He-burning (^{12}C) and s-process elements (^{88}Sr, ^{138}Ba, ^{208}Pb and ^{99}Tc for example). Subsequent third dredge-up episodes lead to an enrichment of these elements in the outer layers of the star, where they can be detected. From the observational point of view especially carbon has an important role here, since its abundance has a major impact on the chemistry visible on the stellar surface. The reason for this is primarily the CO-molecule, which is formed predominantly at the 'typical' effective surface temperatures or red giants and binds most of the carbon and oxygen available. What is left over, whether carbon or oxygen, is free to form other molecules, for example H_2O and TiO the oxygen rich case (C/O < 1) and C_2 in the carbon rich case (C/O > 1) (Habing & Olofsson, 2004). This determines the shape of the visual and infrared

spectra to a great extent and therefore the photospheric C/O ratio is one of the stellar parameters which is relatively easy to observe and still provides valuable insight in the processes deep inside the star.
The efficiency of the third dredge-up depends on a number of factors, for example the CO-core mass, the mass of the stellar envelope and the mean metallicity, which affect both how deep the dredge up reaches into the intershell and the total amount of material dredged up each time. The properties of the stellar envelope are the deciding factor here once again, since evolutionary computations show that the third dredge-up does not take place once the envelope mass drops below $\approx 0.4M_{\odot}$ (Salaris & Cassissi, 2005). This also excludes stars below a certain mass limit (1.2-1.5$M_{\odot}$ (Salaris & Cassissi, 2005)) from experiencing the third dredge-up in the first place, since their envelope mass at the start of the TP-AGB phase is below that limit already. Therefore, AGB-stars in old populations, globular clusters in our galaxy for example, are not expected to show signs of the third dredge-up and in order to study its effects, we are forced to look for targets in younger stellar populations. In the case of this work, the stars in the two LMC clusters NGC 1846 (section 2.2) and NGC 1978 (section 2.1) were selected as promising targets.

1.3 What is fluorine?

Fluorine is the 9th element of the periodic system. The core of its primary isotope ^{19}F consists out of 9 protons and 10 neutrons, which represents also the only stable configuration for this element. All other isotopes are unstable and rather short living, ^{18}F having the by far longest half life time of them: $\approx$ 109 min. The core is complemented by a shell of 2 electrons in the 1s, 2s and 2d orbitals, leaving it one electron short of 'noble gas configuration' and marking it as the first halogen in the periodic system. As a consequence, atomic fluorine is the most electronegative element in existence, due to its electron configuration of seven valence electrons and its relative small size compared to other halogens. Therefore atomic and molecular fluorine are both very reactive and react with all elements except the noble gases helium and neon. Mixed with hydrogen it reacts even at very low temperatures explosively to hydrogen fluoride acid (HF). This is a fortunate feature for astronomic observations, however, since most if not all fluorine in the hydrogen-rich atmosphere of a cool star can be expected to be found in the HF-molecule as a consequence. A very good overview of this topic was published by Croswell (2003).

1.3.1 The fluorine abundance issue

If we take a look at the solar elemental abundances it becomes apparent, that fluorine is a special case among the lighter elements. Compared to its neighbouring elements oxygen and neon, its only stable isotope ^{19}F is roughly 3 magnitudes less abundant than ^{20}Ne, 4 times less abundant than ^{16}O and even the two oxygen isotopes ^{17}O and ^{18}O show significantly higher abundances. The only deeper hole in the abundance profile before that we find at the elements lithium, beryllium and boron, which are bypassed by the triple-α process. How can this low abundance be explained?

First, the element can not be produced via the caption of additional α particles on ^{12}C, since it is bypassed by the ^{16}O(α,γ)^{20}Ne reaction, which leads together with further burning stages (Section 1.1.3) to an increased production of elements in this area of the abundance profile. Furthermore, there is no known bottleneck in any of the other supplementary burning processes, like for example CNO-I producing ^{13}C and ^{14}N as a side effect (Section 1.1.1), which could lead to an increase of the fluorine abundance, most of them on the contrary rather reducing it.
Under the 'typical conditions' for nuclear reactions, where fluorine is formed among other elements, it can also be rapidly destroyed by reactions with both hydrogen (^{19}F(p,α)^{18}O) and helium (^{19}F(α,p)^{22}Ne), making its survival in a hydrogen and/or helium rich environment rather unlikely and its production in a star to a bit of a riddle. Therefore, in order to produce fluorine in any measurable amount, the freshly produced element must be somehow transported out of the zone where nuclear reactions take place before it can be destroyed, since otherwise the presence of fluorine would be just a temporary one.

1.3.2 Fluorine production sites

During the last decades, three different sites with the exceptional properties needed for fluorine production were suggested. The historically first attempt was made by Woosley & Haxton (1988) in the wake of the Supernova 1987A. In the scenario they suggest, the high energy neutrinos generated at the collapse of the core play an important role in the stars chemistry. In contradiction to the usual case, where neutrinos pass through most matter without interaction, here both the matter density and the energy of released neutrinos is high enough for a significant number of collisions to take place. Some of the neutrinos passing through the stars ^{20}Ne-layer (resulting from previous C-burning) do interact with the neon-cores and knock off a proton (^{20}Ne(ν,p)^{19}F) or a neutron (^{20}Ne(ν,n)^{19}Ne) and, thus, directly or indirectly form fluorine (^{19}Ne is unstable and decays to ^{19}F). Further nuclear reactions are prevented by the expanding shell and the element is released to the ISM. However, due to the scarcity of supernovae in our 'vicinity' nobody was ever able to detect fluorine in a supernova or a supernova remnant.

In a different scenario, suggested by Meynet & Arnould (2000), the authors expect to find the origin of fluorine in even more mass-rich objects, so called Wolf-Rayet stars. During their final evolutionary stages these extremely massive stars ($M_\star > 40\ M_\odot$) generate strong stellar winds and by this loose their hydrogen envelopes. Fusion reactions, which under normal conditions take place close to the stellar core and, thus, have no direct impact on the observed nuclear abundances, now take place close to the stellar surface. Newly produced elements, among them also fluorine (some of the stars nitrogen is transformed via ^{15}N(α,γ)^{19}F), can be carried out by the strong stellar winds and is, by this, saved from destruction. While this might be an important fluorine-source, also here there is no direct observational evidence yet. There are, however, observations of planetary nebulae by Zhang & Liu (2005), which indicate fluorine production in WR-stars.

There is one fluorine production scenario, however, where observational evidence is available. In the paper by Jorissen, Smith, & Lambert (1992), the discovery and mea-

surement of HF-features in the spectra of red giants was published. As the number of observations grew, one thing became obvious. Stars with high carbon to oxygen (C/O) ratios showed also higher fluorine abundances, suggesting that this element is somehow being produced in these stars and that this must in some way be connected with the carbon enrichment on the stellar surface. A theory to explain the observations was presented by Forestini et al. (1992) and further refined by Mowlavi et al. (1996), leading to following, rather complex scenario:
During the AGB-phase of an evolved star, fluorine can be produced in the He-rich intershell region via ^{15}N(α,γ)^{19}F, the same process as suggested for Wolf-Rayet stars. While a significant portion of ^{15}N results from the ashes of H-burning (CNO), this alone is not sufficient to explain the observed values. For the production of additional ^{15}N via the process ^{18}O(p,α)^{15}N, both the heavy oxygen isotope ^{18}O and a proton source are required. ^{18}O can be produced in the intershell region via the chain ^{14}N(α,γ)^{18}F(β^+)^{18}O and is not the limiting factor, since both ^{14}N and ^{4}He are to be found abundantly in the H-burning ashes. The proton source is a problem, however, since the intershell region is H-depleted and the two possible proton source reactions, ^{14}N(n,p)^{14}C and ^{26}Al(n,p)^{26}Mg, both require a neutron source in turn. Free neutrons are unstable and must be produced in the intershell region via the reaction ^{13}C(α,n)^{16}O, which is also the main neutron source for the s-process element enrichment. ^{13}C, however, is not too abundant in the intershell and a mixing-down of protons during the thermal pulse, when the outer convective zone can penetrate into the intershell region, is necessary to form a ^{13}C-rich pocket. This convective zone is also required to move the synthesized fluorine out of the area, before it can be destroyed.
The fluorine, after being produced by this rather complex production chain ^{14}N(α,γ)^{18}F (β^+)^{18}O(p,α)^{15}N(α,γ)^{19}F is transported to the stellar surface during the 3^{rd} dredge up, together with other elements typical for late AGB-evolution, primarily ^{12}C and s-process elements. Therefore, one would expect a strong correlation between the star's C/O ratio and its observed fluorine abundance during its late evolution.

1.3.3 Observations of fluorine

Fluorine can be observed in a number of different wavelength ranges. Fluorine was first found in the form of vibrational HF-lines in the K-band, published by Spinrad et al. (1971). The first abundance measurements by using this feature were performed by Jorissen, Smith, & Lambert (1992) and various observers used the same features when observing AGB stars. These observations are complemented by observations of post-AGB stars in the UV (Werner et al., 2005), detecting highly ionized fluorine in the white dwarf to be, and by the detection of neutral fluorine in the spectra of cool extreme helium stars (Pandey, 2006). Furthermore, both fluorine and hydrogen fluoride have been observed in the interstellar medium already by Snow & York (1981) and Neufeld et al. (1997). There are observations of fluorine in planetary nebulae, for example by Zhang & Liu (2005).
While this restricts direct observational evidence to AGB-stars, similar objects and the interstellar medium, there are also suggestions that WR-stars and supernovae must be responsible for some part of the fluorine in the universe (Renda et al., 2004). In the case of fluorine synthesis in AGB-stars, one would expect a slow, gradual enrichment of this element in the galaxy. Therefore, for example halo stars or old globular clus-

ter members should not show fluorine features, if the production would take place in AGB-stars only. In the case that supernovae are responsible for most of the fluorine in the universe, one would observe more or less the opposite. Old stars should show some 'initial' fluorine in their spectra due to the short evolution time of high mass stars, which end their life as supernovae and release their elements to the ISM for other stars to form out of eventually. The third possible fluorine source, WR-stars also have short evolution times but their mere existence requires a certain metallicity level first (Pagel, 1997). Therefore, if WR-stars are the main production source, one would expect a delayed fluorine enrichment in the galaxy. Renda et al. (2004) used the various enrichment patterns to study the impacts of the different sources on the galactic chemical evolution. They state that all three production sites are necessary to match observations. This illustrates nicely how indirect observations can support a theory, although no direct observations of fluorine synthesis in supernovae are available yet.

1.4 Observations in the Infrared

Observations in the near infrared (IR) (1-5μm) have a number of advantages when studying AGB-stars. First, their low effective temperatures mean that a significant part of their spectral energy distribution lies in the IR. A star with an effective temperature of 3000K, for example, has it's maximum at $\approx 1\mu$m. Second, the majority of molecular features, which are used to estimate stellar elemental abundances, are located here due to their rotational and vibrational transitions. Third, some AGBs are producing so much dust, that it significantly reduces their luminosity in the optical; the energy absorbed by the dust is then re-emitted in the mid IR. In the near IR however, dust becomes much more transparent, which means that observations in this range can pierce through thick dust-shells and detect such enshrouded objects. Also the center of our galaxy, which is hidden in the visual range by to the dust in the galactic plane, becomes visible at longer wavelengths.

However, besides their advantages for our topic, IR-observations face a number of problems, which are much less of an issue in the visual range. First, the high abundance of molecular features in the earth's atmosphere (mostly of H_2O, C_2O and O_3) limits the possible ground-based observations to a few atmospheric windows (bands), where at least a part of the radiation can penetrate till the ground. For the near IR these are the J- (1.1-1.4μm), H- (1.5-1.8μm), K- (2.0-2.4μm), L- (3.0-4.0μm) and M-bands (4.6-5.0μm). Outside of these bands, the transmission is next to zero and therefore, ground-based observations are impossible. To access these regions it is necessary to utilize air- or spaceborne observatories, like the Kuiper Airborne Observatory, SOFIA, ISO, Spitzer and Herschel. First ones can, by flying above most of the water vapor in the atmosphere and, thus, bypassing the H_2O-influence in the atmosphere, access the majority of the IR-range, while the last ones have no atmospheric restraints at all.

Second, the thermal radiation of the earth's atmosphere becomes a problem too, once one moves to longer wavelengths. While it's peak lies at $\approx 10\mu$m in the mid-infrared, the resulting background in the IR is by orders of magnitudes higher than in the visual and it shows variations on short timescales. Therefore, a sophisticated method to remove the thermal background is necessary: 'chopping' and 'nodding'. At the 'chopping', the telescopes secondary mirror is moved frequently at a frequency of a few Hertz, to observe an adjacent position on the sky. The pairs of pictures are than subtracted to remove the sky's background. However, since also the telescope itself radiates in the IR and the lightpath is not the same at both mirror positions, this leaves a radiative offset which must be accounted for by using the 'nodding'-technique, where the same idea is used. Yet here, the whole telescope is being moved in the same pattern (but at a lower frequency of course), which results in one positive image in the center, corresponding to 1/2 of the exposure time, and two shifted negative images, corresponding to 1/4 of the exposure time each. By this, most of the background's and telescope's glow can be corrected. While this procedure is mandatory at imaging and low-resolution spectroscopy, at high-resolution spectroscopy the small field of view and high dispersion of the light reduce the background per pixel. Thus, here a stare/nod mode can be used, like it is also the case in here used observations (Geballe et al., 2006).

As stated above, the telescope itself glows significantly in the IR. The only way to reduce this is cooling of the optical parts. While it is of course not possible to do this with the whole ground-based telescope, which would induce a number of other problems (thermal deformation, condensation, ice,...), modern IR-instruments are usually cooled with a combination of liquid nitrogen and/or helium, to reduce the temperatures within close to absolute zero. In contrast, spaceborne observatories like ISO, Spitzer and Herschel can and do use a combination of active and passive cooling to achieve low temperatures on the whole optical path, however they pay for this with higher costs, higher risk, a limited lifetime and lower angular resolution due to smaller mirrors.

1.5 The Gemini Observatory and Phoenix

The Gemini Observatory is maintained by a partnership of seven countries (United States, United Kingdom, Canada, Chile, Australia, Brazil, Argentina) and consists of two 8.1 meter telescopes. While one of them was built on the Mauna Kea on the main island of Hawaii (Gemini North), the other one is located on the Cerro Pachon in Chile (Gemini South), which allows the twin telescopes to cover the whole sky. They are equipped with a number of imaging and spectroscopic instruments for both the visual and the observable infrared ranges and a number of different instruments is mounted on the telescope's Cassegrain focus to provide flexibility in cases of weather changes, multi-instrument programs and 'observing emergencies' like SNe and Gamma Ray bursts.
The telescopes use a combination of active primary mirrors, rapid tip-tilt correction by the secondary mirror and an adaptive optics system to provide the best possible image quality. In contrast to other telescopes of their size, all mirrors of the Gemini Observatory are coated with (protected) silver instead of aluminium, which is more commonly used. This gives them a higher reflectivity in wavelengths over $\lambda \geq$400nm, a reduced thermal infrared emission by factors of 2-3 and makes them, in consequence, one of the best tools for IR-observations.

The Phoenix spectrograph (Hinkle et al., 2003) offers a high spectral resolution (R $\approx$ 50000 - 80000) in the near IR wavelength-range of 1-5μm. To achieve this, it is built as an echelle spectrometer, but it uses order-sorting filters instead of the commonly used cross-disperser to divide the different overlapping echelle-orders. It was originally built for the National Optical Astronomy Observatory (NOAO) and was first used at the Kitt Peak National Observatory. Later it was moved (as a loan by NOAO) to the Gemini South telescope as one of its first instruments. Further, it was upgraded with a 512 x 1024 InSb Aladdin II array, which improved its performance greatly. While it proved to be a scientifically productive instrument, it is no longer available for science use, since it was removed from the Gemini South telescope in January 2011 in favour of the new adaptive optics system (GeMS). This leaves the telescope without a high-resolution spectrometer in this wavelength range.

All information presented in this section was gathered on the Gemini Observatory homepage (Gemini Observatory, 2012).

Chapter 2

Target clusters

For this work, K- and H-band spectra of oxygen-rich AGB-stars in NGC 1846 and NGC 1978 were used. Both clusters are members of the Large Magellanic Cloud (LMC), one of the Milky Ways' satellite galaxies. There is a number of reasons, why it its necessary bother to observe objects that far away, while there would be a high number of closer AGB-star-targets to observe. First, observing stars in a cluster allows to estimate their absolute magnitudes (via the red clump brightness for example), which is always a problem for field stars, when they are too far away for parallax-measurements and do not happen to be periodic variables with a well known period-luminosity relation (like Cepheids, RR Lyrae-stars, etc.) or other standard candles. Additionally, the age of a cluster can be estimated by isochrone-fitting in the color-magnitude diagram (CMD), which also allows to estimate the masses of stars at different positions in the diagram, which is very hard to do for field-stars and possible just for binaries.
However, choosing clusters in the LMC over the ones of the Milky Way has an additional reason. Clusters in the Milky Way tend to be too old, their intermediate-mass stars evolved already through their AGB-phases and the AGB-stars present have a too low mass to have an efficient 3rd dredge-up, which I aim to observe. Therefore, the nearest possible candidates for observation are clusters in the Magellanic Clouds. They tend to be younger and, like their parent galaxy, less metal rich.

2.1 NGC 1978

The LMC hosts three different globular cluster populations, an old one, with ages similar to the milky ways clusters, as well as an intermediate and a young one, with ages around 1-3 and <1Gyrs, respectively (Olszewski et al., 1996). NGC 1978 is one of the LMC's intermediate age clusters. Its elemental abundances have been studied by various groups already, in particular by Ferraro et al. (2006) and Mucciarelli et al. (2007) who are both deriving a metallicity of about [Fe/H] = -0.37. The latter paper is also reporting a slight depletion of alpha-elements. This is in disagreement with previous results by Hill et al. (2000), who derive a significantly lower metallicity of [Fe/H] = -0.96 and an O/Fe-ratio of +0.37, so no alpha-element depletion. Results by Alcaíno et al. (1999) indicate the presence of two sub-populations in the cluster with an offset of 0.2 dex in metallicity. Although this result, together with the cluster's elongated shape, might point to a merger-event, which would explain both observations, this seems un-

likely. Fischer et al. (1992) excluded such a scenario through dynamical studies and the publication by van den Bergh (2008) suggests, that tidal interaction might be the more likely explanation for the clusters shape.
By fitting model isochrones to the cluster's CMD, Mucciarelli et al. (2007) derive a cluster's age and turn-off mass of τ = 1.9 Gyr and M_{TO} = 1.49 $M_\odot$. However, due to the uncertainty of this method (the values depend on the chosen models), also higher cluster-ages (of up to τ = 3.2 Gyr) and lower turn of masses (M_{TO} = 1.44 $M_\odot$) could be possible (Mucciarelli et al., 2007). This places the stars of this cluster close to the theoretical lower mass limit of the third dredge-up (sect. 1.2.3).
The work of Lloyd Evans (1980) lists a number of cluster-members as red giants and his naming-convention (LE) will be primarily used in this thesis (the same is true for the targets in NGC 1846). Furthermore, Frogel et al. (1990) report a number of carbon stars in their sample, identified via photometric studies, pointing towards an ongoing third dredge-up in at least some of the cluster members. One alternative to this could be an 'extrinsic' scenario, where the stars would be contaminated by a more massive and further evolved binary companion.

The paper by Lederer et al. (2009) tries to explain some of the contradictory observational features of NGC 1978. First: the cluster has C-stars, second: the clusters M-stars show no conclusive signs of third dredge-up and third: there is no saturation in the carbon isotopic ratio. Additionally, there are no S-stars (C/O $\approx$ 1) to be observed in the cluster, which would be expected at the transition from an O-rich to a C-rich chemistry. This, as well as the contradiction between the first and second statements above, might be explained by the low number of stars observed and the short lifetime of a thermally pulsing AGB-star. However, after discussing a number of scenarios, they were not able to find a theoretical scheme to satisfyingly reproduce the chemical abundance pattern of the cluster. The existence of a non-standard mixing mechanism might offer some solutions though. I refer to the above mentioned paper for more details concerning their results.

2.2 NGC 1846

Like NGC 1978, this cluster belongs to the LMC's intermediate age cluster population. While it seems to be younger than NGC 1978 (τ = 1.4 Gyr and M_{AGB} = 1.8 $M_\odot$) (Lebzelter & Wood, 2007) it shows a slightly lower metallicity of Fe/H = -0.49 (Grocholski et al., 2006). This places it at the metal-deficient end of the LMC's cluster population and is somewhat counter-intuitive, since one would expect younger clusters to be more metal-rich. Other authors however, published even lower values for the metallicity, reaching down to [Fe/H] = -1.5, deduced by Leonardi & Rose (2003). The age estimation via isochrones is uncertain as well, providing values from τ = 1.9 to τ = 2.2 Gyrs ($\pm$0.4 Gyrs) (Mackey & Broby Nielsen, 2007), corresponding to AGB-masses of M_{AGB} = 1.8 - 1.3 $M_\odot$. The exact deduced values depend mostly on which theoretical isochrones are chosen. The authors also suggest the existence of two stellar populations within the cluster with similar metallicity but an age-difference of about 0.3 Gyrs, which would help to explain the two sets of isochrones they need for fitting the CMD best. The age and AGB-mass estimations by using pulsation periods done by Lebzelter & Wood (2007) indicate, that the observed objects are at the higher end of the mass spectrum (1.8 $M_\odot$) and, thus, part of the younger population in the cluster. The authors state, however, that the assumed age-separation is too small to be detectable by the AGB-star pulsation behaviour.

The observation of carbon enrichment during the third dredge-up was part of the paper by Lebzelter et al. (2008). A number of M-, C- and S-type giants has been observed in the H- and K-band and compared to theoretical atmosphere models to derive their C/O- and $^{12}C/^{13}C$-ratios. For the oxygen-rich stars an enhancement for both quantities could be observed, indicating ongoing third dredge-up in some cluster members. The observed C-stars proved to be harder to model, leading to rather uncertain values for both quantities, although the correlation between them is visible as expected and good agreement with model predictions for both values can be met when assuming an initial cluster-overabundance of oxygen. Additionally, standard dredge-up models fail to explain the $^{12}C/^{13}C$-ratio found in the clusters C-stars. This might indicate the need of some extra-mixing. Furthermore, the two observed S-stars show C/O-ratios of significantly less than 1; their S-type characteristics at this C/O might be a result of their relatively high temperatures.
Finally, they also derived the fluorine abundance for the oxygen-rich stars. It shows a correlation with the C/O-ratio, which (qualitatively) confirms the nucleosynthesis of this element in AGB-stars. Their numbers however, are based on a single HF-line in the K-band, blended with a ^{13}CO-line, and might, therefore, be subject to systematic error, as pointed out by the authors. See also: Karakas et al. (2010)

Chapter 3

Observations

For this work, K- and H-band spectra of oxygen-rich AGB-stars in the two LMC clusters NGC 1846 and NGC 1978 were used to compare the fluorine abundances in AGB stars with their C/O ratios. The targets were observed with the Phoenix spectrograph at the Gemini South Telescope (Section 1.5). While the data of the cluster NGC 1978 were already used by Lederer et al. (2009) and were available already fully reduced, the ones from NGC 1846 just underwent the basic bias-, dark- and flatfield-reduction and, thus, needed some additional refining. The extraction of spectra from the data and their calibration will be the main topic of this chapter; for all of these reduction-steps tasks of the IRAF-package were used (Tody, 1986).

3.1 Observational data

The observations of the targets in NGC 1978 were carried out mostly in Dec.2006, in consequence of an observing proposal by Lebzelter et al. to study the dredge up pattern in this cluster by observing carbon lines in the H- and K-bands. The results were published in Lederer et al. (2009) and some of them were summarized in the previous section on NGC 1978. Details concerning the observations can be found in Table 3.1; for detailed information on the data-reduction, please refer to the above mentioned paper. The obtained and already reduced K-band data cover a wavelength range from 2.3580 to 2.3680μm with a spectral resolution of R = 50000 and show a single HF-feature (R7) at 2.36365μm. Since the observations were made primarily to derive the C/O- and $^{12}C/^{13}C$-ratios of the targets, however, this feature is not optimal for deducing the fluorine abundance, because it is blended with a strong ^{13}CO-line. Nevertheless, this line was also used by Lebzelter et al. (2008) to derive F-abundances for some targets in NGC 1846 successfully, although with some uncertainty.

Following the latter paper and the limitations in deriving the fluorine-abundances, Lebzelter et al. asked for more observing time in a slightly different wavelength range, especially chosen to measure the fluorine-abundance of the evolved cluster-members. The observed spectra of that second run reach from λ_1 = 2.2756 μm to λ_2 = 2.2857 μm, corresponding to approximately λ_{01} = 2.2738 μm and λ_{02} = 2.2838 μm once the redshift due to the cluster's heliocentric radial velocity of roughly v_R = 235.2 km/s (Grocholski et al., 2006) is taken into account. Additionally, they asked for H-band

Table 3.1: List of targets and log of observations for NGC 1978, all targets are M-stars, spectra were taken in the H- and in the K-band (LE stands for Lloyd Evans 1980). J- and K-magnitudes are 2MASS values (Skrutskie et al., 2006). Data from: Lederer et al. (2009)

ID	M_J	M_K	H band (λ_c = 1.5585 μm)	$(S/N)_H$	K band (λ_c = 2.367 μm)	$(S/N)_K$
A	12.253	11.116	2006 Dec. 03: 3 x 1000s	55	2006 Dec. 05: 3 x 1000s	65
LE4	12.347	11.199	2006 Dec. 03: 3 x 1000s	65	2006 Dec. 05: 3 x 1000s	65
LE5	12.527	11.387	2006 Dec. 03: 3 x 1200s	50	2006 Dec. 05: 3 x 1200s	55
LE9	13.315	12.259	2008 Mar. 19: 4 x 1800s	45	2006 Dec. 06: 3 x 2000s	50
LE10	12.917	11.802	2006 Dec. 03: 3 x 1800s	60	2006 Dec. 05: 3 x 1800s	70

Table 3.2: List of targets and log of observations for NGC 1846, all targets except LE13 are M-stars, spectra were taken in the H- and in the K-band (LE stands for Lloyd Evans 1980). J- and K-magnitudes are 2MASS values (Skrutskie et al., 2006).

ID	M_J	M_K	H band (λ_c = 1.557 μm)	$(S/N)_H$	K band (λ_c = 2.281 μm)	$(S/N)_K$
H39	12.841	11.748	-	-	2008 Nov. 11/12: 4 x 1800s	30
LE8	12.438	11.230	-	-	2008 Nov. 11: 4 x 900s	35
LE9	12.671	11.528	-	-	2008 Nov. 11: 4 x 1200s	35
LE16	12.533	11.429	-	-	2008 Nov. 11: 4 x 1200s	50
LE7	12.558	11.352	2008 Nov. 13: 4 x 1200s	35	2008 Nov. 12: 4 x 1200s	40
LE13	12.256	10.963	2008 Nov. 13: 2 x 1000s	25	2008 Nov. 11: 4 x 900s	50
LE14	12.662	11.543	2008 Nov. 13: 4 x 1200s	40	2008 Nov. 12: 4 x 1200s	40
LE15	12.666	11.481	2008 Nov. 13: 4 x 1200s	35	2008 Nov. 12: 4 x 1200s	45
LW1	12.577	11.462	2008 Nov. 13: 4 x 1200s	25	2008 Nov. 12: 4 x 1200s	35

observations of some cluster members, which were not part of their previous sample (λ_H = 1.5532 - 1.5606 μm). Their purpose was to derive the C/O ratios for these stars, since this value is critical for the calculation of synthetic spectra. All spectra were taken with a spectral resolution or R = 50000, for more details concerning the observations please refer to Table 3.2.
In contrast to the single line in the NGC 1978 observations, this second range includes three different HF-lines, namely R15, R16 and R23. The first two lines are strong and free of blends. The third line R23 however, turned out to be very weak and rather unaffected by F-abundance variations. Therefore it was neglected in the analysis. Some minor problems were also caused by the line R15 because of its location at the very edge of the observed spectra, where the normalization turned out to be somewhat problematic for most stars. It, however, usually provides the same numbers as the line R16, which seems to be free of blends and other problems.

3.2 Basic reduction

Since the data from the observations of NGC 1978 were already used in a publication (Lederer et al., 2009) and were therefore available fully reduced and calibrated for this thesis, this and all following sections will focus on reducing and calibrating the data of NGC 1848, which saw just some basic reduction steps with bias-, dark- and flatfield-reduction.
To correct for the background-brightness, it is in our case not necessary to use the chopping-nodding-technique which was described in section 1.4 and which is mandatory for IR imaging and low-resolution spectroscopy. Instead, the stare/nod-technique can be used, which is more time-efficient since all object-frames taken can also be used to extract spectra. A set of 4 observations per target star was obtained, each with a slight offset. By subtracting the object-frames from each other it is possible to reduce the background-brightness from $\approx$ 50 counts to almost zero. This leaves us again with 4 frames per observed object, each with a positive and a negative spectrum on it and practically no background, illustrated in Fig. 3.1.

3.3 Extraction of spectra

For the extraction, the 'apall'-task of the IRAF-package was used, which allows to set parameters like aperture size and background-areas freely, and which is also able to trace the spectrum on the frame. The spectrum had to be traced and extracted separately on each object-frame, since its position on the frame varies from frame to frame. This means, of course, that the aperture-sizes and the background-regions vary throughout the sample, due to various object luminosities, background objects or 'cosmics'. The variations, however, were kept as small as possible. The four one-dimensional spectra of each of the target- and standard-stars were then added up, before further calibration is taking place. An example of extracted and added up spectra is shown in Fig. 3.2.

3.4 Removal of telluric lines and normalization

For this step, the IRAF-task 'telluric' was used. It requires in addition to the object-spectra data from a 'hot' standard star as a reference. The idea is, that the otherwise in this wavelength-range featureless calibration spectrum of a standard star contains only atmospheric (telluric) features and, thus, allows the removal of these lines from the object-spectra. Therefore the observations included also the spectra of two standard-stars (HD33875 and HR591), although just HD33875 was needed for this step of the data reduction. The task uses a simple Beer's law to scale the calibration spectrum, and it can also shift it in wavelength if necessary. This spectrum is then divided into the object spectrum to remove the telluric lines. To iterate the best fitting parameters (shift and scale), three versions with slightly different settings are shown, together with the calibration and/or data-spectrum (Fig. 3.3); by selecting the best fitting setting and adjusting the parameters again, the iteration can be continued until the result is satisfying: the stellar lines are still visible and the telluric ones are gone without leaving big 'jumps' in the spectrum. Although all these steps would also be possible by using 'implot' (or similar) and the built-in arithmetic tasks of IRAF, this procedure would be quite time-consuming and tedious; the 'telluric' task speeds up the process. As a convenient side effect, the task also flattens the spectra and, thus, makes, due to the narrow wavelength-range of them, any additional normalization besides a division by the spectrum's continuum flux value unnecessary (Fig. 3.4).

3.5 Wavelength calibration

By using the task 'identify', IRAF offers the possibility to use a combination of manually found lines and database values to perform the wavelength calibration for the data. Additionally, the use of a spectral line atlas, in this case the digital issue of the Arcturus-atlas (Hinkle et al., 1995), is necessary to find and identify some lines on which the routine can start working on, please refer to Table (3.3) and Table (3.4) for details on the lines used. After providing some initial guesses, the task finds additional lines by itself, in the best case without misidentified lines. Such ones can be removed manually later, if the mistake is made obvious by bad fitting results. Once a good fitting solution for the dispersion is found, it can be applied to the object-spectra to assign each pixel-coordinate its proper wavelength. Since all the observations of one night are taken with the same instrument and in the same setup, just one calibration per wavelength-range and night needs to be done, which can then be applied to all the other observations of this night, an example of the resulting spectra is shown in Fig. 3.5.

For the calibration of the K-band spectra, a sufficient number of strong and unblended stellar features for the initial guess proved to be hard to find. Therefore, instead of using a target-star for the calibration, the strong telluric lines of the standard-star were used instead. In the range of our H-band spectra however, the earth's atmosphere shows no lines worth mentioning and the identification of the stellar lines was less of a problem, so here exclusively stellar lines were used for the initial guesses.

Table 3.3: List of features in the K-band spectrum of the non-telluric corrected standard-star (HD33875) used for the wavelength calibration. Observations of Nov.11th (the pixel-positions of the observations on Nov.12th vary slightly, the lines used and the wavelengths, however, are practically identical). λ_{in} and λ_{out} refer to the initial guess of the line position and the position after the calibration is done, respectively.

position [pix]	λ_{in} [Å]	λ_{out} [Å]	source
162.80	22840.3235	22840.46	telluric
261.56	22830.4160	22830.32	telluric
270.85	22829.4894	22829.38	telluric
288.45	22827.7348	22827.66	telluric
409.51	22815.7206	22815.74	telluric
485.38	22808.2242	22808.29	telluric
509.29	22805.8640	22805.95	telluric
539.00	22802.9330	22802.99	telluric
751.90	22781.8758	22781.85	telluric
847.84	22772.3080	22772.20	telluric
917.21	22765.3379	22765.30	telluric
979.88	22758.9929	22759.08	telluric

Table 3.4: List of stellar features in the telluric-corrected spectrum of LE14 used for the wavelength calibration; H-band. Observed: Nov. 13th

position [pix]	λ_{in} [Å]	λ_{out} [Å]	source
162.88	15594.3587	15594.380	Fe
351.12	15580.5124	15580.375	CN
427.65	15574.8956	15574.975	CN?
472.97	15571.5695	15571.645	Fe
589.14	15563.0421	15563.156	CN
619.48	15560.8121	15560.700	OH or Fe
653.77	15558.2912	15558.221	Si
812.49	15546.5879	15546.635	Ti
906.69	15539.6070	15539.533	blend
924.04	15538.3176	15538.374	OH

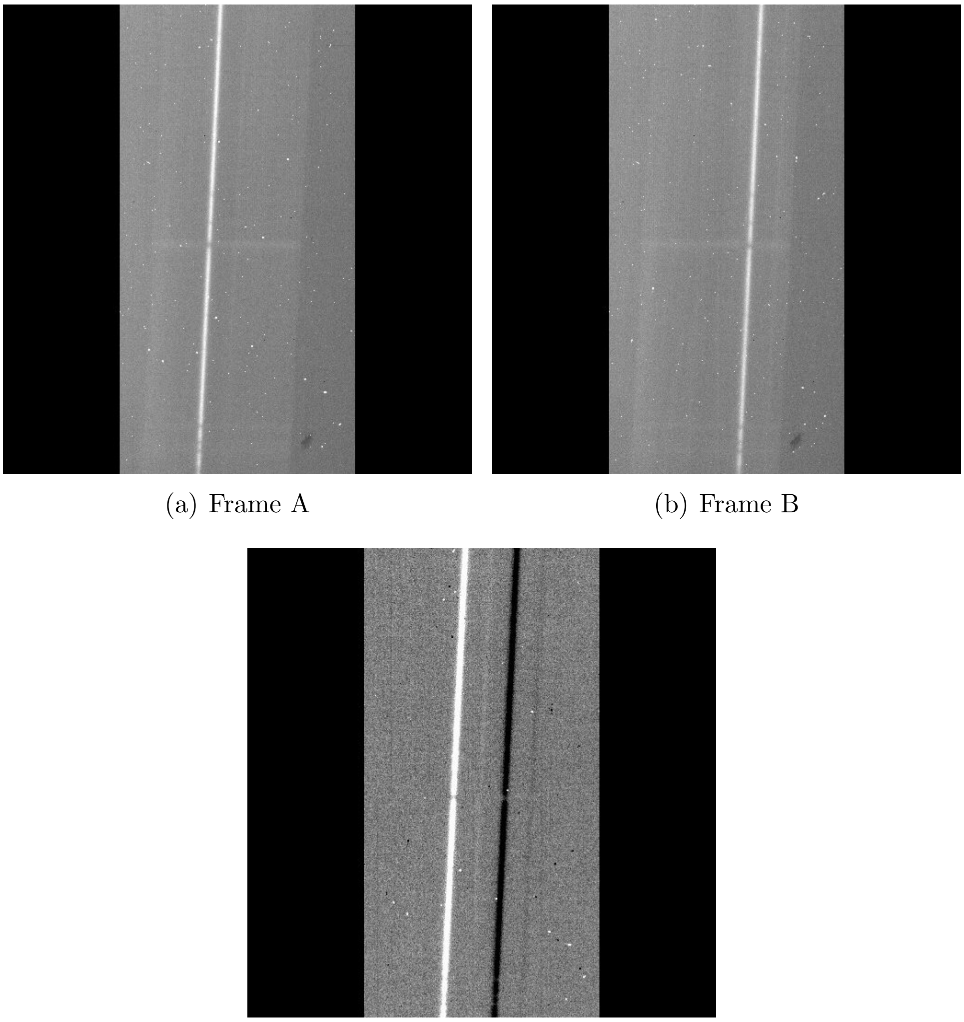

(a) Frame A (b) Frame B

(c) Difference (A-B)

Figure 3.1: Frames A and B show two raw spectra of the target NGC 1846 - LE16, please note the offset of the spectra, while instrumental features remain at the same positions (for example the 'dark spot' in the bottom right corner). What is also apparent is the lower sensitivity of the instrument on the lower end of the frame. The third picture, 'Difference (A-B)' is resulting from the subtraction, it shows both a positive and a negative spectrum, a relatively small background brightness and (at least in theory) no instrumental features.

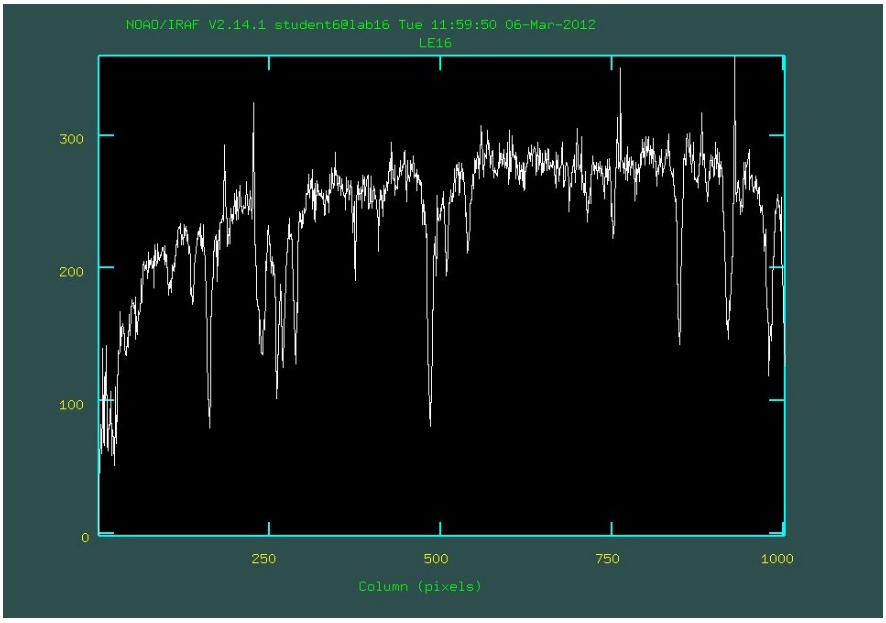

Figure 3.2: This is the average of four extracted spectra of the target NGC 1846 - LE16. It still contains telluric features and the lower sensitivity of the instrument now on the left side of the spectrum is apparent.

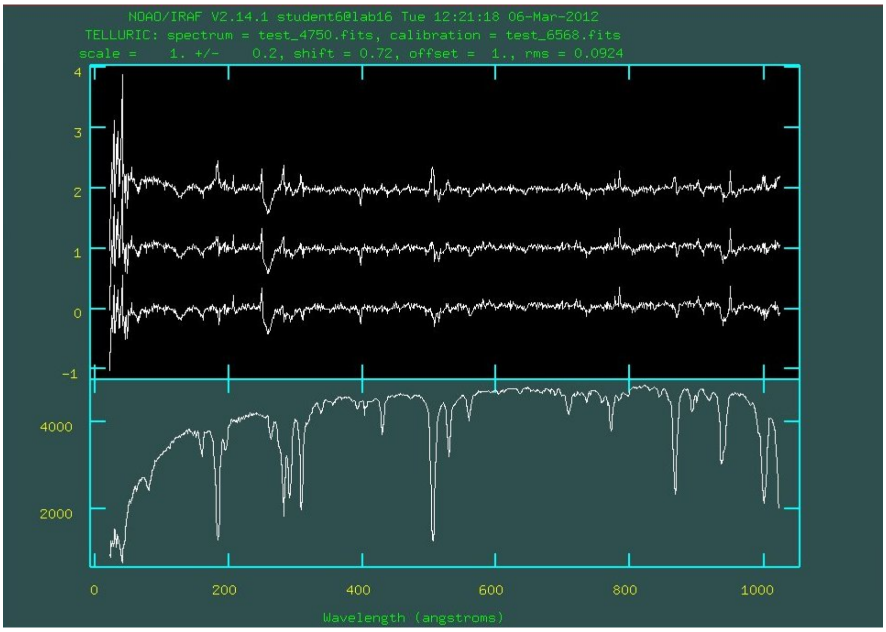

Figure 3.3: Here one can see the 'telluric' task at work. On top 3 object spectra after the correction with different sets of fitting parameters (shift and scaling) is shown. On the bottom you see the calibration spectrum of the standard star, showing only telluric features. This helps at their identification and elimination from the object spectra at further interactive iteration steps.

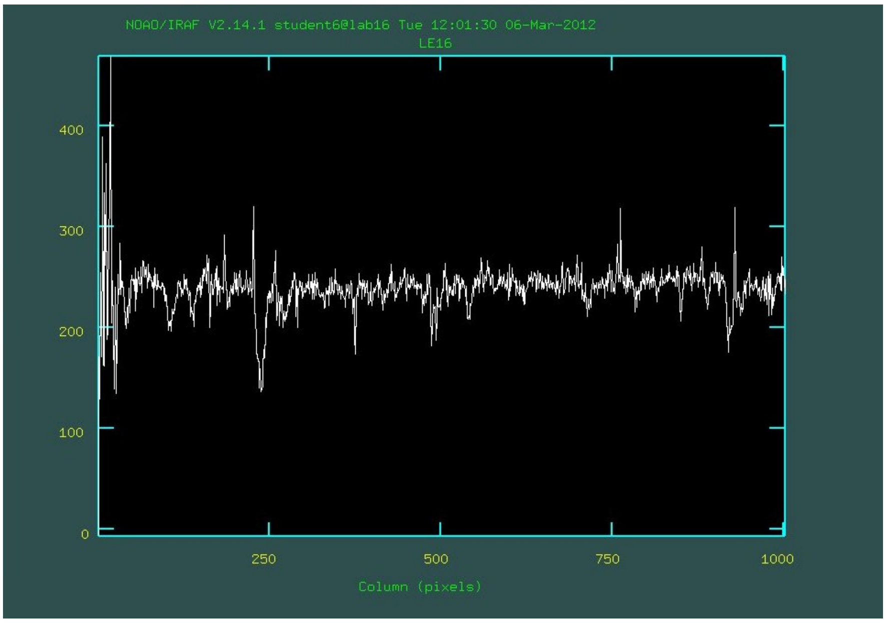

Figure 3.4: This is spectrum of the target NGC 1846 - LE16 after the 'telluric' task was applied. The majority of the telluric features are gone and the spectrum is flattened. However, due to the lower sensitivity on the left side of the spectrum, the operation also introduced some artificial irregularities, which do cause problems for some of our targets since the line R15 lies very close to this area.

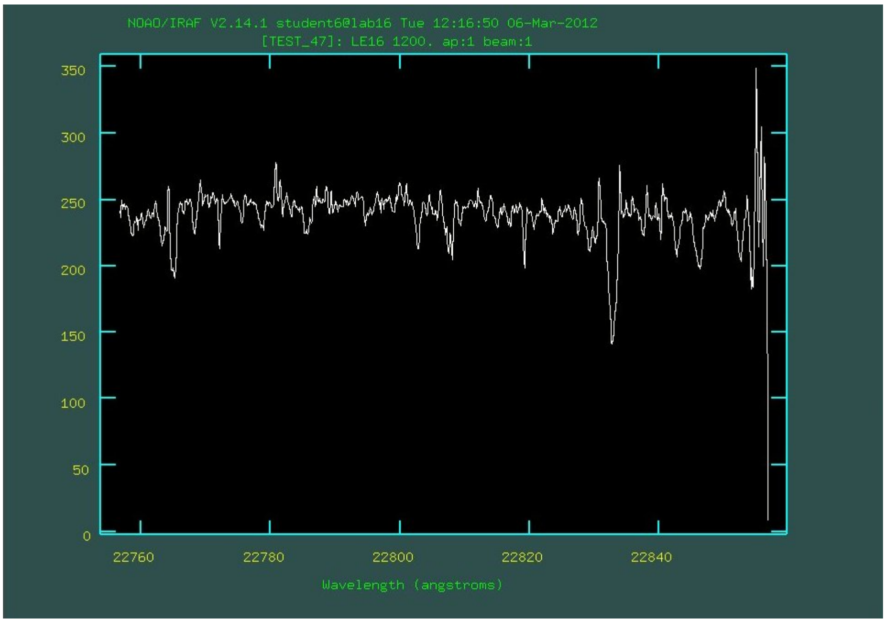

Figure 3.5: This is dispersion corrected spectrum of the target NGC 1846 - LE16. Please note that the spectrum is now reversed (the erratic part is now on the right hand side, at longer wavelength) and that a moderate (box size = 3) smoothing was applied, which makes features better visible without affecting them significantly.

Chapter 4

Modeling

One way to determine the elemental abundances in stars is to compare the observed spectra with synthetic ones. By comparing a model, where all relevant parameters are known, with an observation, where this is usually not the case, it is possible to constrain various quantities of the star. While the idea might sound simple, its numerical application is everything else than trivial. To model a stellar spectrum is usually a two-step process. First it is necessary to compute a model of a stellar atmosphere, which provides the density, pressure and temperature in its various layers. In the second step this model is used to compute the absorption features of the atoms and molecules in the atmosphere under said conditions, which then, hopefully, add up to the same spectrum as the one we observe. This chapter will focus on how to calculate synthetic spectra, how to derive the modelling parameters and, ultimately, how to derive the fluorine-abundances of the observed stars.

4.1 Model stellar atmospheres and the grid

For this work, synthetic stellar atmospheres calculated by the COMARCS code were used, which was recently described in detail by Aringer et al. (2009). It is a variation of the MARCS-code (Model Atmospheres in Radiative and Convective Scheme), published by Gustafsson et al. (1975), please refer also to Jørgensen et al. (1992) and Gustafsson et al. (2008) for more details. The COMARCS-code assumes spherical symmetry as well as both hydrostatic and local thermal equilibrium. This is, of course, just an approximation for an in reality rotating, pulsating and eventually mass-losing star; it is, however, a good one as long as the stars variability is negligible.
A consequence of these assumptions is also chemical equilibrium in the stellar atmosphere. All major contributors to the opacity are taken into account in the model calculation, in particular H_2O, TiO, CO and CN in the oxygen rich case and CO, C_2 and CN in the carbon rich case. The code considers a high number of additional species like SiO, C_2H_2 and H_2S. To calculate the opacities of these molecules the COMA-code (Copenhagen Opacities for Model Atmospheres) is used, first published by Aringer (2000) and initially developed to work in tandem with dynamical atmosphere models to calculate wavelength dependent absorption coefficients. Since its first publication, however, it has been refined and adapted to compute weighted mean opacities for various applications. Based on a given temperature-density or temperature-pressure

structure, provided by COMARCS, COMA computes the abundances of various molecular species in the atmosphere under the assumption of an equilibrium between formation and dissociation (chemical equilibrium). Following these calculations, the opacity at each spectral point can be computed by using the partial pressures of all involved molecules, neutral atoms and ions. These results are then sent back to the COMARCS-code, which can in turn provide a more accurate temperature-density-pressure profile for the star. This makes it possible to iterate successively better models, which can than serve as input for the calculation of synthetic spectra.
For the calculations used in this work, a large grid of such input models was already available. They were computed for a $M_\star = 1.5\ M_\odot$ star with a metallicity of [Fe/H] = -0.4. These numbers fit quite well for both target clusters, although the AGB-stars in NGC 1846 seem to be a bit more massive and less metal-rich (Section 2.2). The grid reaches in effective temperature from T_{eff} = 3500 to 3900K (with a step size of 50K) and in surface gravity from log(g) = 0.0 to 0.5 (Δ log(g) = 0.25). It is therefore covering the parameter range expected for in the observed sample. The abundances for all elements heavier than ^{4}He are scaled with the mean metallicity (so the [x/Fe]-ratios remain constant) with the single exception of carbon, which plays a major role in the atmosphere's chemistry and was therefore scaled independently. This provides another free parameter in form of the carbon/oxygen-ratio, reaching from [C/O] = 0.1 to 0.95. Finally, a carbon isotopic ratio of $^{12}C/^{13}C = 25$, which is a typical values for a star after the first dredge up, and a microturbulent velocity of $\xi = 2.5$ km/s are assumed for all models.

4.2 Spectral synthesis

The COMA-code was developed in the first place to support the COMARCS-code at providing better model atmospheres (Aringer, 2000). Due to its further development (including of atomic transitions from the VALD database (Kupka et al., 2000), extended chemical routines (Falkesgaard, 2001), better handling of ionisation (Gorfer, 2005), effects of dust (Nowotny et al., 2007), inclusion of a higher number of molecular species and, specifically important in this case, HF-line data form the lists by R. H. Tipping (priv. comm.; discussed in Uttenthaler et al. (2008)) it is today capable of a lot more than that and is used in this application to compute synthetic spectra. For this thesis COMA(08) is used.
As input it requires an array of p_{gas}/T or ρ/T-data from the COMARCS-code atmosphere model and information on radius and gas velocity from this model for the radiative transfer as well as fixed values for atomic abundances, isotopic ratios and microturbulence and, optionally, condensation degrees for various dust species. Furthermore, a wavelength-range must be specified, since the model grid is defined by the extension in wavelength and the desired spectral resolution.
For the calculations then, additionally to the chemical molecular equilibrium, which is taken as granted for all covered molecular species, ionization equilibrium for all species which are not covered by the chemical routines is assumed. By this, COMA can account for the continuous, line, and dust absorption. The computed molecular abundances are also part of the program's output, together with the mean opacity and equations of state (T, p, ρ), which are required for the iterative part of COMARCS (Section 4.1).

Table 4.1: Modelling parameters for the stars in NGC 1846 (LE stands for Lloyd Evans 1980). J- and K-magnitudes are 2MASS values (Skrutskie et al., 2006). Data from: Lebzelter et al. (2008)

ID	M_K	M_{J-K}	$T_{eff,f}$ [K]	$log(g)$	v_t [km/s]	C/O	$^{12}C/^{13}C$
H39	11.748	1.093	3650	0.25	3	0.20 ± 0.05	12 ± 2
LE8	11.230	1.208	3550	0.25	3	0.30 ± 0.05	20 ± 2
LE9	11.528	1.143	3650	0.25	3	0.20 ± 0.05	13 ± 2
LE13	10.963	1.293	3600	0.00	7	0.65 ± 0.10	60 ± 5
LE16	11.429	1.104	3600	0.00	4	0.44 ± 0.05	43 ± 2
LE7	11.352	1.206	-	-	-	-	-
LE14	11.543	1.119	-	-	-	-	-
LE15	11.481	1.185	-	-	-	-	-
LW1	11.462	1.115	-	-	-	-	-

In order to obtain synthetic spectra, the total gas opacity, the continuous opacity, the opacities of dust as well as scattering coefficients for different species, together with the various abundances of dust and molecules, are provided. Roughly 10^8 molecular lines from various line lists are being used for the opacity data, covering all major species (CO, CH, C_2, SiO, CN, TiO, H_2O being the more prominent ones). Atomic features are provided by the VALD database (Kupka et al., 2000). To account for the dust opacity, also a number of species like $MgFeSiO_4$, SiC, MgS and SiO_2 can be included. Their condensation degrees and temperatures are provided by the input model and the depletion of elements due to dust formation is included in the chemical routines. The treatment of dust, however, is optional and was not included in this case.
The opacity data are than passed to the (spherical) radiative transfer subroutine 'Sphspec' which provides intensity profiles for each wavelength and is also capable of including dust with different temperatures. The output are intensity profiles and high resolution spectra (R ≈ 300000), which still need to be rebinned by the 'Sphread' subroutine, which also accounts for macroturbulence, normalization, and, optionally, also radial velocity shifts.

4.3 Stellar modelling parameters

The most important model parameters are: effective temperature, surface gravity (log(g)), C/O-ratio, and the macroturbulent velocity (v_t). Most of these values for the target star were already derived and published in the papers by Lebzelter et al. (2008) and Lederer et al. (2009) and are listed in the Tables 4.1 and 4.2 respectively. For some of the targets in NGC 1846, however, these fitting parameters were not known yet, so it was decided to deduce them from their J-K colour index and their H-band spectra (section 4.4.2). Of course, there is a number of other important parameters, like mass and metallicity, but they influence primarily the input models (Section 4.1), and can be assumed to be roughly the same for all stars of one cluster. Therefore, a fixed set of these parameters was used for all the calculations.

Table 4.2: Modelling parameters for the stars in NGC 1978 (LE stands for Lloyd Evans 1980). J- and K-magnitudes are 2MASS values (Skrutskie et al., 2006). Data from: Lederer et al. (2009)

ID	M_K	M_{J-K}	$T_{eff,f}$ [K]	$log(g)$	v_t [km/s]	C/O	$^{12}C/^{13}C$
A	11.116	1.137	3825	0.50	3	0.23 ± 0.05	16 ± 3
LE4	11.199	1.148	3725	0.38	3	0.18 ± 0.03	13 ± 4
LE5	11.387	1.140	3775	0.25	3	0.18 ± 0.05	6 ± 2
LE9	12.259	1.056	3900	0.38	3	0.13 ± 0.03	12 ± 2
LE10	11.802	1.115	3900	0.38	3	0.18 ± 0.05	9 ± 3

4.4 HF-abundance models for NGC 1846

As described in the previous section on COMA (4.2), the program uses the properties of an input model in combination with given elemental abundances to compute the abundances of various molecules in the stellar atmosphere, under the assumption that their formation and destruction are in an equilibrium. While some of the fitting parameters (temperature, log(g) and the C/O-ratio) are set by selecting the right input-model from the grid, others are set by changing the various parameter files for COMA and its subroutines. The atmosphere's elemental abundances are provided via an input-file and can be changed independently. Although this is slightly inconsistent with the abundances used to calculate the input models (which are Z-scaled solar values), it does not really matter in the case of fluorine, since it is rather rare and its few molecular lines have no significant impact on the structure of the stellar atmosphere.

For all calculations, the spectral resolution was set to R = 300000, which is way beyond observable values but is necessary to allow for a correct sampling at the rebinning to a reduced and more realistically observable value of R = 50000, which is done by the routine 'Sphread' via a convolution with a Gaussian. To account for the macroturbulent velocity, another convolution with a Gausian is used. The synthetic spectra cover the following wavelength ranges: 4374-4395 cm^{-1} (22750-22860 Å) in the K-band and 6412-6449 cm^{-1} (15505-15595 Å) in the H-band. Both wavelength ranges are slightly shifted to the observed ones to account for the spectral shifts due to the radial velocities of our targets. While COMA(08) also provides the option to calculate a spectrum at a given redshift, this feature was not used, since it was preferred to apply the correction manually for every single star. The reason for this was, that radial velocity values were not available for all observed cluster-members, and the presence of a strong iron-line (at ≈ 22814 Å) in the observed K-Band spectra made the manual correction relatively easy.
For each star four models with various fluorine-abundances (log(F/H) = -7.64, -7.84, -8.04 and -8.24) were calculated by default, which usually proved to be sufficient to derive abundances. In some cases, however, it was necessary to increase this 'window', so the models cover actually a range of log(F/H) = [-7.04 : -8.44] with a step size of typically 0.2, in some rare cases also a smaller step size of 0.1 was used. This proved to be a waste of computing time however, because the influence of the input-parameters uncertainty on the synthetic spectra is roughly in the same size as a change in log(F/H) of 0.1 (shown in more detail in the section 4.4.1). Lowering the value below log(F/H)

= -8.44, what might be necessary in one single case (Fig.5.5), is rather useless, since below this value the observed features become too weak to distinguish them reliably from the noise.
An important detail to note, however, is that since all spectra were calculated with a metallicity of [Fe/H] = -0.4 and all elements heavier than ^{4}He are scaled with iron, the real values of the fluorine abundance in the models is by the same value lower. Because the input file uses solar-like abundances to start with and above mentioned fluorine abundance numbers are entered there (and later scaled by COMA), these numbers will be used through the text despite this offset. While it will be necessary to take this into account if comparing these values to the ones published in other works, for the calculation from log(F/H) to [F/Fe] here it can be neglected, since all [x/Fe]-ratios (besides H and He) remain constant.
The computing time for each spectrum is rather moderate, due to its limited spectral range. The computation of one single spectrum takes between 10 and 15 minutes on a standard desktop PC, so with a grid of 4-5 spectra with various fluorine-abundances for each observed star, this adds up to roughly one hour per target.

4.4.1 Parameter study

In order to familiarize myself with the impact of the various fitting parameters, a short parameter study was made by computing a number of synthetic spectra and changing just one of the parameters at a time. The results of this are presented on the following pages, but to quickly sum it up, temperature (Fig. 4.1) and C/O ratio (Fig. 4.3) have the biggest impact on the shape of the model spectrum in the observed range. While for the shape of the spectral lines, the macroturbulent velocity (Fig. 4.4) is important as well, the surface gravity (Fig. 4.2) is, in comparison to the other parameters, rather neglectable.
If not stated otherwise, all spectra in this study were computed with: T_{eff} = 3600K, log(g) = 0.25, C/O = 0.2, v_t = 3km/s and log(F/H) = -8.04. The only exception from this are the C/O ratio models, which were computed at a lower surface gravity (log(g)=0.00), since this allowed the use of a wider range of C/O ratios from the input stellar structure models.
The last plot illustrates the influence of the carbon isotopic ratio on the blended HF-feature in the spectra of the targets in NGC 1978. Therefore, a different wavelength range is shown and a higher fluorine abundance is used, to make the HF feature better visible.

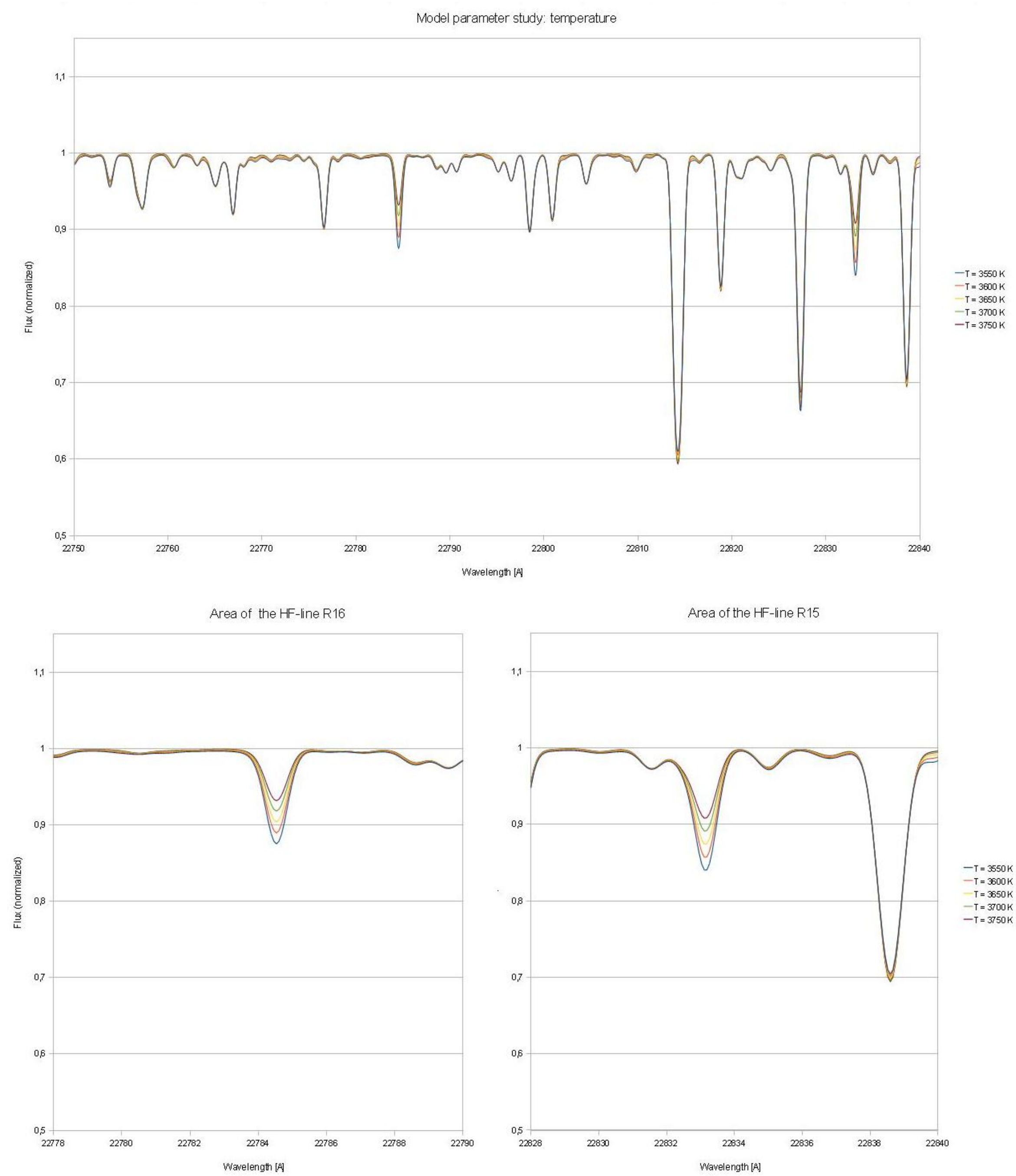

Figure 4.1: Models with varying effective temperature. The other fitting parameters are: log(g) = 0.25, C/O = 0.2, v_t = 3km/s and log(F/H) = -8.04. Please note the high temperature dependency of both HF-lines, while the rest of the spectrum stays rather unaffected.

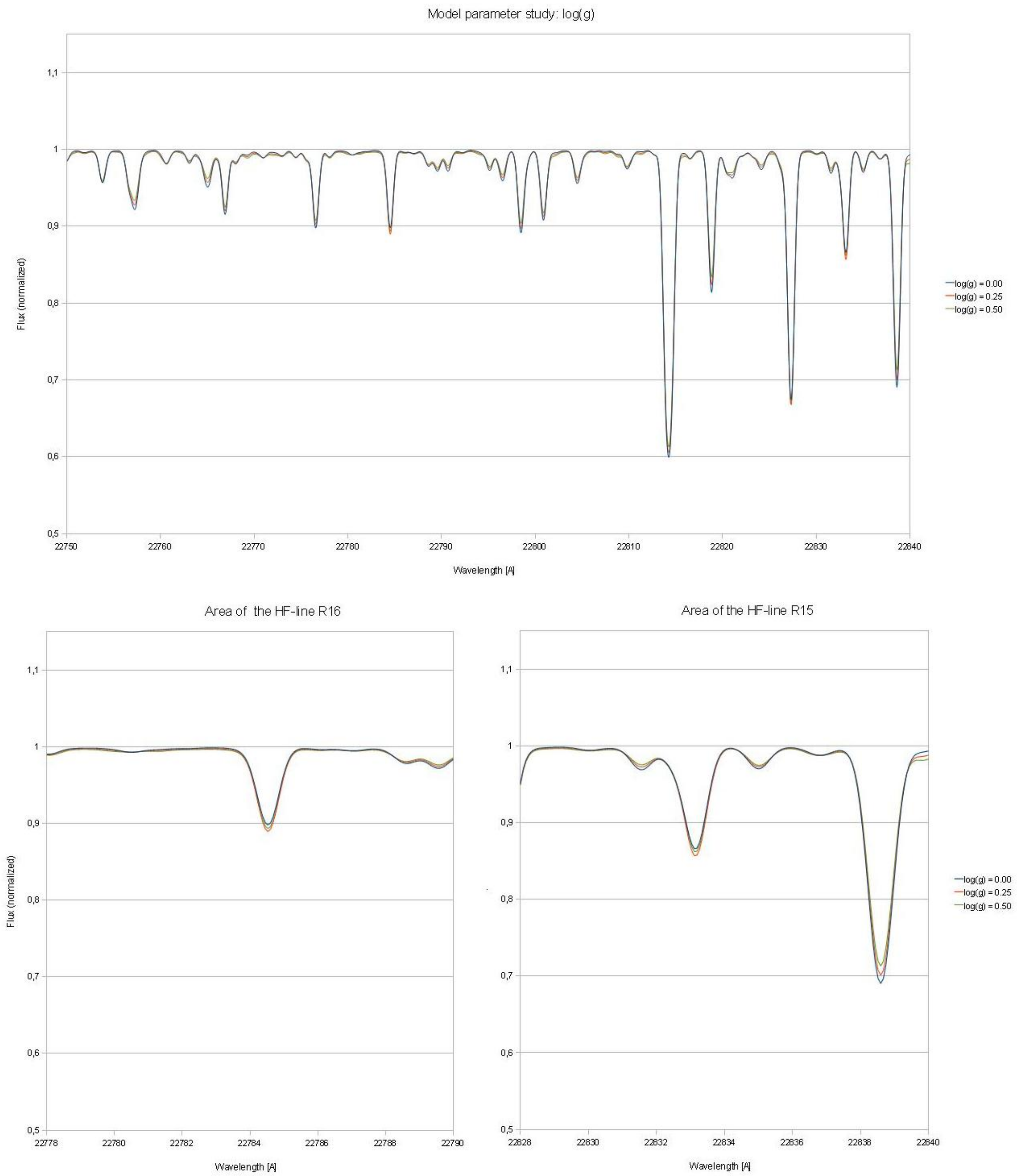

Figure 4.2: Models with varying surface gravity. The other fitting parameters are: T_{eff} = 3600K, C/O = 0.2, v_t = 3km/s and log(F/H) = -8.04. In comparison to the influence of the other studied parameters, log(g) has just a minor influence.

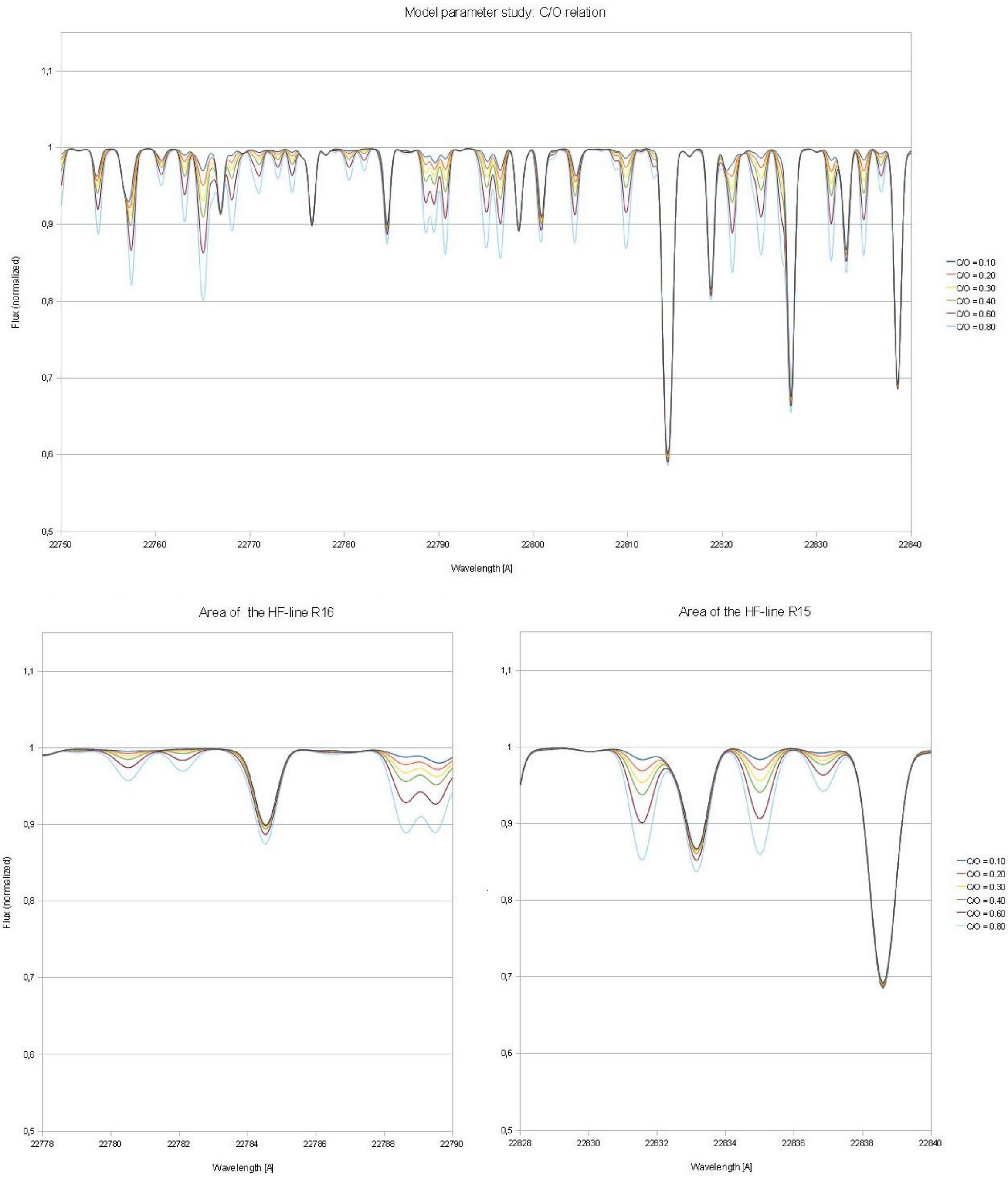

Figure 4.3: Models with varying C/O ratio. The other fitting parameters are: T_{eff} = 3600K, log(g) = 0.00, v_t = 3km/s and log(F/H) = -8.04. Overall, the C/O ratio has a strong influence on the spectrum. The depth of both HF-lines, however, is not too much affected, as long as the ratio is small.

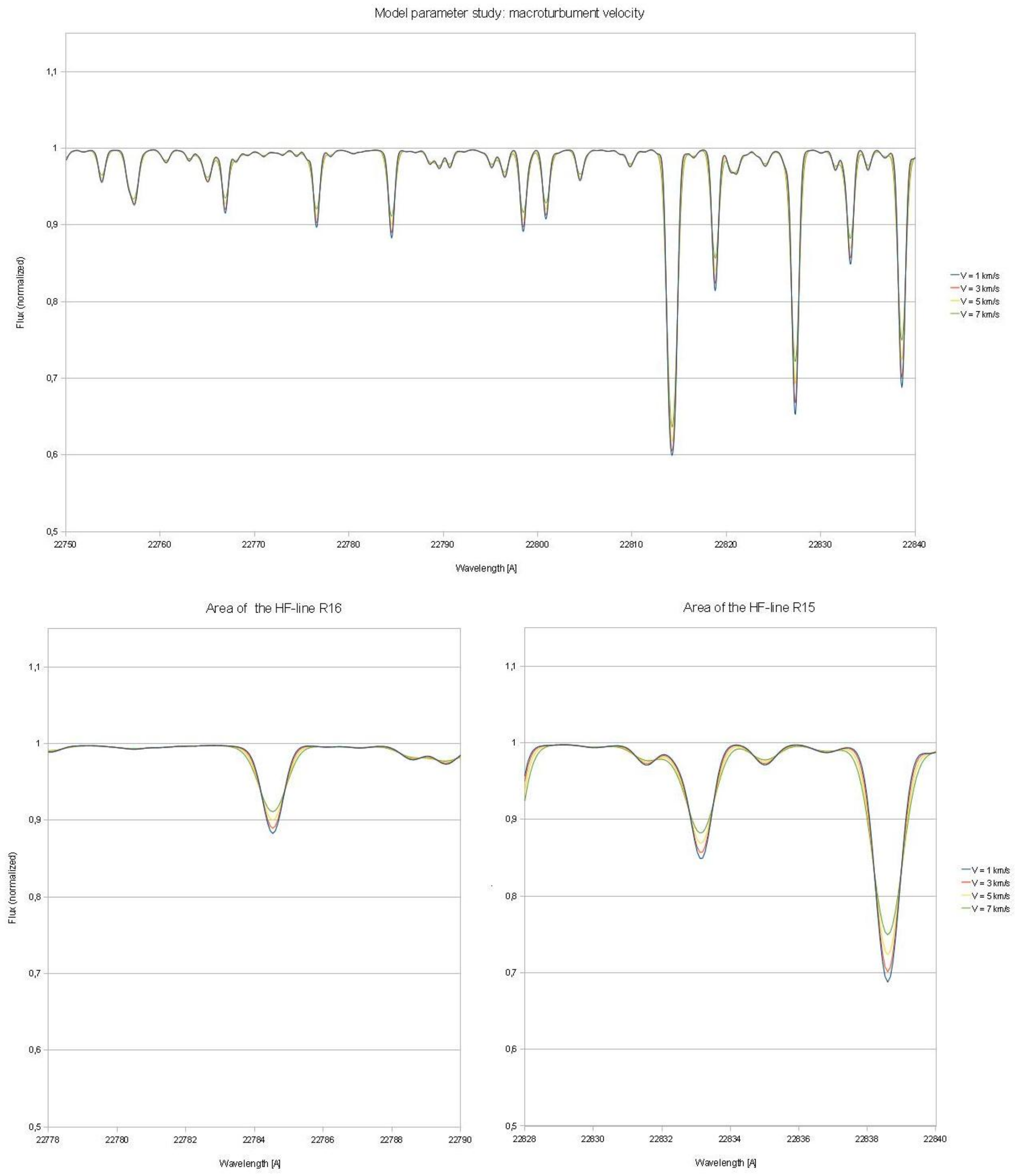

Figure 4.4: Models with varying macroturbulent velocity. The other fitting parameters are: T_{eff} = 3600K, log(g) = 0.25, C/O = 0.2 and log(F/H) = -8.04. While the overall impact seems to be low, a higher v_t makes all features appear shallower and broader.

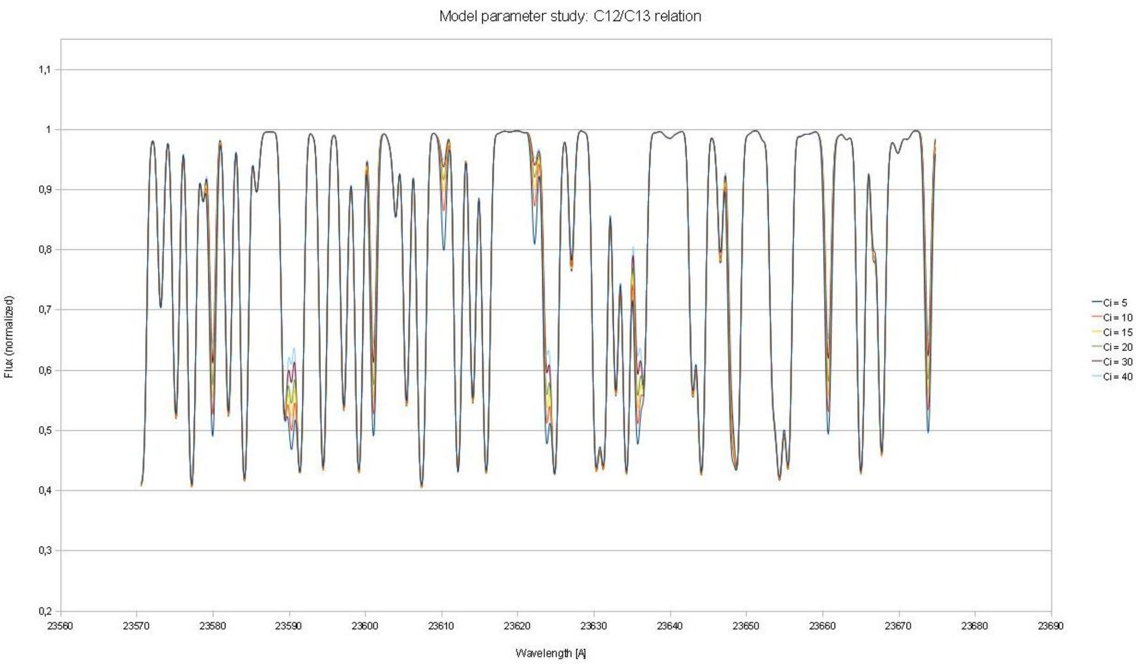

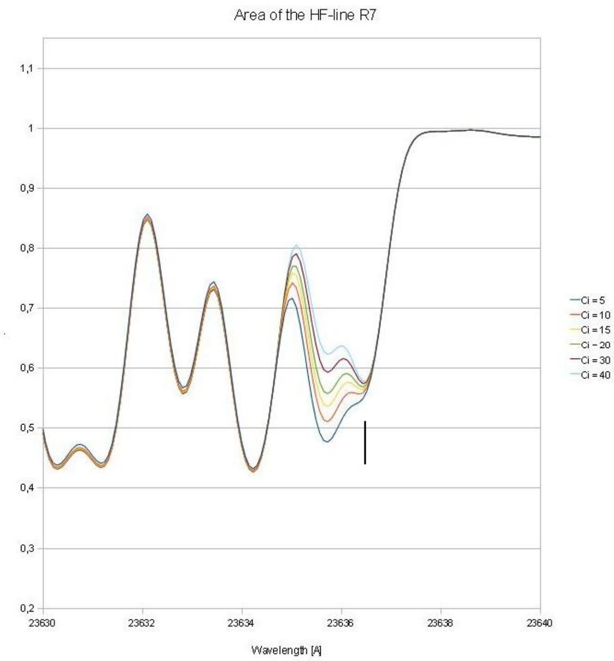

Figure 4.5: Models with varying carbon isotopic ration (Ci = $^{12}C/^{13}C$). The other fitting parameters are: T_{eff} = 3600K, log(g) = 0.25, C/O = 0.2 and log(F/H) = -7.84. This study is made in a different wavelength range, since it is relevant only for the NGC 1978 models. The position of the HF-feature is marked. The depth of the ^{13}CO-feature is clearly anti-correlated to the $^{12}C/^{13}C$ ratio. Furthermore, please note that the depth at the position of the HF-feature is much less affected at higher Ci-values.

4.4.2 Obtaining the missing fitting parameters

To obtain the missing parameters in Table 4.1, it is first necessary to estimate the stars' effective temperatures from the J-K colour indices (Skrutskie et al., 2006). This value can then be used for some 'initial-guess' models in the H-band with various C/O ratios, to deduce also this critical value. While the values of log(g) and v_t are less critical for initial K-band model fitting and can be estimated by some iterations, the $^{12}C/^{13}C$-value is not critical for the NGC 1846 observations, since the points of interest are primarily the two HF-lines R15 and R16, which are unblended and, thus, not affected by this ratio.

To derive the unknown effective temperatures, the color-indices of the already previously observed cluster members (LE8, LE9, LE13, LE16 and H39) are plotted as function of their effective temperatures. A simple linear regression then provides a formula to estimate the temperatures of LE7, LE14, LE15 and LW1 from their colour-index, which is, of course, by no means perfect and can be done only due to the limited temperature-range, since the T_{eff}/(J-K) relation is not linear and can be approximated by a linear function just within a small range. Therefore, the deduced temperatures have to be used with some caution and an uncertainty of ± 50K has to be taken into consideration. The results are shown in Table 4.3. Two stars have temperatures around 3600K while for the other two a T_{eff} = 3625K seems to be more appropriate. However, since the grid of atmosphere structure models has a step size in temperature of Δ T_{eff} = 50K, the same input models (T_{eff}) are used for all four of them in the next step (estimation of C/O ratio). To compute the synthetic K-band spectra for the estimation of the fluorine abundance, however, input models with both T_{eff} = 3600K and 3650K were used and the results from both input values are consistent.

Based on the values for the temperature, a grid of synthetic H-band spectra with varying C/O ratios was calculated, while everything else was kept constant. The C/O-ratio can be estimated by comparing the synthetic with the observed spectra. In contrast to the models with varying fluorine-abundances, it is not sufficient just to change a number in the input-files, since the C/O-ratio has a significant impact on the stellar structure and, thus, also different input models have to be used to compute the synthetic spectra. The spectra were calculated with a spectral resolution of R = 300000 (and later rebinned to R = 50000), cover a wavelength range of 15505-15595 Ångstrom (6412-6449 cm^{-1}), and range in C/O from 0.1 to 0.9 with step size of 0.1. By this method it was possible to derive the 4 unknown C/O-values for the targets, which all lie close to C/O = 0.2 (± 0.05). Furthermore, also the high C/O ratio of LE13 derived by Lebzelter et al. (2008) could be confirmed, since for this star a new H-band spectrum was available too.
The surface gravity (log(g)) and the macroturbulent velocity (v_t) have similar effects on the appearance of a K-band spectrum. While a higher surface gravity generally leads to slightly shallower features, some features are not affected and some are even getting deeper. Overall, however, the effect is relatively small. A higher macroturbulent velocity on the other hand, makes all individual features 'wider and shallower', so the spectrum looks less 'sharp'. Both values can be roughly estimated by computing a number of K-band models with varying parameters and comparing them with the observed ones. Due to the small influence of both values, however, it proved very

Table 4.3: Additional modelling parameters for the stars in NGC 1846 which were not observed in Lebzelter et al. (2008) (LE stands for Lloyd Evans 1980). J- and K-magnitudes are 2MASS values (Skrutskie et al., 2006). Note the relatively large error bars for both $log(g)$ and v_t.

ID	M_K	M_{J-K}	$T_{eff,f}$ [K]	$log(g)$	v_t [km/s]	C/O
LE7	11.352	1.206	3600 ± 50	0.25 ± 0.25	3 ± 2	0.20 ± 0.05
LE14	11.543	1.119	3625 ± 50	0.25 ± 0.25	3 ± 2	0.20 ± 0.05
LE15	11.481	1.185	3600 ± 50	0.25 ± 0.25	3 ± 2	0.20 ± 0.05
LW1	11.462	1.115	3625 ± 50	0.25 ± 0.25	3 ± 2	0.20 ± 0.05

difficult to estimate exact values. High macroturbulent velocities ($v_t \leq 5$) and low surface gravities (log(g) < 0) could be excluded. As a result, a standard set of stellar parameters (see Tab. 4.3) was used for all four target stars.

4.5 HF-abundance models for NGC 1978

Models for the red giants in NGC 1978 were calculated in a similar way as the ones for NGC 1846, but in a slightly different wavelength range. Furthermore, the observed spectra were shifted to zero velocity already in the beginning, so there was no need to worry about that value and, in retrospect, doing so with the observed spectra of the first cluster (NGC 1846) might have saved some trouble there. Additionally, there was already a grid of synthetic spectra available, covering the range of T_{eff} = 3700-3900K in temperature. They were all computed with a C/O-ratio of 0.15, which is a good approximation for the targets in this cluster since they show a quite homogeneous pattern. Models for log(g) = 0.25 and 0.50 are part of the grid. This covers pretty much all 5 stars in the sample and only LE5 needed some 'special treatment' in the form of additional calculations. The grid-range in the fluorine-abundance is similar to the one calculated for the other cluster, reaching from log(F/H) = 7.44 to 7.84[1], which proved to be adequate for all the targets in NGC 1978.
There is, however, one significant difference in the modelling of stellar spectra between those two clusters. Due to the fact that a different HF-line was used, which is blended with a strong ^{13}CO-line, it was necessary to include an updated CO-linelist in the calculations for NGC 1978 since COMA failed to reproduce the observed spectra with the standard lists used. Additionally, the by the input models restricted carbon isotopic ratio (^{12}C/^{13}C = 25) is significantly different from the values published by Lederer et al. (2009) and shown in Tab.4.2. To compensate for this, however, the carbon isotopic ratio, or rather the ratio between various carbon-bearing modules, can be modified manually for the calculation of the synthetic spectra. While it is in contradiction to the input models used, this does not really matter, since the carbon isotopic ratio has only a negligible influence on the structure of the model atmospheres but a significant one in the synthetic spectra (Fig. 4.5).

[1]These values are still being scaled with the mean metallicity, [Fe/H]=-0.4; please refer to section 4.4 for more details.

Chapter 5

Comparison

While the previous two chapters described how to gain observed and synthetic spectra, this chapter focuses on the comparison between them and how to deduce values for the fluorine abundance and the C/O ratio. This can be done using any plotting program (Gnuplot, Origin, Excel). Here the spreadsheet-module of the Open Office package (OpenOffice, 2012) was chosen for the task. While this might not look like a very professional choice, the program is free, it provides all the tools required at this stage and it allows for an interactive radial velocity correction once it is set up right.

5.1 Putting observation and model together

Since the continuum of the observed spectra is already flattened by the 'telluric' task but not yet normalized, the spectra need to be divided by the value of their estimated continuum flux, so the flux at each spectral point varies between zero and one (normalized flux). This is necessary for two reasons: first, to compare individual stars with each other, compensating for their differing brightness; second, the model spectra are calculated within this interval, and it is less taxing to compensate for one star than for 4-5 models per object. The figures 5.1 and 5.11 show the obtained and normalized K- and H-band spectra of the sample stars in NGC 1846. Figure 5.17 shows the same for the objects of NGC 1978, here, however, the whole data reduction including the normalization was already done by Lederer et al. (2009).

For the spectra of NGC 1846 a correction for the stellar radial velocity had to be applied. This was done by comparison of observation and model. While there are two ways to do this, either by shifting the observed spectrum to zero redshift or by shifting the synthetic spectrum to match the observed one, the first option was chosen, since shifting one observed spectrum is simply easier to handle than shifting 4-5 model spectra per star. In the K-band, a strong iron line at ≈ 22814 Ångstrom was used as the main reference point, the two HF-lines (R15, R16) being the secondary one if they are of sufficient strength. The deduced radial velocities (≈ 235-245 km/s) are not heliocentric values, however, since the earth's orbital velocity at the time of the observation is not taken into account. Furthermore, the use of the HF-lines to correct for the redshift proved to be problematic, since the line list used does not seem to be exact enough and both theoretical line positions therefore show a slight offset from the

observed ones, if the spectra are shifted according to the strong iron line lying between them. This might, however, also be a consequence from a bad wavelength calibration (good zero-point but wrong dispersion-solution), although this option seems rather unlikely, because a number of telluric lines over the whole observed spectral range was used for the calibration. Either way, since measuring the line strength is the main objective of this work, their exact position is just a secondary concern, since usually there are no nearby lines from other sources to mix them up with (R16 is fine, R15 is more problematic).
For the H-band spectra on the other hand, a large number of characteristic features is available to match the oberved and synthetic spectra. As main point of reference, however, the bandhead at $\approx$ 15580 Ångstrom was used. The problems with the relative line positions in the K-band spectra were not an issue here.

By shifting the observed spectra to a radial velocity of zero and by using normalized fluxes, the models provided by COMA can now be compared to the observations directly without any further adjustments.

5.1.1 K-band spectra of NGC 1846

Most of the observed K-band spectra of the targets in NGC 1846 show some erratic behaviour at the right-hand side of the observed range (towards larger wavelengths), which is mostly caused by artifacts from the data reduction. The sensitivity at this end of the detector seems to be rather low in compare to the rest of the CCD; and dividing a small, noise affected number by another small, noise affected number during the telluric-task (please refer to Fig. 3.3) can lead to the effect seen here. Unfortunately, one of the spectral lines investigated (R15) is located in this area and, thus, often cannot be used to estimate the fluorine abundance reliably. The line R16 on the other hand, provides good and reliable values for it, which are usually also supported by the line R15, if the trend in the continuum in this area, which is seen in most spectra, is corrected for.

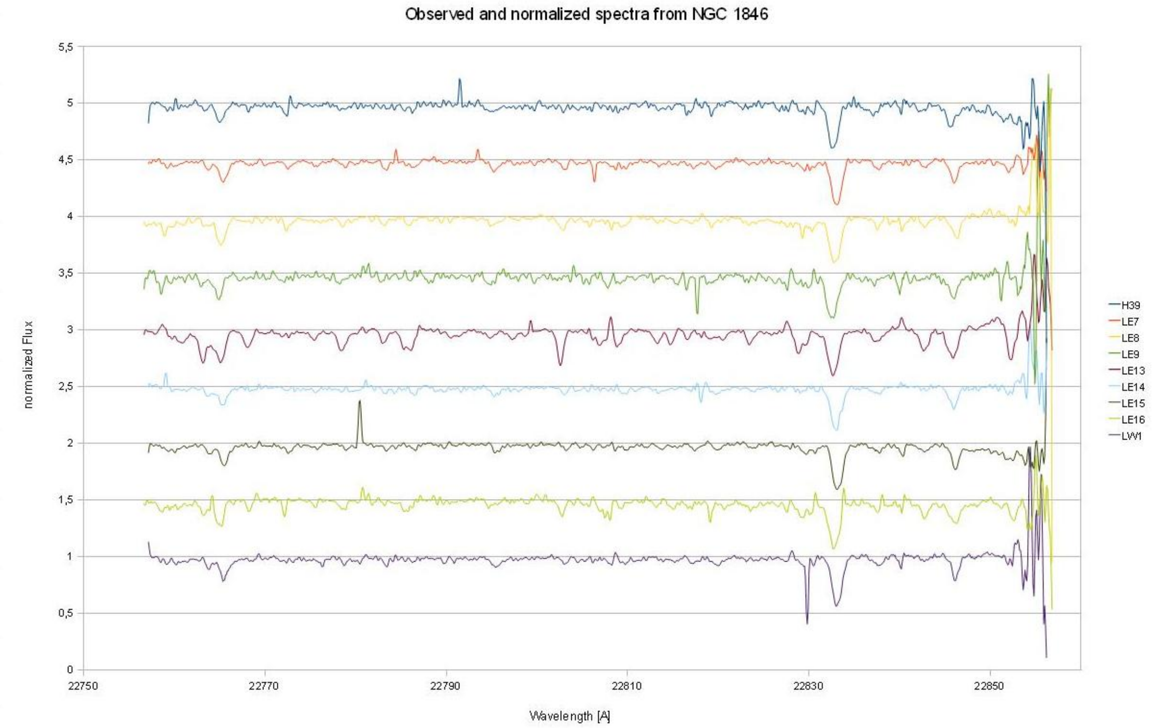

Figure 5.1: The observed, normalized K-band spectra of the targets in NGC 1846. No velocity correction has been applied, therefore a slight wavelength shift between them is visible. To separate individual stars, an artificial offset of 0.5 between the spectra has been added. The erratic behaviour at the right hand side of most spectra is likely caused by a combination of instrumental properties and non-perfect data reduction. Furthermore, also the the emission-line like features in some spectra are just artifacts from the telluric correction and the flattening of the continuum. The two HF-lines are located at ≈ 22803 and 22852 Ångstrom.

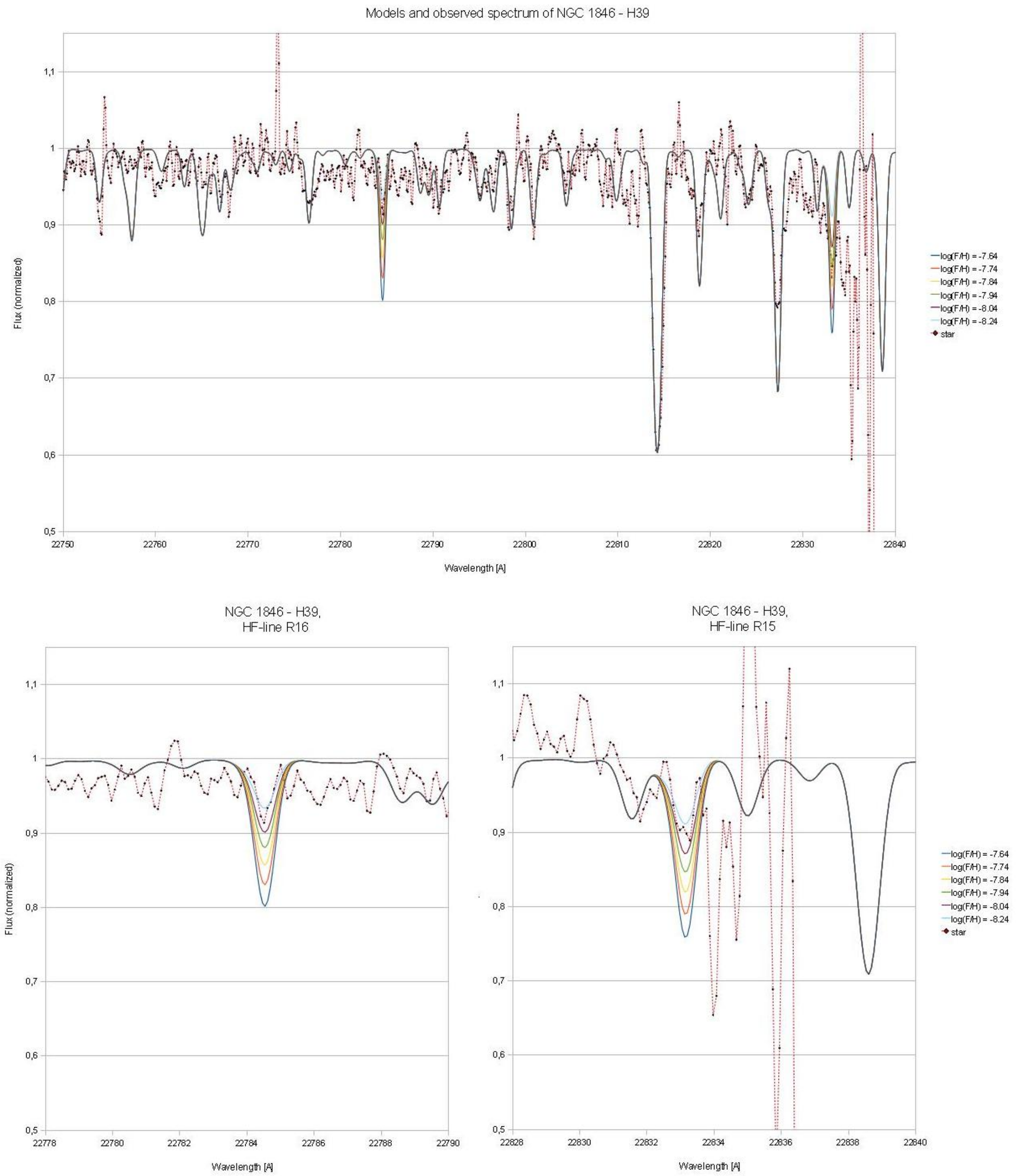

Figure 5.2: Comparison of observed and synthetic spectra for NGC 1846 - H39, showing first the whole observed wavelength range and then a zoom on the two HF-lines. The observed spectrum lies between the models with log(F/H) = -8.04 and -8.24, so a value of -8.14 was adopted. The area around line R15 (bottom right panel) had to be adjusted manually in order to be comparable to the models, so the uncertainty of the data from this feature is significantly higher and less weight is put on the data gathered from it.

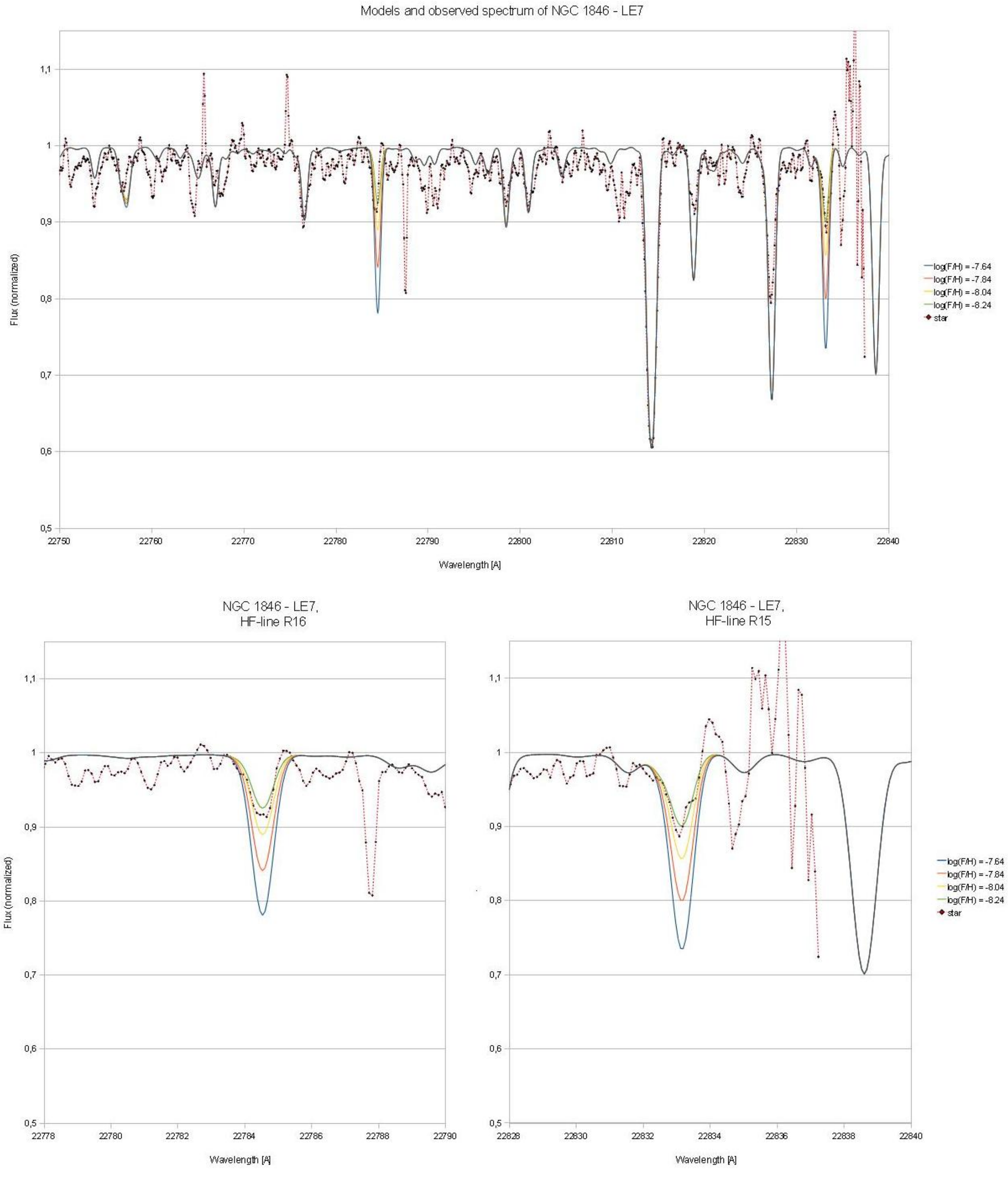

Figure 5.3: Same as Fig. 5.2 for NGC 1846 - LE7. Both HF-lines can be fit best with the models having log(F/H) = -8.04 and -8.24, so a value of -8.14 was adopted.

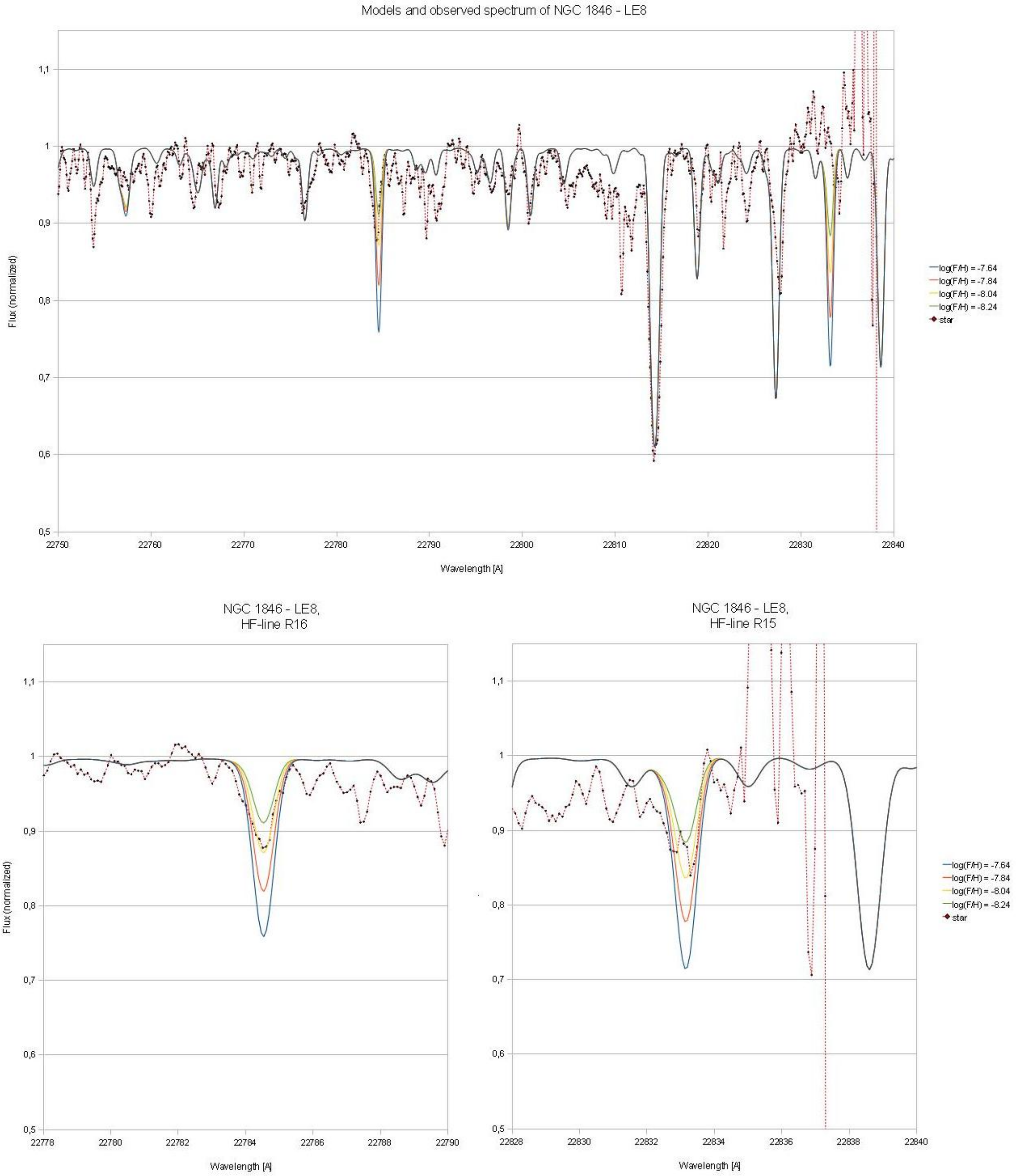

Figure 5.4: Same as Fig. 5.2 for NGC 1846 - LE8. The observed spectrum around the HF-feature R16 is matched well by the model with log(F/H) = -8.04, so this value was adopted. R15 was taken into account, but with less weight (see Fig. 5.2).

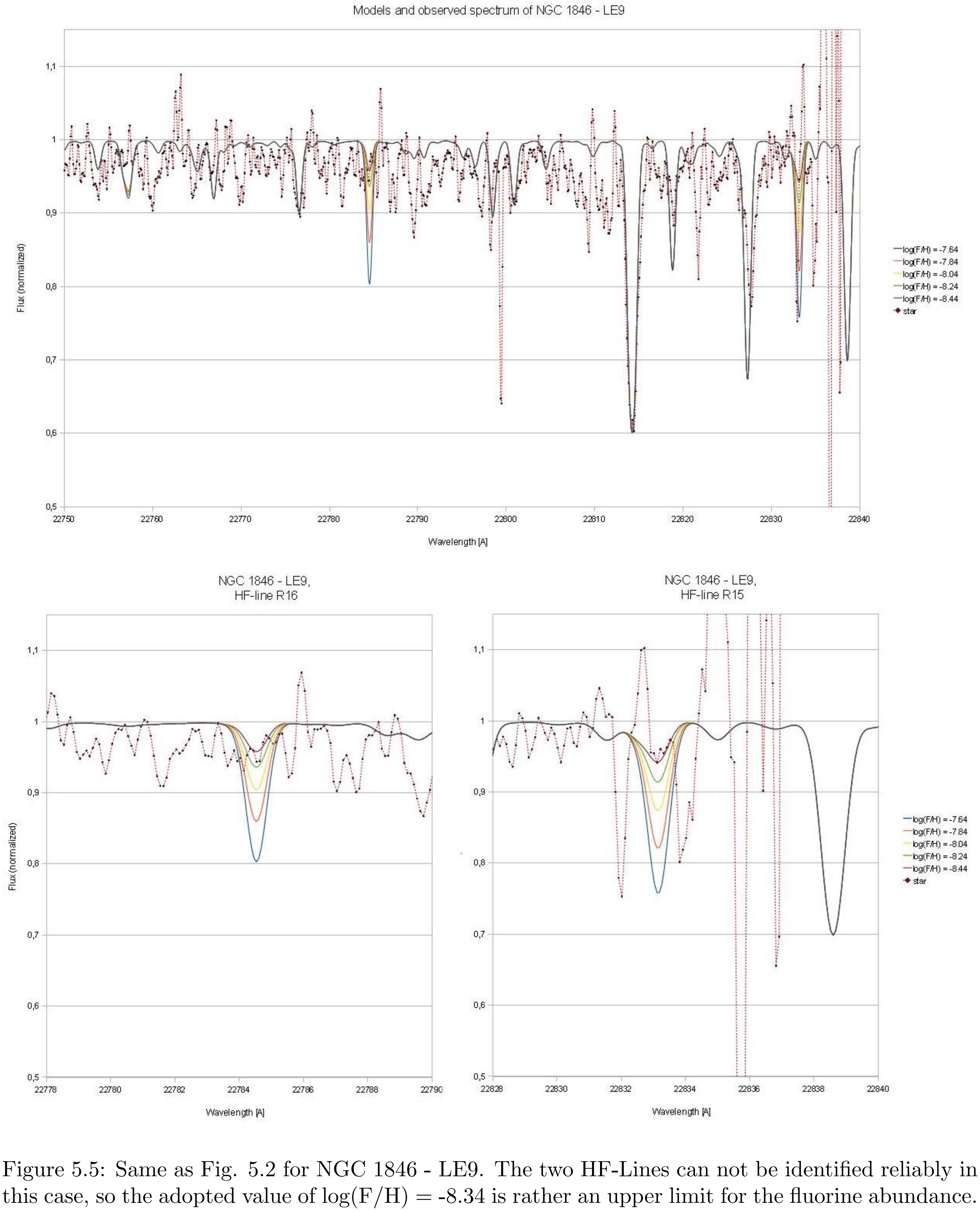

Figure 5.5: Same as Fig. 5.2 for NGC 1846 - LE9. The two HF-Lines can not be identified reliably in this case, so the adopted value of log(F/H) = -8.34 is rather an upper limit for the fluorine abundance.

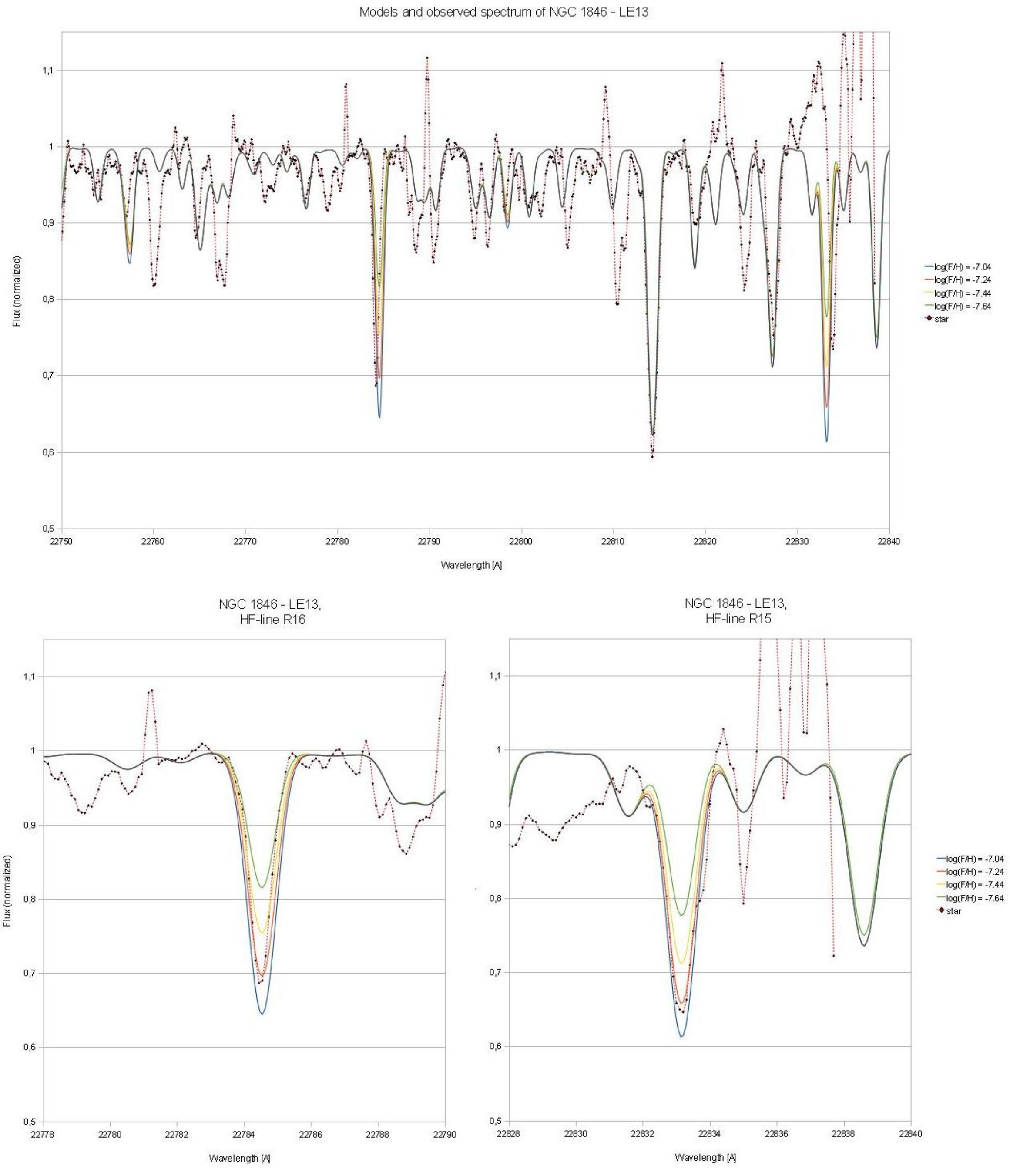

Figure 5.6: Same as Fig. 5.2 for NGC 1846 - LE13. The observed spectrum around the HF-feature R16 is matched well by the model with log(F/H) = -7.24, so this value was adopted. R15 was taken into account, but with less weight (see Fig. 5.2).

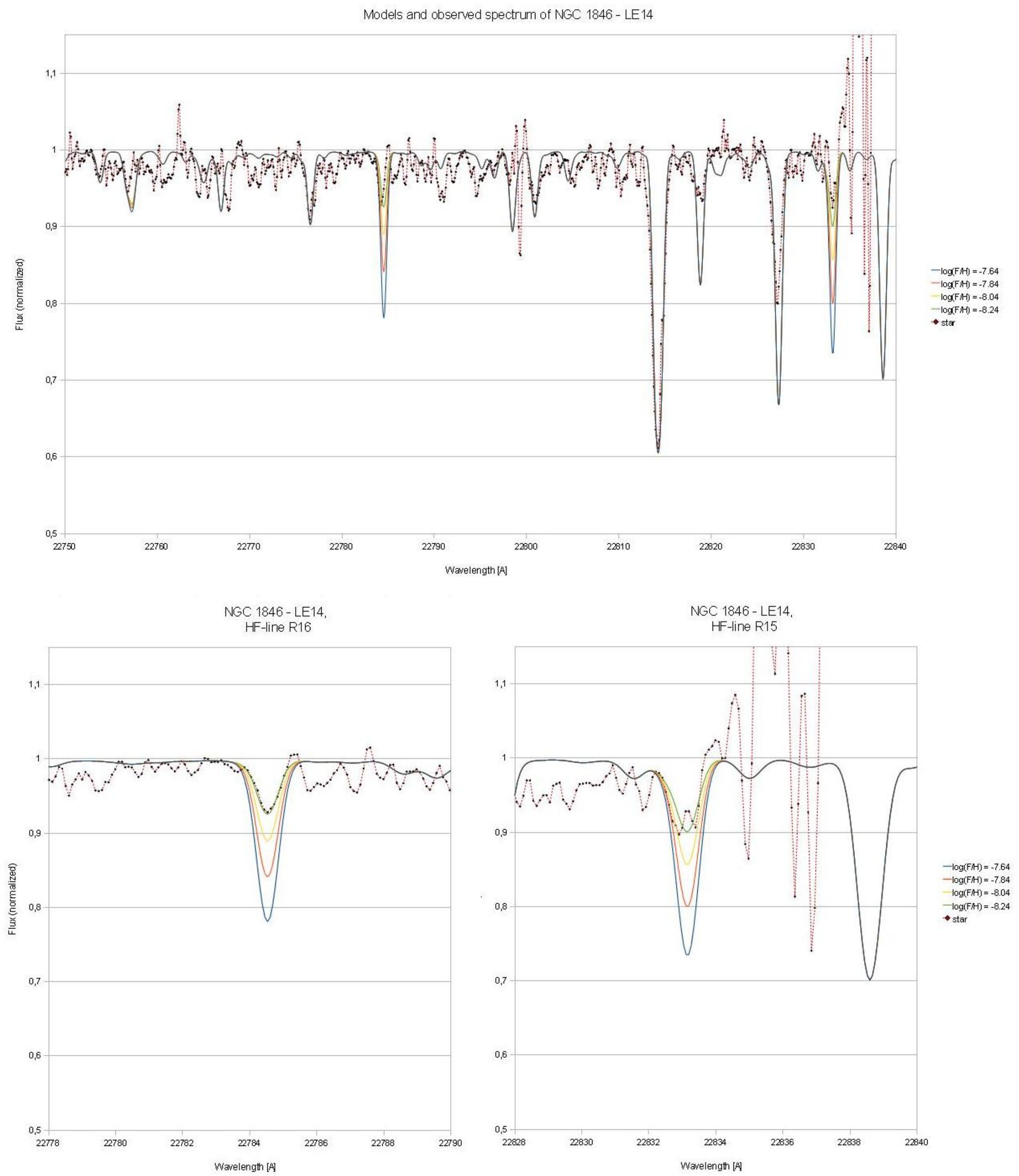

Figure 5.7: Same as Fig. 5.2 for NGC 1846 - LE14. The observed spectrum around the HF-feature R16 is matched well by the model with log(F/H) = -8.24, so this value was adopted. R15 was taken into account, but with less weight (see Fig. 5.2).

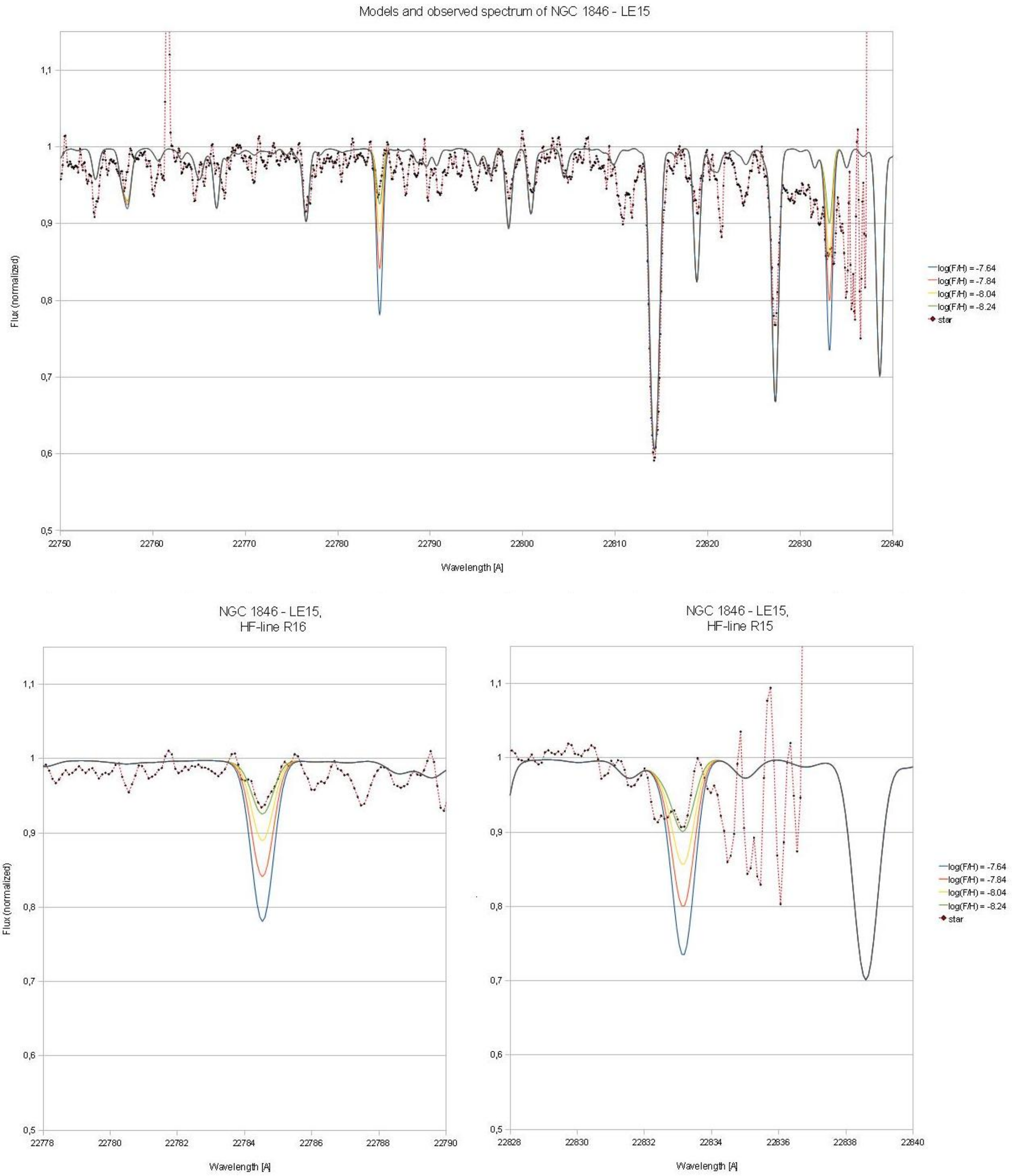

Figure 5.8: Same as Fig. 5.2 for NGC 1846 - LE15. The observed spectrum around the HF-feature R16 is matched well by the model with log(F/H) = -8.24, so this value was adopted. R15 was taken into account, but with less weight (see Fig. 5.2).

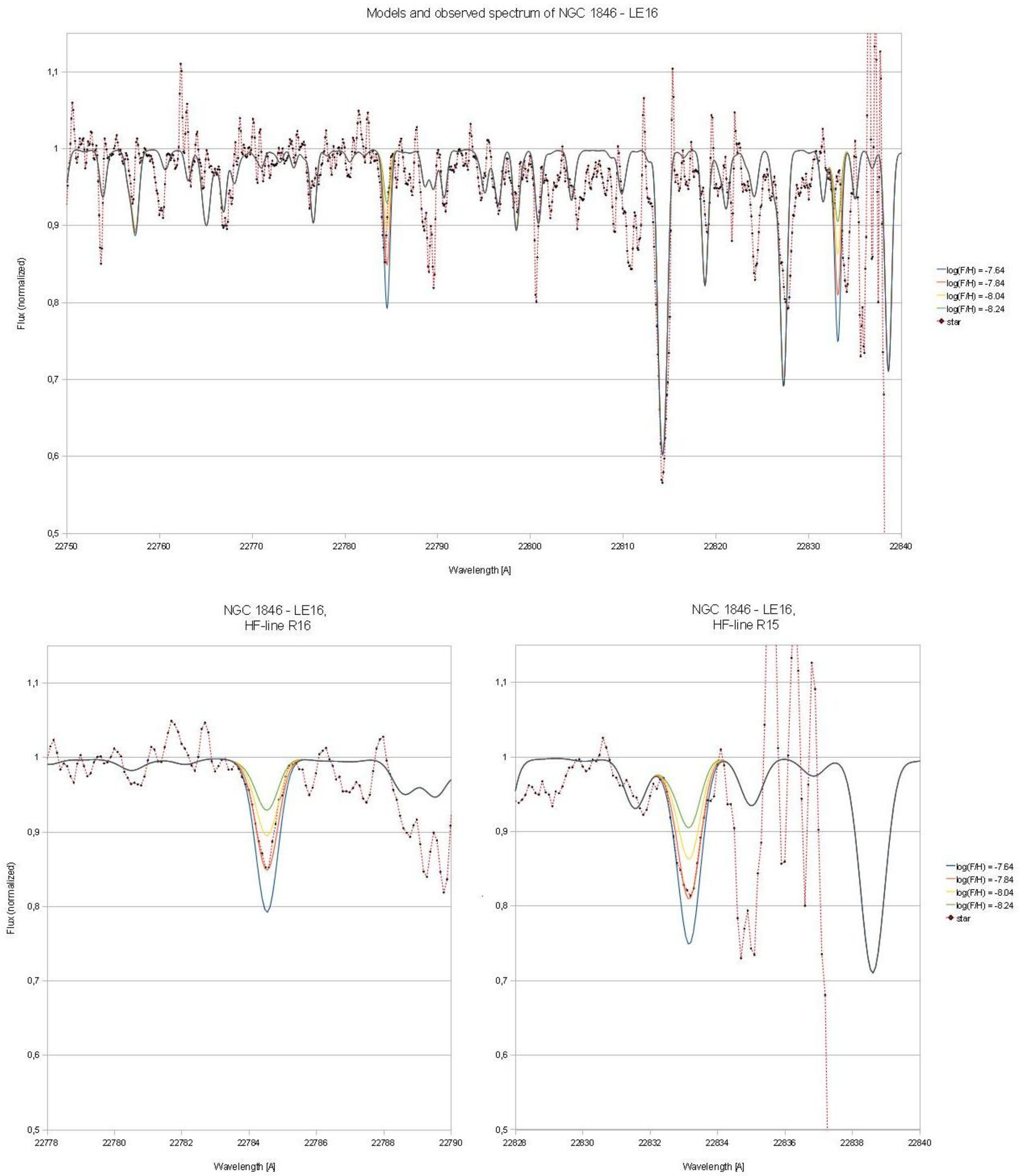

Figure 5.9: Same as Fig. 5.2 for NGC 1846 - LE16. The observed spectrum is matched well by the model with log(F/H) = -7.84, so this value was adopted. In this case, both lines could be fitted successfully without further adjustments.

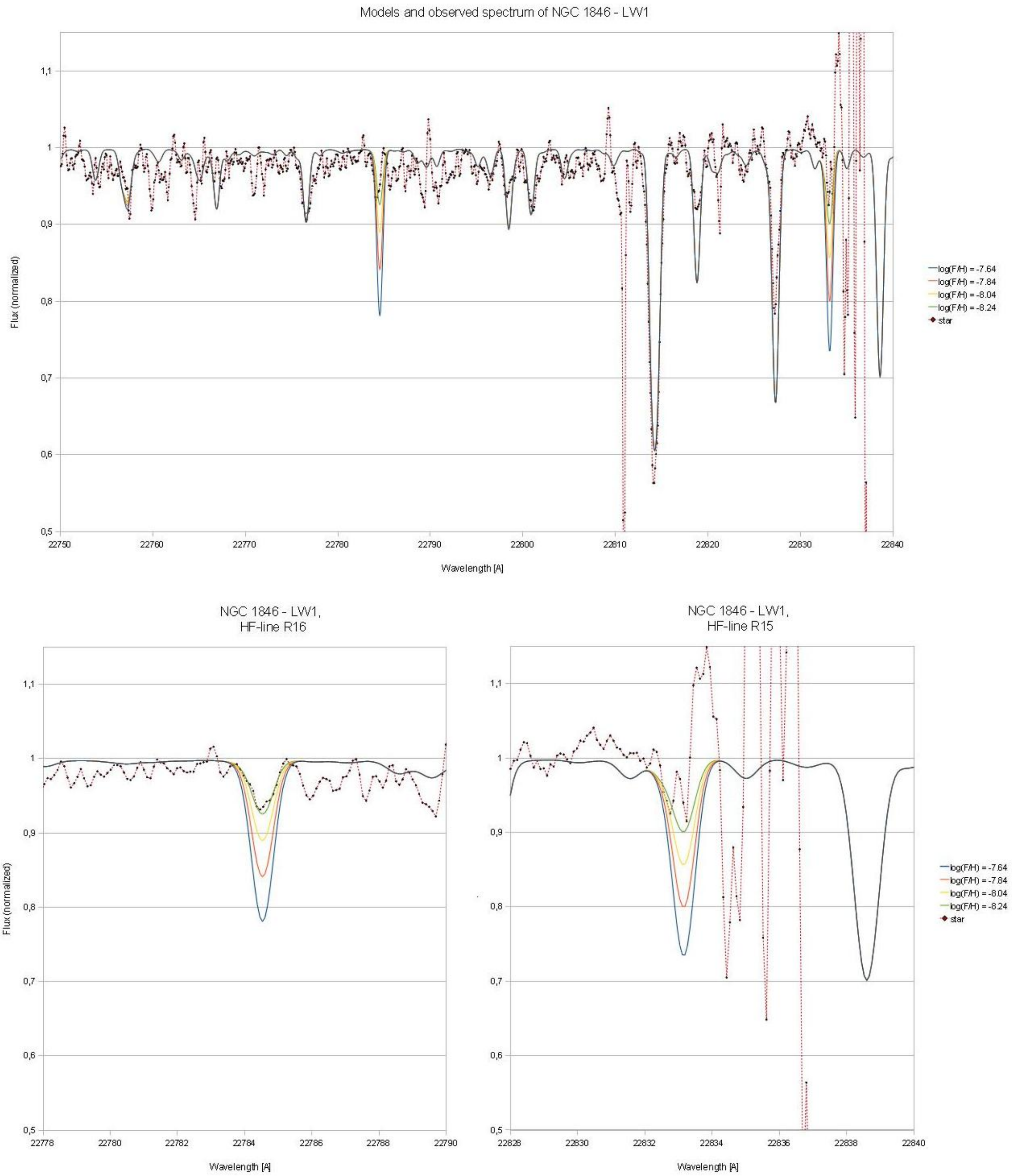

Figure 5.10: Same as Fig. 5.2 for NGC 1846 - LW1. The observed spectrum around the HF-feature R16 is matched well by the model with log(F/H) = -8.24, so this value was adopted. R15 was not taken into account.

5.1.2 H-band spectra of NGC 1846

In the synthetic H-band spectra, both the correlations and anti-correlations in line depth with growing C/O-ratio are clearly visible. Within the observed wavelength range all target stars follow these relations very well, besides the occasional cosmic/artifact of course, so it is easy to deduce their C/O ratio. While this value was already known for the object LE-13 (Lebzelter et al., 2008), it could be confirmed by this newer observation. It also shows a sharp contrast to the other four observed targets, which show significantly lower C/O ratios and an overall more homogeneous behaviour. For all shown models, the following fitting parameters were used: T_{eff} = 3600K and log(g) = 0.25.

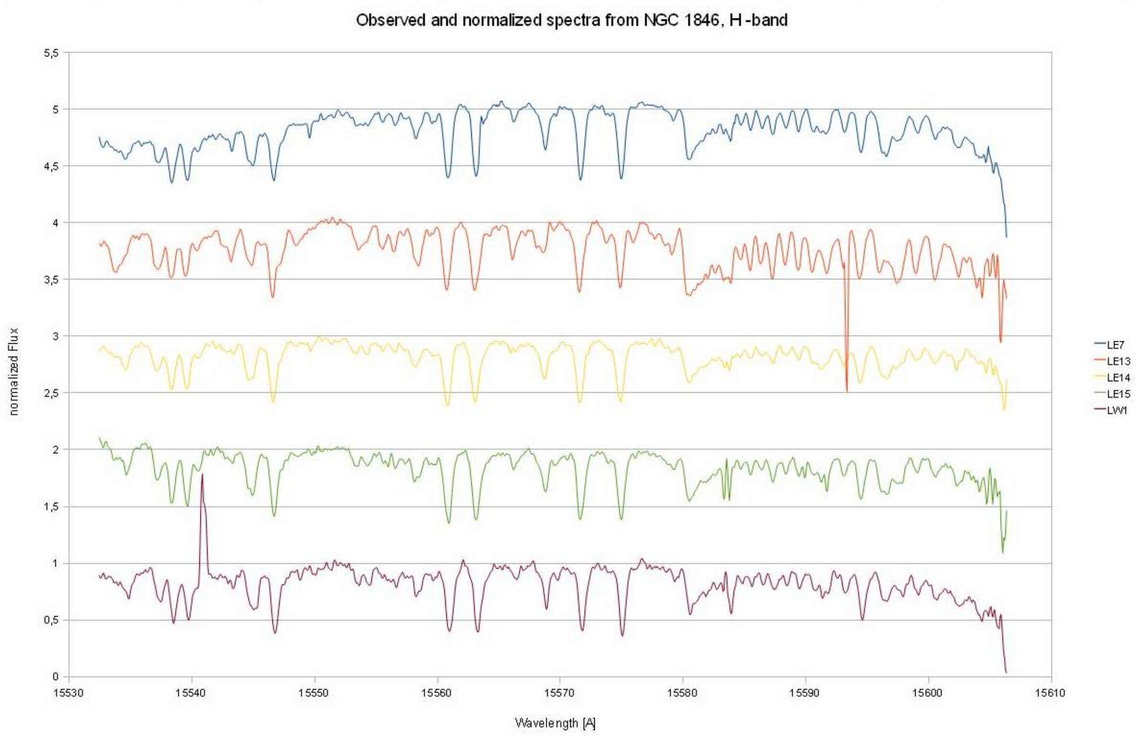

Figure 5.11: The observed, normalized H-band spectra of our targets in NGC 1846. No velocity correction has been applied, therefore a slight wavelength shift between them is visible. To separate individual stars, an artificial offset of 1.0 between the spectra has been added.

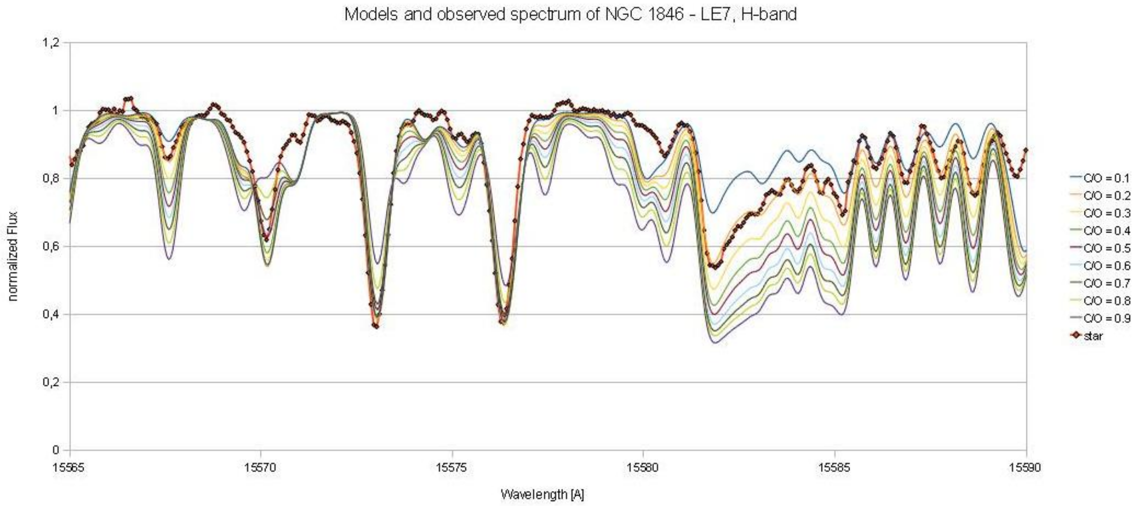

Figure 5.12: Detailed comparison of observed and synthetic H-band spectra for NGC 1846 - LE7. The model with C/O = 0.2 fits the observation best.

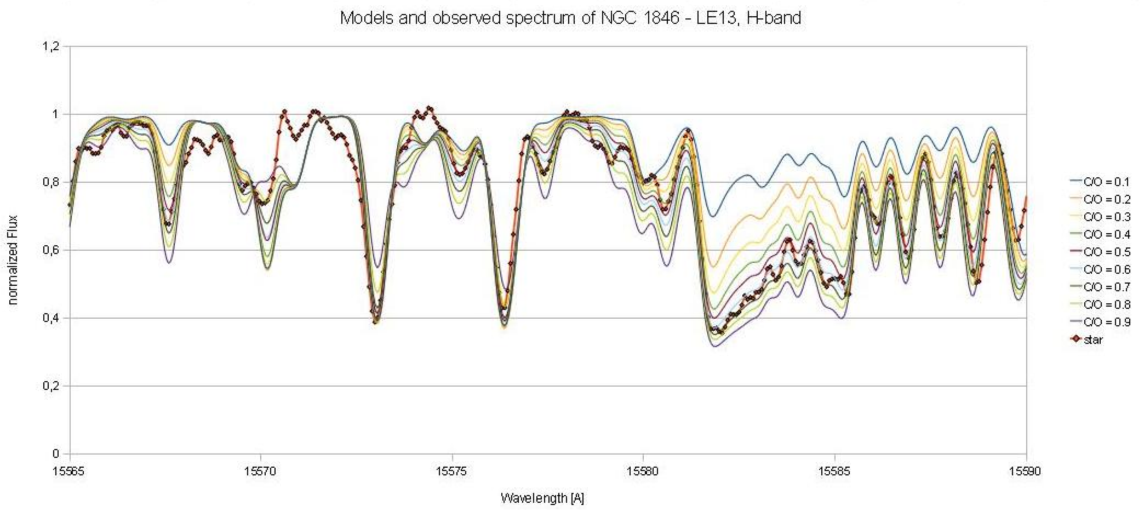

Figure 5.13: Same as Fig. 5.12 for NGC 1846 - LE13. The observed spectrum lies between the models with C/O = 0.6 and C/O = 0.7, so an adopted value of C/O = 0.65 was derived.

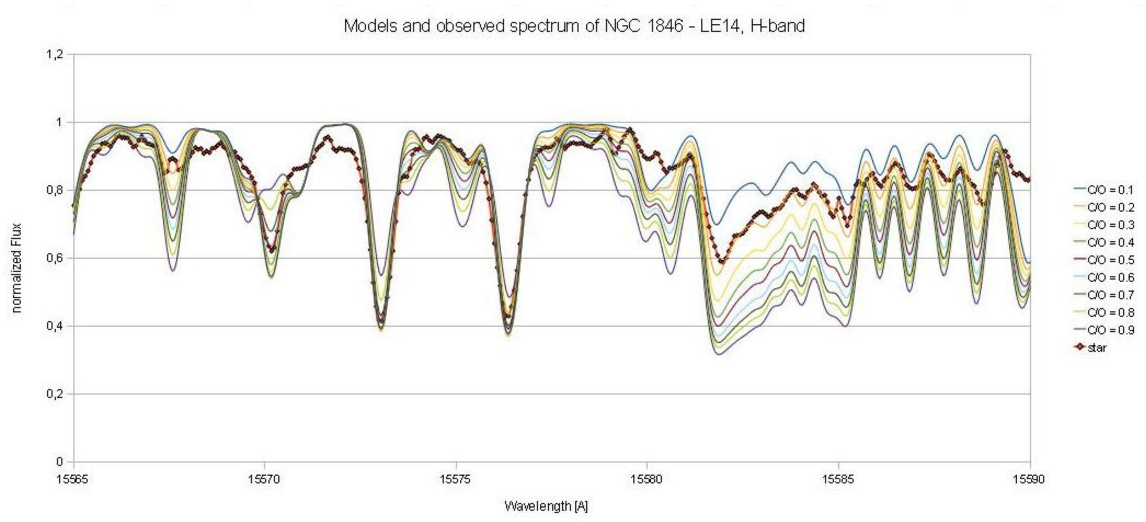

Figure 5.14: Same as Fig. 5.12 for NGC 1846 - LE14. The model with C/O = 0.2 fits the observation best.

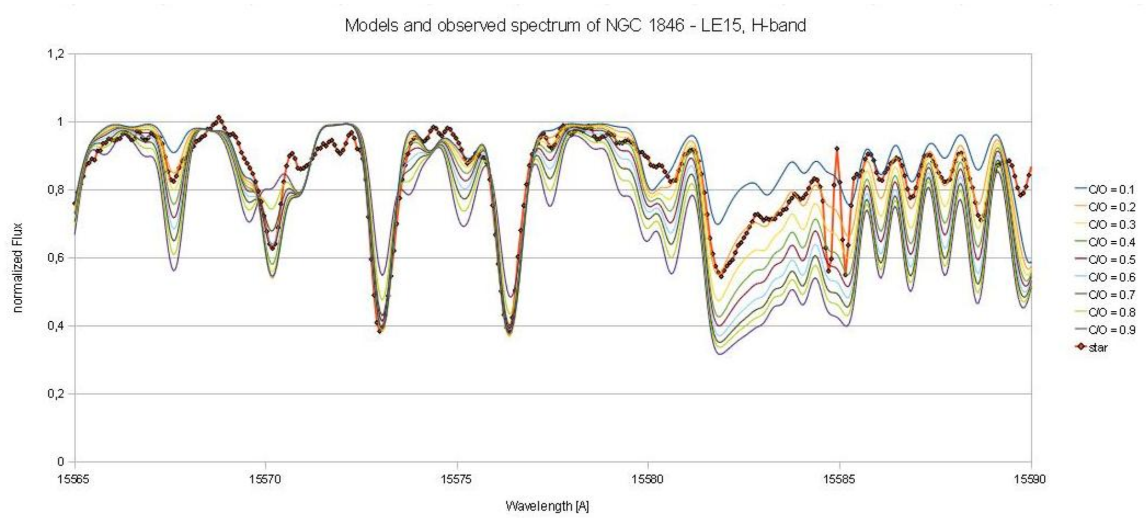

Figure 5.15: Same as Fig. 5.12 for NGC 1846 - LE15. The model with C/O = 0.2 fits the observation best. Please note, that the 'spike' (15585 Å) is most likely caused by a cosmic.

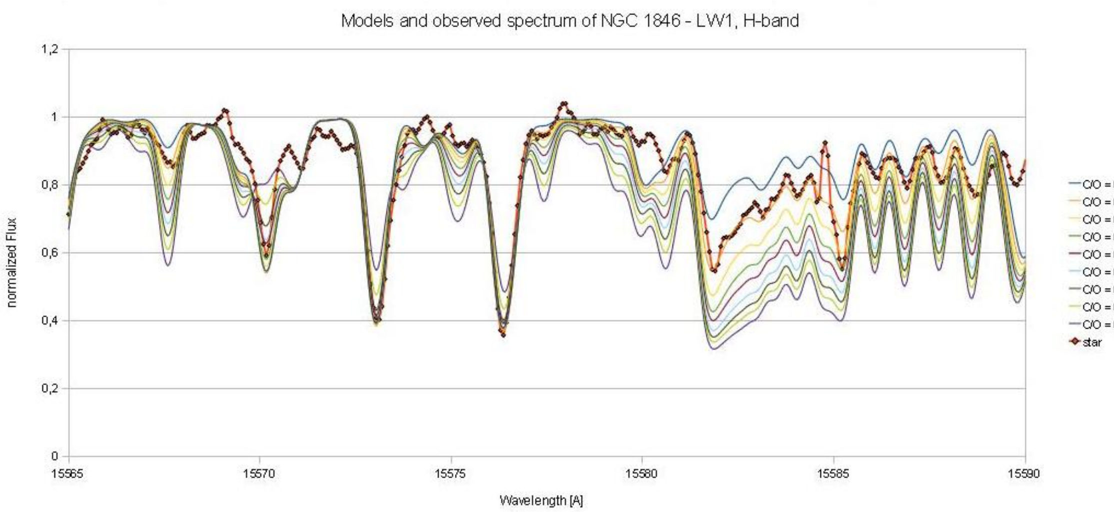

Figure 5.16: Same as Fig. 5.12 for NGC 1846 - LW1. The model with C/O = 0.2 fits the observation best.

5.1.3 K-band spectra of NGC 1978

The spectra of this cluster were provided already in this form and just had to be reproduced by modelling synthetic spectra with varying fluorine abundances. Here, in contrast to the spectra of NGC 1846, the observed HF-line is blended with a strong ^{13}CO-feature, making it a bit more tricky to derive the fluorine abundance, since although one is tempted to look for the model which fits the overall pattern the best, only the depth at a specific spectral point is important. Of course, however, the depth at this point depends as much on the C/O and ^{13}C/^{12}C ratios as on the F abundance. Although both values are well know for all our targets, this adds to the values' uncertainty, since the fitting of the model spectra is restricted by the available grid of COMARCS models they are based on. Here, the step size of the C/O ratio in the grid is 0.05 and the value for ^{13}C/^{12}C is kept constant. There is a workaround, however, as described in section 4.5. Therefore, since the C/O ratio offset is small and the ^{13}C/^{12}C ratio can be varied freely, the impact of the restricted input model grid and the additional fitting parameters should not be too significant, but have to be taken into account in the error estimation.

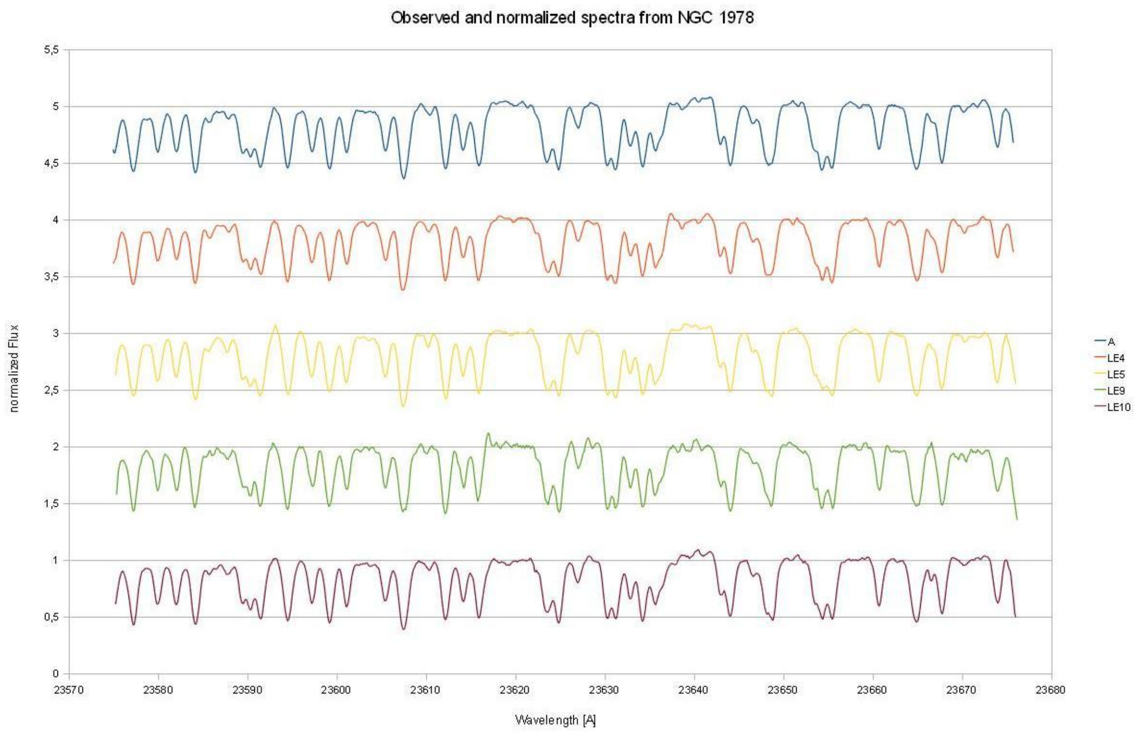

Figure 5.17: The observed, normalized K-band spectra of our targets in NGC 1978. They are plotted at zero velocity, therefore here no wavelength shift is visible. To separate individual stars, an artificial offset of 1.0 between their spectra has been added.

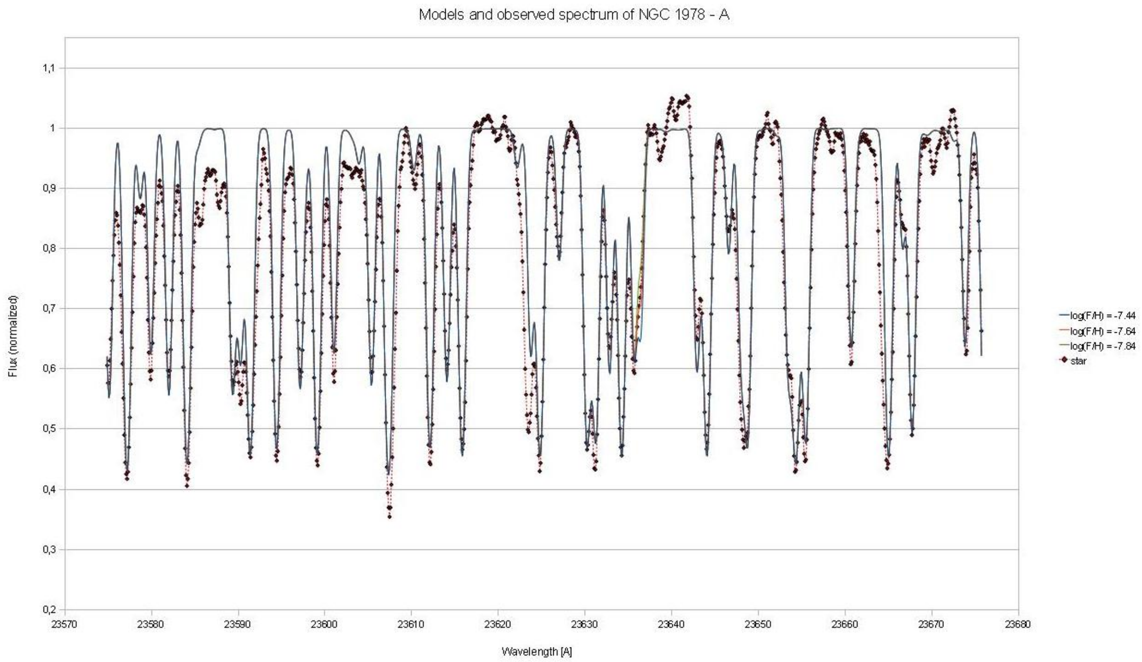

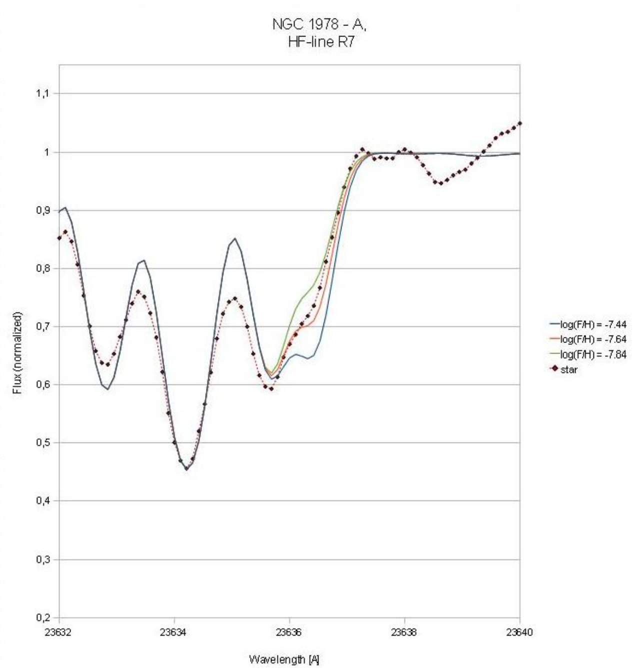

Figure 5.18: Comparison of observed and synthetic spectra for NGC 1978 - A, showing first the whole observed wavelength range and then a zoom on the blended HF-line. Since the depth of the observed spectral line lies between the two calculated models with log(F/H) = -7.64 and -7.84, a value of log(F/H) = -7.74 was adopted.

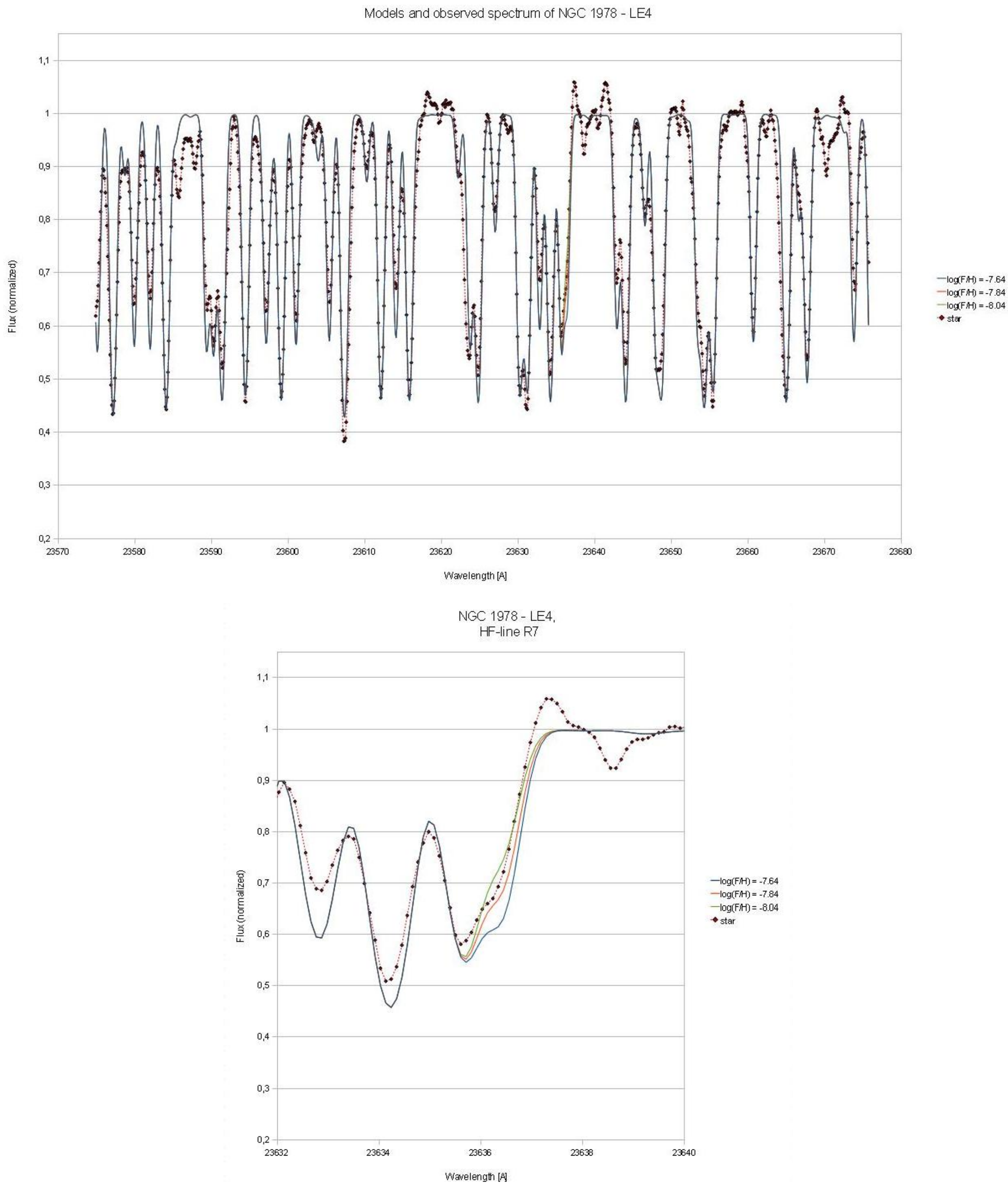

Figure 5.19: Same as Fig. 5.18 for NGC 1978 - LE4. Since the depth of the observed spectral line lies between the two calculated models with log(F/H) = -7.84 and -8.04, a value of log(F/H) = -7.94 was adopted.

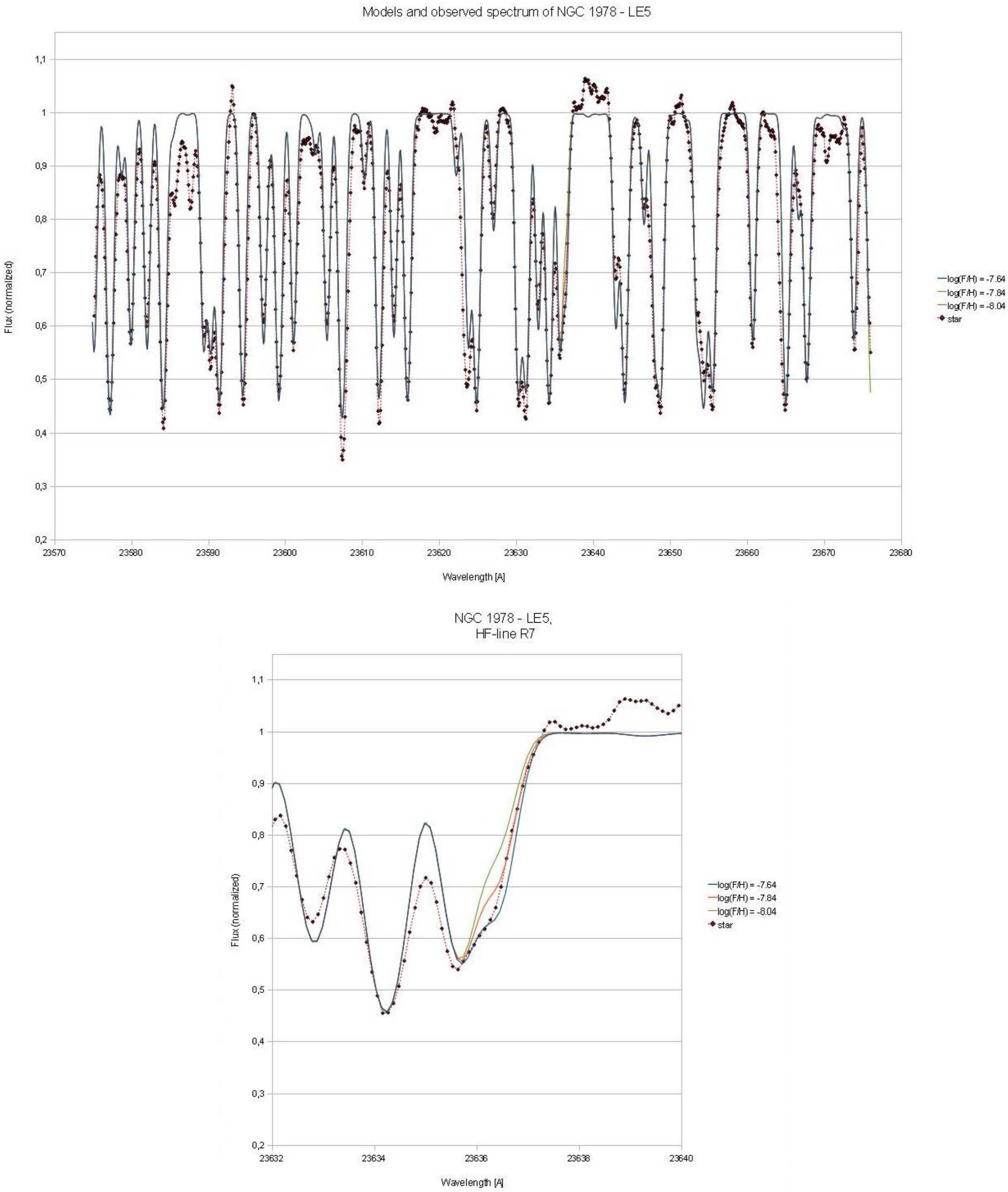

Figure 5.20: Same as Fig. 5.18 for NGC 1978 - LE5. The observed spectrum is matched well by the model with log(F/H) = -7.64, so this value was adopted.

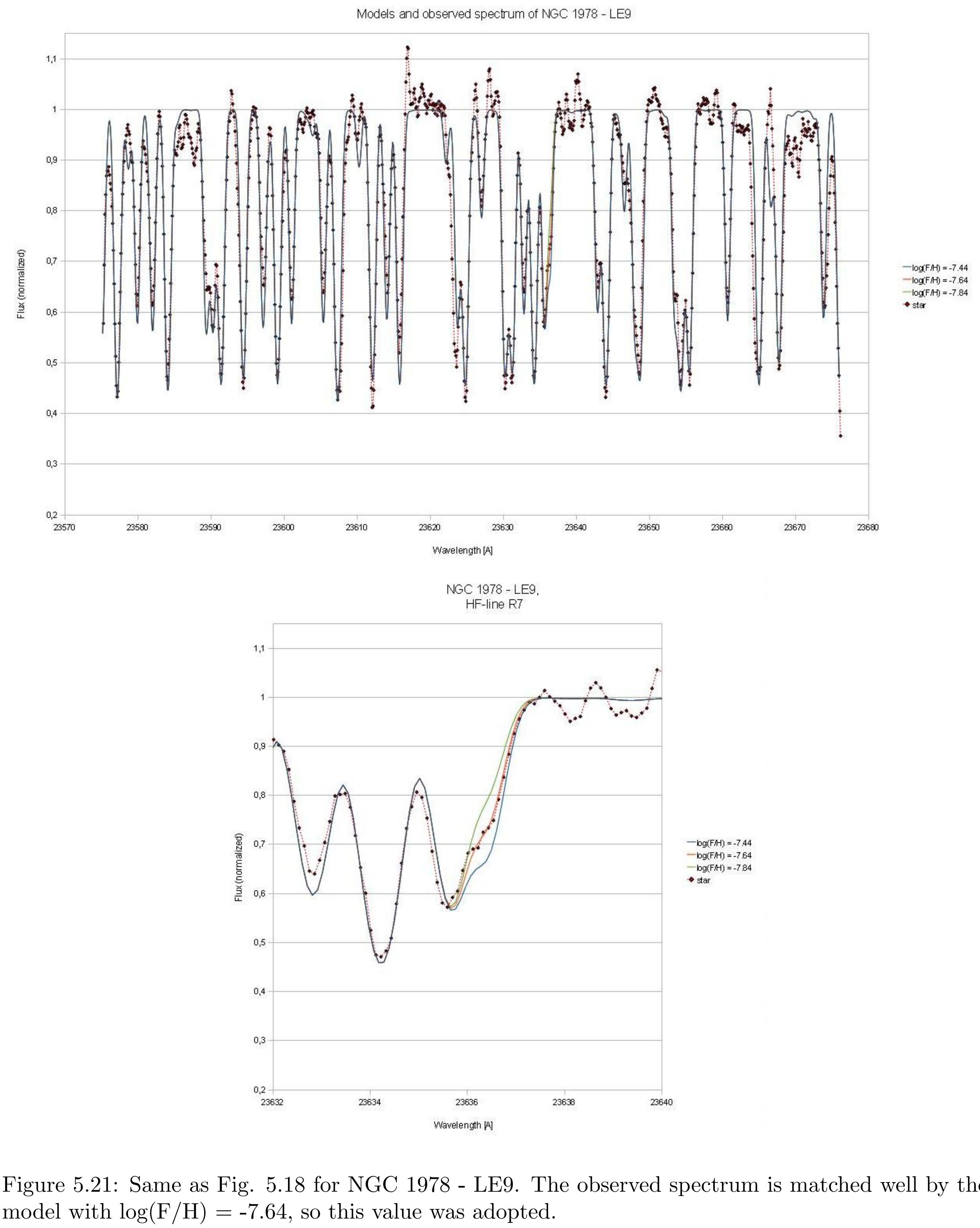

Figure 5.21: Same as Fig. 5.18 for NGC 1978 - LE9. The observed spectrum is matched well by the model with log(F/H) = -7.64, so this value was adopted.

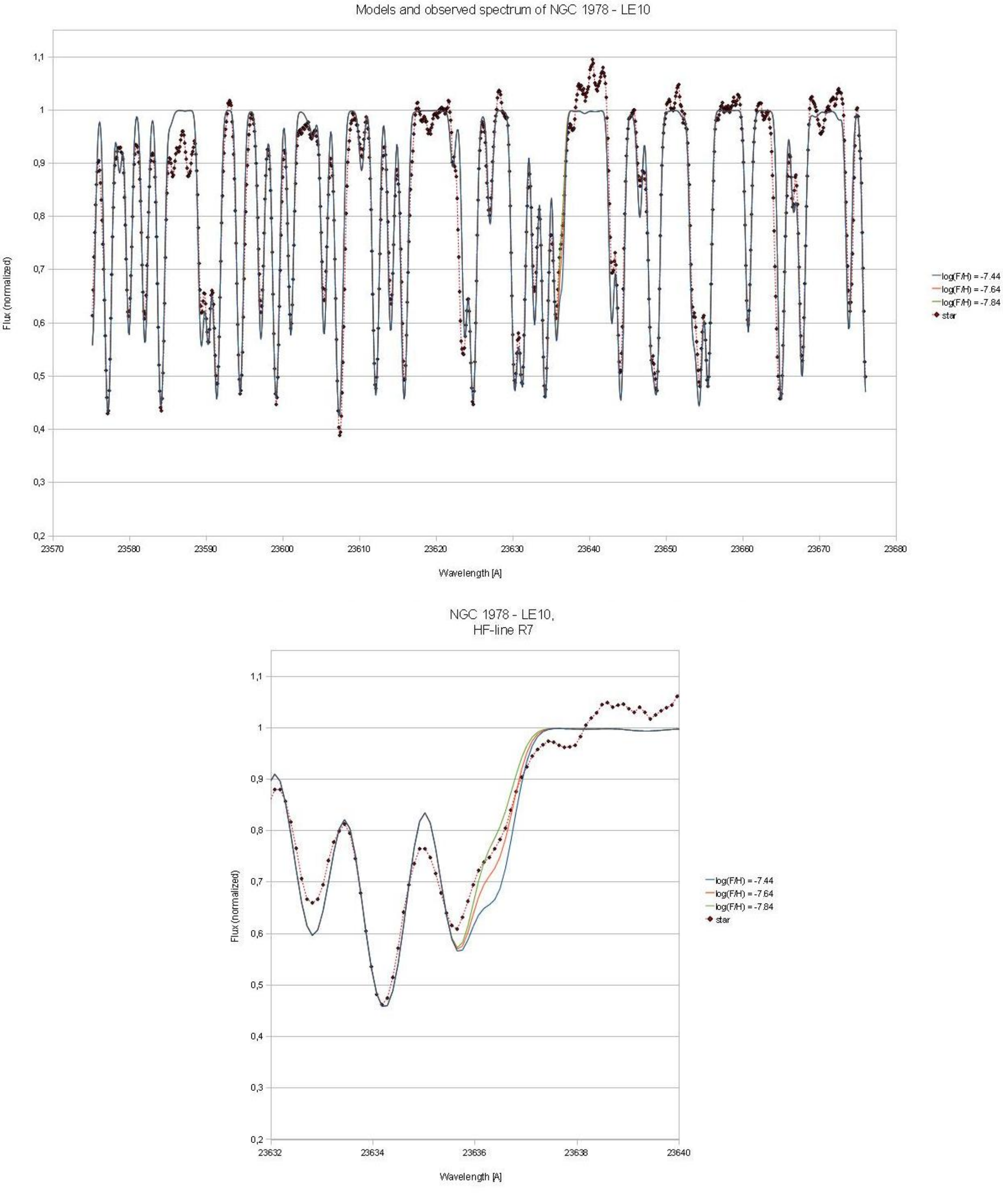

Figure 5.22: Same as Fig. 5.18 for NGC 1978 - LE10. Since the depth of the observed spectral line lies between the two calculated models with log(F/H) = -7.64 and -7.84, a value of log(F/H) = -7.74 was adopted.

5.2 Estimating errors

For the synthetic spectra of NGC 1846, the biggest error-source is the effective temperature (Fig. 4.1), a variation of 50K leading to an offset of almost 0.1 in the deduced fluorine abundance. Unfortunately, besides the observed HF-lines, the influence of temperature in the K-band spectrum is relatively small, so 'temperature fine tuning' by comparing synthetic with observed spectra proves to be rather difficult in this wavelength range.

The C/O ratio (Fig. 4.3), on the other hand, has generally a strong impact on the shape of the synthetic spectrum, its influence on the depth of the HF-lines is rather modest, however. Therefore, as long as the C/O ratio is small (<0.4), its variations are negligible and also above this threshold, a variation of +0.4 would be necessary to lead to a significant error of 0.1 in log(F/H).

In contrast to that, the appearance of the model spectrum does not change a lot by varying the surface gravity (Fig. 4.2), but it does have an influence on the strength of the two HF-features. As a consequence, a variation of 0.25 in its value can lead to an error of roughly 0.05 in the deduced fluorine abundance. An interesting detail in this case is, however, that the features are weakest at log(g) = 0.00, strongest at a value of log(g) = 0.25 and get weaker again at higher values.

Furthermore, the macroturbulent velocity (Fig. 4.4) is a significant factor at the estimation of the fluorine abundance, since a variation of 2km/s leads to an error of about 0.05 in log(F/H). Luckily, it does not influence only the depth but also the shape (width) of the features, so its value can be estimated well by some fine-tuning. Therefore, an error of 2km/s should be the maximum of what could go unnoticed.

In the worst case scenario, the influences of the fitting parameters add up to an error of about 0.2 in log(F/H). Of course, this should not be the case for most targets, since the parameters are usually known better than above mentioned and different errors can cancel each other out. A realistic error for most objects, especially the ones already observed by Lebzelter et al. (2008) is $\Delta log(F/H) = \pm$ 0.1. For the four objects where the fitting parameters were derived as described in section 4.4.2, the error is higher of course, since especially their log(g) and v_t values are questionable. However, for three of these objects their synthetic spectra fit that well to the observed ones, often better than in the other part of the sample, that it is hard to believe that the fitting parameters used could show larger errors. Therefore, also here an error of $\Delta log(F/H) = \pm$ 0.1 seems reasonable, with the single exception of LE7, where the fit is worse and the uncertainties are higher. A special case is the object LE9 (Fig. 5.5), where it was not possible to derive any reliable numbers for the fluorine abundance besides its upper limit. A higher abundance than log(F/H) = -8.34 seems to be very unlikely, since some kind of clear HF-feature should be visible in this case. It is not possible to set a lower limit of the F-abundance for this star, of course.

For the model spectra of NGC 1978 all these influences need to be taken into account as well. Additionally, since we are dealing here with a blended feature, here the uncertainty/error of the carbon isotopic ratio is an issue as it was explained in the previous section. At lower ratios, an offset of $\Delta\ ^{12}C/^{13}C = 5$ can lead to an error in log(F/H) of up to 0.05. This effect gets smaller with increasing carbon isotopic ratio, and above a value of about $^{12}C/^{13}C = 20$ the influence of this parameter on the HF-feature depth at our typically observed fluorine abundances becomes rather negligible (as shown in Fig. 4.5). The target stars in NGC 1978, however, all show values below this threshold and therefore we have to accept a higher formal error of 0.15 in log(F/H) for the five objects in this cluster.

Chapter 6

Results

This section will present and discuss the results of this work, compare it with the results of other publications and try to evaluate their consequences for the understanding of fluorine production in AGB stars.

6.1 Measured values

The results of this thesis are presented in the tables on the following page (Tab. 6.1 and 6.2). One can notice a few significant differences between the targets in both clusters. The targets in NGC 1846 show a correlation between their observed C/O ratio and their fluorine abundance, although this trend is clearly visible only due to the two members LE 13 and LE 16. Although LE 8 also shows an enhanced abundance, that alone could also be explained by a combination of observational errors and uncertain fitting parameters.
In contrast to this, nothing similar is observed in the results from NGC 1978. This is not really surprising, however, since the sample is rather uniform in C/O ratios and also the paper by Lederer et al. (2009) states that the authors did not detect any M-stars with an ongoing 3rd dredge-up in this cluster, which would be necessary to raise the C/O ratio and the fluorine abundance. There is one interesting thing about the targets in this cluster however. On average, all NGC 1978-targets show significantly higher fluorine abundances at similar C/O ratio than the targets in the other cluster.

Furthermore, there is also a comparison between the measurements for this thesis and the ones published by Lebzelter et al. (2008) presented in table 6.3 and in figure 6.1. The reader will notice rather significant offsets of ≈ 0.2 dex between the two sets of observations. While this is as much as the error bars on both measurements combined, this alone can hardly account for it. The offset might be explained by a systematic error as a consequence of using a different wavelength range with a blended HF-feature, leading to an overestimation of log(F/H) when the blended feature is used. This might be an issue for the measurements of the targets in NGC 1978 as well, since here the same feature is used and therefore, the observed abundances might need to be adjusted. This remains speculative though, until new observations in another wavelength range can confirm or reject the numbers presented in this work. The systematic offset does not affect the steep increase of [F/Fe] with rising C/O ratio, described by Lebzelter et al. (2008), however, since the same relation is observed also in this work.

Table 6.1: Results for the targets in NGC 1846 (LE stands for Lloyd Evans 1980). Data partially from: Lebzelter et al. (2008). The presented [F/Fe] values are based on a mean cluster metallicity of [Fe/H] = -0.4, please note the offset to the value published by Grocholski et al. (2006) of [Fe/H] = -0.49.

ID	$T_{eff,f}$ [K]	$log(g)$	v_t [km/s]	C/O	$^{12}C/^{13}C$	$log(F/H)$	$[F/Fe]$
H39	3650	0.25	3	0.20 ± 0.05	12 ± 2	-8.14 ± 0.1	-0.67 ± 0.1
LE8	3550	0.25	3	0.30 ± 0.05	20 ± 2	-8.04 ± 0.1	-0.57 ± 0.1
LE9	3650	0.25	3	0.20 ± 0.05	13 ± 2	< -8.34	< -0.87
LE13	3600	0.00	7	0.65 ± 0.10	60 ± 5	-7.24 ± 0.1	+0.23 ± 0.1
LE16	3600	0.00	4	0.44 ± 0.05	43 ± 2	-7.84 ± 0.1	-0.37 ± 0.1
LE7	3600 ± 50	0.25 ± 0.25	3 ± 2	0.20 ± 0.05	6	-8.14 ± 0.1	-0.67 ± 0.15
LE14	3625 ± 50	0.25 ± 0.25	3 ± 2	0.20 ± 0.05	6	-8.24 ± 0.1	-0.77 ± 0.1
LE15	3600 ± 50	0.25 ± 0.25	3 ± 2	0.20 ± 0.05	6	-8.24 ± 0.1	-0.77 ± 0.1
LW1	3625 ± 50	0.25 ± 0.25	3 ± 2	0.20 ± 0.05	6	-8.24 ± 0.1	-0.77 ± 0.1

Table 6.2: Results for the targets in NGC 1978 (LE stands for Lloyd Evans 1980). Data partially from: Lederer et al. (2009). The presented [F/Fe] values are based on a mean cluster metallicity of [Fe/H] = -0.4, please note the offset to the value published by Mucciarelli et al. (2007) of [Fe/H] = -0.37.

ID	$T_{eff,f}$ [K]	$log(g)$	v_t [km/s]	C/O	$^{12}C/^{13}C$	$log(F/H)$	$[F/Fe]$
A	3825	0.50	3	0.23 ± 0.05	16 ± 3	-7.74 ± 0.15	-0.27 ± 0.15
LE4	3725	0.38	3	0.18 ± 0.03	13 ± 4	-7.94 ± 0.15	-0.47 ± 0.15
LE5	3775	0.25	3	0.18 ± 0.05	6 ± 2	-7.64 ± 0.15	-0.17 ± 0.15
LE9	3900	0.38	3	0.13 ± 0.03	12 ± 2	-7.64 ± 0.15	-0.17 ± 0.15
LE10	3900	0.38	3	0.18 ± 0.05	9 ± 3	-7.74 ± 0.15	-0.27 ± 0.15

6.2 Discussion

As it was discovered and published by Jorissen, Smith, & Lambert (1992), fluorine can be produced in AGB-stars. A possible correlation between its abundance and the observed C/O ratio and, thus, the third dredge up efficiency, was investigated by a number of authors, for example by Zhang & Liu (2005) for planetary nebulae and by Lebzelter et al. (2008) for red giants in the LMC.
The data presented here support their observations concerning the synthesis and dredge up of fluorine during the AGB-phase and the correlation between [F/Fe] and C/O is clearly visible in figure 6.1.

In the work by Lebzelter et al. (2008) the authors try to explain the observed relation between [F/Fe] and C/O with the model described by Forestini et al. (1992) and Mowlavi et al. (1996) (section 1.3.2). They come to the conclusion, that theoretical

Table 6.3: Results for the targets in NGC 1846 (LE stands for Lloyd Evans 1980) which were also observed by Lebzelter et al. (2008) already, in order to compare the results of both works and to detect eventual systematic offsets, due to the different wavelength areas and HF-features used. While the $[F/Fe]_{(2008)}$-values were presented in the paper mentioned above, the $[F/Fe]_{new}$-values were derived in this work. There is a significant offset of roughly 0.2 dex visible for most targets.

ID	$T_{eff,f}$ [K]	$log(g)$	v_t [km/s]	C/O	$^{12}C/^{13}C$	$[F/Fe]_{(2008)}$	$[F/Fe]_{new}$
H39	3650	0.25	3	0.20 ± 0.05	12 ± 2	-0.71 ± 0.1	-0.67 ± 0.1
LE8	3550	0.25	3	0.30 ± 0.05	20 ± 2	-0.35 ± 0.1	-0.57 ± 0.1
LE9	3650	0.25	3	0.20 ± 0.05	13 ± 2	-0.42 ± 0.1	< -0.87
LE13	3600	0.00	7	0.65 ± 0.10	60 ± 5	+0.40 ± 0.1	+0.23 ± 0.1
LE16	3600	0.00	4	0.44 ± 0.05	43 ± 2	-0.20 ± 0.1	-0.37 ± 0.1

predictions do not manage to explain their observations, however. Although models predict the production of a substantial amount of fluorine, they can not fully account for the observed abundances, as was claimed previously by Jorissen, Smith, & Lambert (1992). As a possible solution they suggest, without going into details, a more efficient production of ^{15}N in the inter-shell region.

The recent publication by Kamath et al. (2012) tries to solve this problem by including an artificial partial mixing zone at the deepest extend of each third dredge up. They experiment with different proton values and depths of these artificial partial mixing zones to match the observations by Lebzelter et al. (2008) better. Their best fitting model can reproduce the observations, but requires very deep mixing zones (M_{PLZ} = 1.2x10^{-2}M$_{\odot}$). This does not fit to theoretical models for s-process elements, which require smaller partial mixing zones (Kamath et al. (2012) and references therein). The authors conclude, therefore, that this is a speculative result. Fluorine production in AGB-stars remains to be an open question.

6.3 Conclusions

In this work, H- and K-band spectra were used to deduce the fluorine abundances of stars in the two LMC clusters NGC 1846 and NGC 1978. The results suggest a higher fluorine production in AGB-stars than predicted by the 'standard model'. It is beyond the scope of this thesis, to find better fitting nucleosynthesis or mixing models to explain the new observations. It can be stated, however, that the values published by Lebzelter et al. (2008) can not be explained solely by their use of a blended feature, since the steep increase in [F/Fe] with rising C/O is detected by observing the unblended features R15 and R16 as well. There is a systematic offset of ≈ 0.2 dex between their and my values, however. This offset is most likely a consequence of using different features and affects presumably also my data from NGC 1978, where the same blended feature R7 is used for the abundance measurements. In order to check this claim, further observations of the objects in NGC 1978 in the wavelength range of the features R15 and R16 would be necessary.

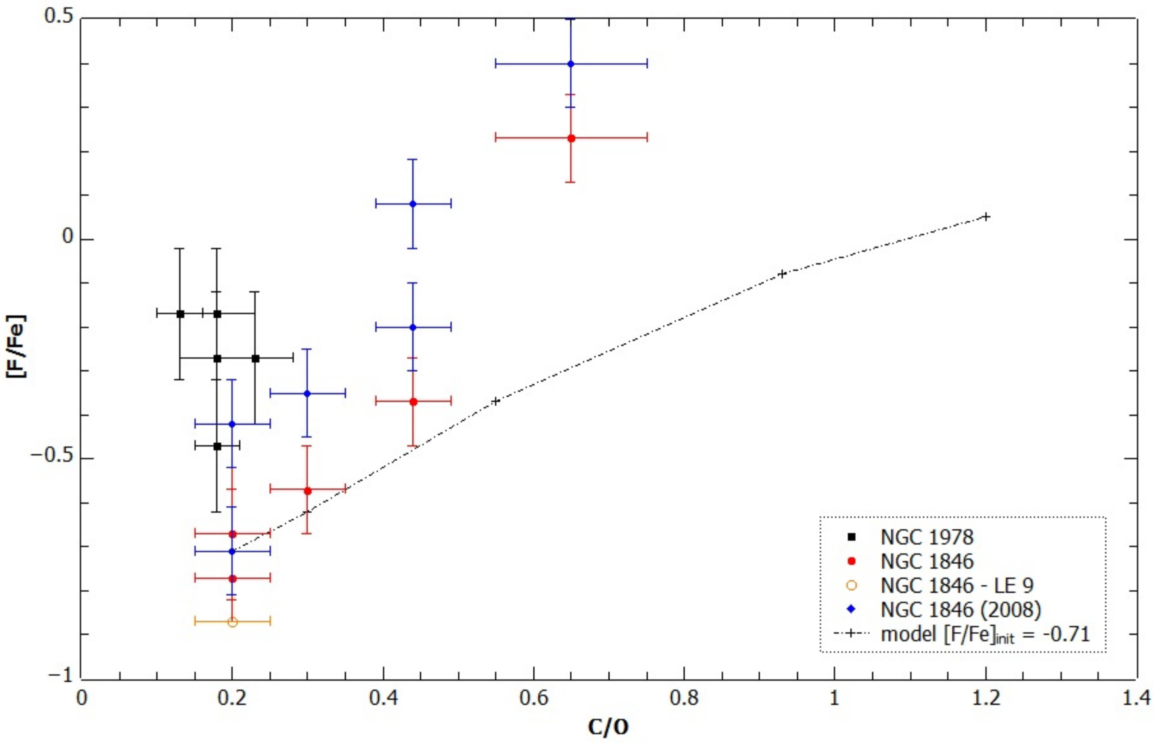

Figure 6.1: The measured fluorine abundances as a function of the C/O ratio. The majority of the C/O data was taken from Lebzelter et al. (2008) and Lederer et al. (2009). Please note that some of the data point overlap and, therefore, are not visible individually. The black squares mark the measurements of NGC 1978, the red and orange circles the ones from NGC 1846. The blue diamonds represent the measurements by Lebzelter et al. (2008), showing the same inclination as the measurements form this work, but with some offset. The dashed line is taken from this paper as well, and shows a theoretical model with an initial [F/Fe] of -0.71. While it does fit to the observations at low C/O ratios, it fails to reproduce the inclination of the relation. (Diagram generated with QtiPlot (2012))

Danksagung

Ich möchte mich in erster Linie bei meinem Betreuer Thomas Lebzelter bedanken, der mir die ursprüngliche Idee geliefert und die Beobachtungsdaten zur Verfügung gestellt hat und auch darüber hinaus stets mit Rat zur Stelle war.

Dank gilt auch meiner Frau Aleksandra, die meine Launen ertragen und sich mutig als Lektorin durch den Text gekämpft hat.

Bibliography

Alcaíno, G., Liller, W., Alvarado, F., Kravtsov, V., Ipatov, A., Samus, N., & Smirnov, O. 1999, Astronomy and Astrophysics, Supplement, 135, 103

Alpher, R. A., Bethe, H., & Gamow, G. 1948, Physical Review, 73-7, 803

Aringer, B. 2000, PhD thesis, Univ. of Vienna

Aringer, B., Girardi, L., Nowotny, W., Marigo, P., & Lederer, M. T. 2009, Astronomy and Astrophysics, 503, 913

Bethe, H. A. 1939, Physical Review, 55-5, 434

Burbidge, E. M., Burbidge, G. R., Fowler, W. A., & Hoyle, F. 1957, Reviews of Modern Physics, 29-4, 547

Cameron, A. G. W., & Fowler, W. A. 1971, Astrophysical Journal, 164, 111

Croswell, K. 2003, Fluorine: An Element-ary Mystery, http://kencroswell.com/fluorine.html

Falkesgaard, J. F. 2001, Master's thesis, Univ. Copenhagen

Ferraro, F. R., Mucciarelli, A., Carretta, E., & Origlia, L. 2006, Astrophysical Journal, Letters, 645, L33

Fischer, P., Welch, D. L., & Mateo, M. 1992, The Astronomical Journal, 104, 1086

Forestini, M., Goriely, S., Jorissen, A., & Arnould, M. 1992, Astronomy and Astrophysics, 261, 157

Frogel, J. A., Mould, J., & Blanco, V. M. 1990, The Astrophysical Journal, 352, 96

Geballe, T., Mason, R., Volk, K., & Hayward, T. 2006, Introduction to Ground-based Mid-IR Observing, http://www.gemini.edu/?q=node/10138

Gemini Observatory. 2012, About The Gemini Observatory, http://www.gemini.edu/about

Gorfer, M. 2005, Master's thesis, Univ. of Vienna

Grocholski, A. J., Cole, A. A., Sarajedini, A., Geisler, D., & Smith, V. V. 2006, The Astronomical Journal, 132, 1630

Gustafsson, B., Bell, R. A., Eriksson, K., & Nordlund, Å. 1975, Astronomy and Astrophysics, 42, 407

Gustafsson, B., Edvardsson, B., Eriksson, K., Jørgensen, U. G., Nordlund, Å., & Plez, B. 2008, Astronomy and Astrophysics, 486, 951

Habing, J. H., & Olofsson, H. 2004, Asymptotic giant branch stars (New York: Springer)

Hill, V., François, P., Spite, M., Primas, F., & Spite, F. 2000, Astronomy and Astrophysics, 364, L19

Hinkle, K., Wallace, L., & Livingston, W. 1995, Infrared Atlas of the Arcturus Spectrum, 0.9-5.3μm (San Francisco: Astronomical Society of the Pacific)

Hinkle, K. H., Blum, R. D., Joyce, R. R., Sharp, N., Ridgway, S. T., Bouchet, P., van der Bliek, N. S., Najita, J., & Winge, C. 2003, in Society of Photo-Optical Instrumentation Engineers (SPIE) Conference Series, Vol. 4834, Society of Photo-Optical Instrumentation Engineers (SPIE) Conference Series, ed. P. Guhathakurta, 353–363

Höfner, S. 2011, in Astronomical Society of the Pacific Conference Series, Vol. 445, Why Galaxies Care about AGB Stars II: Shining Examples and Common Inhabitants, ed. F. Kerschbaum, T. Lebzelter, & R. F. Wing, 193

Höfner, S., & Andersen, A. C. 2007, Astronomy and Astrophysics, 328, L39

Jørgensen, U. G., Johnson, H. R., & Nordlund, Å. 1992, Astronomy and Astrophysics, 261, 263

Jorissen, A., Smith, V. V., & Lambert, D. L. 1992, Astronomy and Astrophysics, 261, 164

Kamath, D., Karakas, A. I., & Wood, P. R. 2012, Astrophysical Journal, 746, 20

Karakas, A. I., Campbell, S. W., & Stancliffe, R. J. 2010, Astrophysical Journal, 713, 374

Kupka, F. G., Ryabchikova, T. A., Piskunov, N. E., Stempels, H. C., & Weiss, W. W. 2000, Baltic Astronomy, 9, 590

LaTeX. 2012, A document preparation system, http://www.latex-project.org/

Lebzelter, T., & Hron, J. 2003, Astronomy and Astrophysics, 411, 533

Lebzelter, T., Lederer, M. T., Cristallo, S., Hinkle, K. H., Straniero, O., & Aringer, B. 2008, Astronomy and Astrophysics, 486, 511

Lebzelter, T., & Wood, P. R. 2007, Astronomy and Astrophysics, 475, 643

Lederer, M. T., Lebzelter, T., Cristallo, S., Straniero, O., Hinkle, K. H., & Aringer, B. 2009, Astronomy and Astrophysics, 502, 913

Leonardi, A. J., & Rose, J. A. 2003, The Astronomical Journal, 126, 1811

Lloyd Evans, T. 1980, MNRAS, 193, 87

Mackey, A. D., & Broby Nielsen, P. 2007, MNRAS, 379, 151

Merrill, P. W. 1952, Astrophysical Journal, 116, 21

Meynet, G., & Arnould, M. 2000, Astronomy and Astrophysics, 355, 176

Mowlavi, N., Jorissen, A., & Arnould, M. 1996, Astronomy and Astrophysics, 311, 803

Mucciarelli, A., Ferraro, F. R., Origlia, L., & Fusi Pecci, F. 2007, Astrophysical Journal, 133, 2053

Neufeld, D. A., Zmuidzinas, J., Schilke, P., & Phillips, T. G. 1997, Astrophysical Journal, Letters, 488, L141

Nowotny, W., Aringer, B., Höfner, S., Hron, J., & Kerschbaum, F. 2007, Astronomische Nachrichten, 328, 650

Olszewski, E. W., Suntzeff, N. B., & Mateo, M. 1996, Annual Review of Astron and Astrophys, 34, 511

OpenOffice. 2012, The Free and Open Productivity Suite, http://www.openoffice.org/

Pagel, B. E. J. 1997, Nucleosynthesis and Chemical Evolution of Galaxies (Cambridge: Cambridge University Press)

Pandey, G. 2006, Astrophysical Journal, Letters, 648, 143

QtiPlot. 2012, Data Analysis and Scientific Visualisation, http://soft.proindependent.com/qtiplot.html

Renda, A., Fenner, Y., Gibson, B. K., Karakas, A. I., Lattanzio, J. C., Campbell, S., Chieffi, A., Cunha, K., & Smith, V. V. 2004, MNRAS, 354, 575

Salaris, M., & Cassissi, S. 2005, Evolution of stars and stellar populations (The Atrium, Southern Gate, Chichester, West Sussex, England: Wiley & Sons)

Skrutskie, M. F., Cutri, R. M., Stiening, R., Weinberg, M. D., Schneider, S., Carpenter, J. M., Beichman, C., Capps, R., Chester, T., Elias, J., Huchra, J., Liebert, J., Lonsdale, C., Monet, D. G., Price, S., Seitzer, P., Jarrett, T., Kirkpatrick, J. D., Gizis, J. E., Howard, E., Evans, T., Fowler, J., Fullmer, L., Hurt, R., Light, R., Kopan, E. L., Marsh, K. A., McCallon, H. L., Tam, R., Van Dyk, S., & Wheelock, S. 2006, Astrophysical Journal, 131, 1163

Snow, T. P. J., & York, D. G. 1981, Astrophysical Journal, Letters, 247, L39

Spinrad, H., Kaplan, L. D., Connes, P., Connes, J., Kunde, V. G., & Maillard, J. P. 1971, in Late-Type Stars, ed. W. G. Lockwood, & M. H. Dyck, Vol. 554, Kitt Peak National Observatory, 59

Tody, D. 1986, in Society of Photo-Optical Instrumentation Engineers (SPIE) Conference Series, Vol. 627, Society of Photo-Optical Instrumentation Engineers (SPIE) Conference Series, ed. D. L. Crawford, 733

Uttenthaler, S., Aringer, B., Lebzelter, T., Käufl, H. U., Siebenmorgen, R., & Smette, A. 2008, Astrophysical Journal, 682, 509 van den Bergh, S. 2008, The Astronomical Journal, 135, 1731

Werner, K., Rauch, T., & Kruk, J. W. 2005, Astronomy and Astrophysics, 433, 641

Woosley, S. E., & Haxton, W. C. 1988, Nature, 334, 45

Zhang, Y., & Liu, X.-W. 2005, Astrophysical Journal, Letters, 631, L61

Appendix A

Abstract - English

The goal of this thesis is the measurement of the fluorine abundances in a sample of M-type red giant (AGB) target stars in the two clusters NGC 1846 and NGC 1978 in the Large Magellanic Cloud. The origin of this element remains uncertain, since a number of theories considering its synthesis exist and the efficiency of its production in different sites (supernovae, Wolf-Rayet and AGB-stars) is a matter of discussion. Previous work on this matter suggests, that the contribution of AGB-stars is underestimated by the standard theories and that a better understanding of the nucleosynthesis or the mixing might be necessary to explain the observed values. In order to verify this claim, the measured fluorine abundances of the targets are compared with their C/O ratio, which is a good indicator for an ongoing third dredge up in these stars and which should enhance both the carbon and the fluorine abundance on the stellar surface. While a positive correlation is to be expected, its inclination is the deciding factor, whether the nucleosynthesis- or mixing-models need to be adjusted.

To measure the fluorine abundance, a series of H- and K-band spectra were taken of our targets. The data used were provided by the Phoenix spectrograph at the Gemini South telescope. While the data from NGC 1978 were already used for another publication and, thus, were available fully reduced, the one of NGC 1846 were taken especially for this purpose and needed to go through all the necessary reduction steps, done by using the IRAF-package. After the data-reduction, a grid of synthetic spectra with varying fluorine abundances was created by using MARCS models and the COMA-code. By comparing these synthetic spectra with the observed ones, the fluorine abundances of the targets could be deduced with a good level of accuracy.

In the cluster NGC 1846, the measured fluorine abundances reach from an underabundance in the order of [F/Fe] = -0.77 in the majority of the targets in this cluster to an overabundance [F/Fe] = +0.23 in one cluster member (LE13). The objects with higher fluorine abundances also tend to have higher C/O ratios, so the third dredge up takes place in some cluster members. Furthermore, the increase is steeper as the one predicted by standard models, so the inclusion of some kind of extra mixing in the models might be necessary to match the observations.

In the cluster NGC 1978, the measured fluorine abundances are rather homogeneous, [F/Fe] $\approx$ -0.27, as are also their C/O ratios. This indicates, that the M-stars in this cluster have no ongoing third dredge up. The sample, however, is restricted to 5 cluster members only.

Three different hydrogen fluoride features were used for the measurements: R15 and R16 for the objects in NGC 1846 and R7 for the objects NGC 1978. While R15 and R16 are unblended, R7 is blended with a strong CO line and, thus, less reliable. When comparing the new observations of NGC 1846 with older ones, where this feature is used, it becomes apparent that there is a systematic offset of ≈ 0.2 dex between the two datasets. R7 suggests presumably higher abundances. This is something to take into account when using this feature for future abundance-measurements.

Appendix B

Abstract - Deutsch

Das Ziel dieser Arbeit ist die Bestimmung der Fluorhäufigkeit in einer Anzahl roter Riesen (am AGB) des Spektraltyps M in den beiden Kugelsternhaufen NGC 1846 und 1978 in der Großen Magellanschen Wolke. Der Ursprung dieses Elements ist unklar, da es zwar eine Reihe von Theorien zu seiner Synthese gibt, der Beitrag der einzelnen Quellen (Supernovae, Wolf-Rayet- und AGB-Sterne) aber umstritten ist. Bisherige Arbeiten zu diesem Thema deuten darauf hin, dass der Anteil, der von AGB-Sternen geleistet wird, in den Standardmodellen jedoch unterschätzt wird und wir eine bessere Vorstellung von der Fluorproduktion in diesen Objekten benötigen, um die Beobachtungen erklären zu können. Um diese Vermutung zu überprüfen, vergleicht der Autor die gemessenen Fluorhäufigkeiten mit dem C/O Verhältnis der beobachteten Sterne, da ein erhöhter Wert darauf hindeuten würde, dass in diesen Sternen der 'third dredge-up' stattfindet und wobei mit dem Kohlenstoff auch Fluor an die Oberfläche transportiert werden sollte. Eine positive Korrelation kann daher erwartet werden und ihr Anstieg ist der entscheidende Faktor, ob unsere Modelle verbessert werden müssen.

Um die Fluorhäufigkeiten zu bestimmen, wurden Serien von H- und K-Band Spektren von den Zielobjekten mit Hilfe des Phoenix Spektrographen am Gemini South Teleskop aufgenommen. Die Daten von NGC 1978 wurden bereits für eine Publikation verwendet und standen mir daher bereits vollständig reduziert zur Verfügung. Die Spektren von NGC 1846 wurden hingegen eigens zu diesem Zweck gewonnen und mussten daher erst reduziert werden, wofür das IRAF-Paket verwendet wurde. Nach der Datenreduktion wurde eine Reihe von synthetischen Spektren mit unterschiedlichen Fluorhäufigkeiten erstellt, basierend auf MARCS-Modellen und mit Hilfe des COMA-Codes. Durch Vergleich der beobachteten mit den synthetischen Spektren konnten schließlich die Fluorhäufigkeiten der Sterne bestimmt werden.

Die Objekte des Haufens NGC 1846 zeigen zwar großteils eine geringe Häufigkeit von [F/Fe] $\approx$ -0.77, einige erreichen jedoch auch deutlich höhere Werte von bis zu [F/Fe] = +0.23. Sterne mit höheren Fluorhäufigkeiten weisen in der Regel auch höhere C/O Verhältnisse auf, der 'third dredge-up' findet also zumindest in einigen dieser Sterne statt. Der Anstieg ist auch deutlich steiler als er von Standardmodellen vorhergesagt wird, also ist unser Verständnis der Prozesse, die in diesen Sternen ablaufen, noch nicht ausreichend.
Die Objekte des Haufens NGC 1978 zeigen eher homogene Fluorhäufigkeiten um [F/Fe] $\approx$ -0.27. Auch ihre C/O Verhältnisse sind sich recht ähnlich, was darauf hindeutet, dass

in den M-Sternen dieses Haufens der 'third dredge-up' nicht stattfindet. Natürlich ist aber die Verlässlichkeit dieser Aussage aufgrund der geringen Anzahl an Beobachtungen (5 Sterne) beschränkt.

Für die Messungen wurden drei verschiedene Fluorwasserstoff-Spektrallinien verwendet, R15 und R16 für die Objekte in NGC 1846 und R7 für die Objekte in NGC 1978. Während sowohl R15 und R16 gut messbar sind, wird R7 von einer starken CO-Linie überlagert, was die Messgenauigkeit einschränkt. Vergleicht man darüber hinaus die Messungen der NGC 1846 - Objekte mit älteren Messungen, bei welchen ebenfalls diese Linie verwendet wird, fällt ein Offset von ≈ 0.2 zwischen den beiden Messreihen auf. Die Messungen mit Hilfe von R7 ergeben deutlich höhere Werte, was bei zukünftigen Häufigkeitsmessungen mit dieser Linie in Betracht gezogen werden sollte.

Curriculum vitae

Andreas Hren

Personal data

Date, place of birth	08.12.1984, Klagenfurt
Nationality	Austrian
Adress	1040 Vienna
E-mail	andrej.hren@gmx.net

Education

03/2008–	University of Vienna, Master Studies, Astronomy
10/2004–01/2008	University of Vienna, Bachelor Studies, Astronomy
09/1995–06/2003	BG/BRG für Slowenen, Klagenfurt
09/1991–06/1995	Volksschule Sittersdorf

Professional Experience

2010–2011	University of Vienna, Tutor for 'Beobachtungorientiertes Praktikum'
2008–2009	University of Vienna, Tutor for 'Einführung in die Astronomie 2'

Research Interests

Stellar nucleosynthesis

Late stellar evolutionary stages

Chemical evolution of stars and stellar populations

Languages

Slovene & German (native), English